Design and Fabrication of Optical Fiber Sources in the Middle Infrared

Department of Electrical and Information Engineering
Electrical and Information Engineering
Ph.D. Program
SSD: ING-INF/02 – ELECTROMAGNETIC FIELDS

Final Dissertation

Design and Fabrication of Optical Fiber Sources in the Middle Infrared

---

by

Mario Christian FALCONI

Supervisor:

Prof. Francesco PRUDENZANO

Coordinator of Ph.D. Program:
Prof. Luigi Alfredo GRIECO

Course n°31, 01/11/2015–31/10/2018

Department of Electrical and Information Engineering
Electrical and Information Engineering
Ph.D. Program
SSD: ING-INF/02 – ELECTROMAGNETIC FIELDS

Final Dissertation

Design and Fabrication of Optical Fiber Sources in the Middle Infrared

---

by

Mario Christian FALCONI

Referees:

Prof. Trevor BENSON

Prof. Dominik DOROSZ

Supervisor:

Prof. Francesco PRUDENZANO

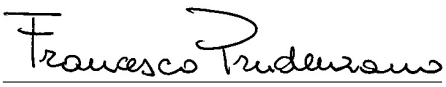

Coordinator of Ph.D. Program:
Prof. Luigi Alfredo GRIECO

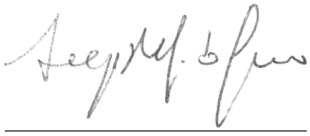

Course n°31, 01/11/2015–31/10/2018

To my parents

"If you want to find the secrets of the universe, think in terms of energy, frequency and vibration."

Nikola Tesla (1856-1943)

Contents

Abstract

In this thesis, the feasibility investigation of different fiber lasers for mid-IR applications is accurately performed via home-made computer codes. Different host glasses and pumping schemes are proposed. In particular, the thesis reports simulation results referring to: i) an optimized optical source exploiting a master oscillator power amplifier (MOPA) configuration, the MOPA pump and signal wavelengths being 1709 nm and 4384 nm, respectively [1]; ii) the design of an efficient pumping scheme for a Dy^{3+}:$Ga_5Ge_{20}Sb_{10}S_{65}$ fiber laser which provides an optical beam emission close to 4400 nm wavelength by employing two pump beams at 2850 nm and 4092 nm wavelengths [2]; iii) the employment of the particle swarm optimization (PSO) technique to maximize the optical gain of an in-band pumped fiber amplifier based on a dysprosium-doped ZBLAN glass; iv) the design of a continuous-wave (CW) fiber laser based on the same dysprosium-doped ZBLAN glass; v) a time-dependent numerical model of a dysprosium-doped ZBLAN glass fiber developed in order to design a pulsed laser emitting at about 3 µm wavelength, by employing the gain switching technique [3]. In all the cases, spectroscopic parameters measured on preliminary samples of chalcogenide and ZBLAN glasses are taken into account to fulfill realistic simulations.

Chalcogenide glasses are extremely promising for innovative applications at longer wavelengths, but further technological efforts in terms of glass purification, fiber drawing and doping with rare earths are required. On the other hand, ZBLAN glasses offer the possibility to develop novel lasers by employing available-on-the-market optical fibers. For this reason, an experimental activity in collaboration with the research group led by Prof. Gianluca Galzerano of the Department of Physics of Polytechnic

University of Milan has been started in order to realize the set-up of a CW dysprosium-doped ZBLAN fiber laser emitting at 3 µm.

Acknowledgement

I would like to express my deep gratitude to my research supervisor, Professor Francesco Prudenzano, for his patient guidance, enthusiastic encouragement and useful critiques of this doctoral research work. His willingness to give his time so generously has been very much appreciated.

I wish to thank my parents for their support and encouragement throughout my study.

I am particularly grateful for the assistance given by Chiara Capriulo for her valuable and constructive suggestions during the planning and development of this doctoral research work.

Finally, I wish to thank my friends Giuseppe Palma, Enza Portosi, Dario Laneve, William Scarcia, Giovanni Vitale, Flavia De Pace, Fabrizio Caramia, Francesco Chiarolli, Giovanni La Tanza, Angelo Pellegrino, Alessandro Giordano, Ivan Cardea and Elisa Nutini.

Introduction

In recent years, the availability of glasses with better optical properties in the middle infrared (mid-IR), compared to silica, has opened the way for novel types of optical sensors, lasers and amplifiers. In fact, a lot of rare earth energy transitions with emission wavelengths greater than 2.5 µm, which are quenched in silica, could be exploited more easily in low-phonon-energy glasses such as chalcogenide and fluoride glasses, some of which are transparent till 15–20 µm. The mid-IR wavelength range is important for several reasons. For example, many biological molecules and greenhouse gases (like carbon dioxide, methane and nitrous oxide) exhibit strong absorption peaks in this region of the electromagnetic spectrum. This is due to the existence of vibrational resonances of chemical bonds such as C-H stretching (terminal alkynes, a kind of hydrocarbons), N-H stretching (amines) and O-H stretching (alcohols, phenols). In addition, the earth atmosphere exhibits several transmission windows, e.g. the 3–4 µm, 4.3–5.0 µm, 8–10 µm and 10–14 µm wavelength ranges. Moreover, laser ablation surgery can greatly benefit from the strong water absorption of biological tissues at mid-IR wavelengths.

Mid-IR optical sources could be employed in optical sensing systems based on attenuation [4, 5] or fluorescence [6] measurements, whose feasibility has already been demonstrated in the visible spectral range, finding application in the fields of chemical and biological sensing, remote sensing and earth atmosphere monitoring. Another possible application could be in free space optical (FSO) communication, whose major characteristics are the wide bandwidth, license-free spectrum, high bit rate, low power and lightness [7,8]. FSO communication systems allow different optical links, e.g.

terrestrial ones within the Earth's atmosphere, indoor, inter-satellite space, ground-to-satellite/satellite-to-ground links [7–11]. In these systems, mid-IR optical amplifiers play an important role by allowing light signals of different wavelengths, beyond the third window, to be amplified simultaneously with the high efficiency typical of wavelength division multiplexing (WDM) techniques. They could be useful in the receivers, too. In this case, they could operate as appropriate preamplifiers before direct detection, thus enhancing the receiving station sensitivity.

Quantum cascade lasers (QCLs) are among the most popular devices with emission in the mid-IR wavelength range. Their main advantages are the wavelength tunability and the low cost. However, the beam quality achievable in fiber lasers cannot be reached by QCLs. Moreover, power scaling, narrow linewidth and short pulse generation are features which can be obtained more easily and more efficiently in fiber lasers. Therefore, this thesis has been devoted to the theoretical study, design and optimization of optical fiber sources, i.e. rare earth-doped lasers and amplifiers, emitting in the middle infrared. Both continuous-wave (CW) and pulsed regimes were considered.

Chapter 1 reports a brief overview of the optical materials employed in active mid-IR fiber devices.

Chapter 2 illustrates the theoretical models developed for the design and the optimization of rare earth-doped fiber lasers and amplifiers.

In chapter 3, the design of a master oscillator power amplifier (MOPA) configuration for a Dy^{3+}:$Ga_5Ge_{20}Sb_{10}S_{65}$ fiber laser is reported.

Chapter 4 reports an innovative pumping scheme, based on a double pump configuration, in order to further enhance the emission efficiency of the fiber laser shown in chapter 3.

In chapter 5, the particle swarm optimization technique is exploited to optimize the performance of a Dy^{3+}:ZBLAN fiber amplifier.

Chapter 6 reports the design of a continuous-wave fiber laser, based on the same ZBLAN glass, emitting at 3 µm.

Finally, in chapter 7 a finite-difference time-domain (FDTD) algorithm is imple-

mented to numerically investigate the feasibility of a gain-switched Dy^{3+}:ZBLAN fiber laser.

Chapter 1

Optical materials for mid-IR applications

1.1 Chalcogenide glasses

In recent years, chalcogenide glasses have been proposed as a potential host material for rare earths to realize fiber amplifiers and lasers [1, 2, 5, 12–16]. These glasses, composed of elements such as sulphur (S), selenium (Se) and tellurium (Te), are characterized by large absorption and emission cross sections for rare-earth ions, exhibiting high refractive indices. Other important characteristics of chalcogenide glasses are the absence of high-energy phonons in the vibrational spectrum and the low probability of multiphonon relaxation of rare-earth ions. These properties increase the efficiency of transitions between rare-earth energy levels compared to silica and fluoride glasses, and also improve other radiative transitions useful for exploiting amplification effects in the mid-infrared region (3–12 µm). Another important property of chalcogenide glasses, for the manufacture of compact and efficient devices, is the capability, for many glass compounds, to accommodate high dopant concentrations without ion clustering and concentration quenching effects [17, 18].

A classic method for the manufacture of microstructured optical fibers (MOF) is the stack-and-draw technique. However, this technique induces high optical losses

(several $\mathrm{dB\,m^{-1}}$) in chalcogenide glass MOFs due to the poor quality of the interfaces between capillaries. Recently, a casting method has been proposed for the manufacture of preforms made of chalcogenide glass [19]. Glass samples consisting of a compound of $As_{38}Se_{62}$ and $Ge_{10}As_{22}Se_{68}$ are manufactured and purified using the typical sealed silica tube method. To develop the fiber, a rather fluid liquid glass is moulded into a silica container with aligned silica capillaries. Once the liquid has filled the empty space, the silica container is tempered at room temperature. The operation is followed by the dissolution of the silica capillaries by treatment with hydrofluoric acid (HF). The mould is entirely made from a capillary wire in hexagonal silica guides. The silica guides are prepared by cutting a preform of microstructured silica. After the dissolution of the silica, the resulting microstructured chalcogenide glass preform is pulled into fibers in controlled helium atmosphere. Typical diameters of fibers made by this process range from 100 to 300 µm. During the process, the diameters of the holes are adjusted by applying an appropriate pressure to the holes in the preform. Fig. 1.1 reports some examples of optical fiber geometries which can be obtained by employing this technique.

In chapters 3 and 4, the $Ga_5Ge_{20}Sb_{10}S_{65}$ chalcogenide glass is employed to design a master oscillator power amplifier (MOPA) laser and an innovative pumping scheme for a photonic crystal fiber (PCF) laser, respectively.

1.2 Fluoride glasses

Fluoride glasses are a class of non-oxide optical glasses composed of fluorides of various metals. Of particular interest are the heavy metals fluoride glasses (HMFG), synthesized by Poulain and Lucas in 1975 at the University of Rennes in France. HMFGs exhibit a low optical attenuation, but are very brittle and not very resistant to moisture. They are used for the manufacture of optical fibers in the mid-infrared band thanks to the their low intrinsic losses with respect to silica fibers, which are transparent only at wavelengths below 2 µm. In fact, fluoride glasses are transparent

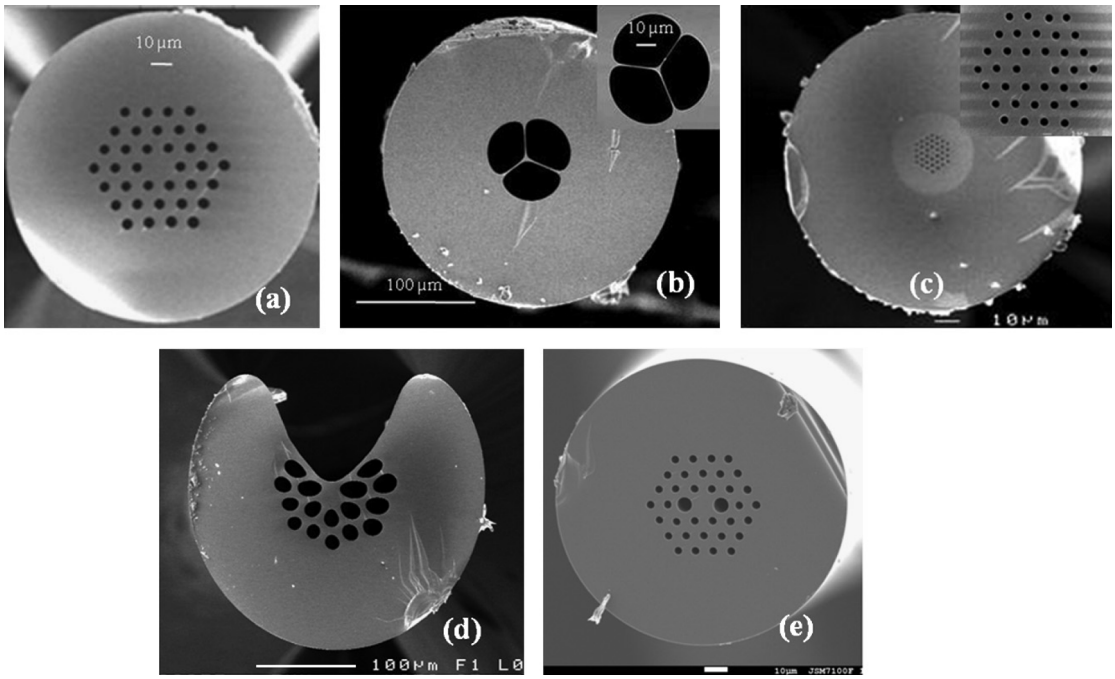

Figure 1.1: Examples of chalcogenide glass microstructured optical fibers: (a) three rings large core fiber, (b) small suspended core, (c) three rings small core fiber, (d) exposed core fiber and (e) highly birefringent fiber [20].

from the ultraviolet band to the mid-infrared band, without any absorption peak.

Many families of fluoride glasses have been studied, but only some of them have been found suitable for the manufacture of high-quality optical fibers. Zirconium fluoride glass, commonly known as ZBLAN (ZrF_4–BaF_2–LaF_3–AlF_3–NaF), was the first to be discovered and is also the most stable. Initially, fibers made from such glass were very brittle and expensive. Fortunately, much progress has been made over the last 15 years in improving the mechanical strength of these structures. Current fibers are very solid and flexible, with a mechanical strength ranging from 350 MPa to 700 MPa, depending on the geometry and parameters of the fiber [21].

The major disadvantage of ZBLAN glass is the difficult manufacturing process, mainly due to the formation of bubbles and irregularities at the core-cladding interface. The process takes place at 310 °C in a controlled atmosphere (in order to minimize contamination from oxygen and moisture impurities which would significantly weaken the fiber). Manufacturing is also complicated by the small difference (only 124 °C) between the glass transition temperature and the crystallization temperature. As a

result, ZBLAN fibers often contain undesired crystallites, which can be reduced by working the material under zero-gravity conditions [22]. If a glassy mixture solidifies too slowly, in fact, its atoms tend to crystallize in ordered structures. Earth gravity also has deleterious effects, stretching and mixing the fluid, and making it easier for the crystals to form. The solution could be to produce these glasses in space, in the absence of gravity.

The main strengths of this glass are: (i) low dispersion, (ii) low refractive index ($n = 1.48$ at the wavelength $\lambda = 2.88\,\mu\text{m}$), (iii) low and negative temperature coefficient of refractive index dn/dT, and (iv) high emission efficiency when doped with rare-earth ions. Moreover, unlike chalcogenide fibers, ZBLAN ones are available on the market and are widely used for many applications: spectroscopy, sensing, lasers and amplifiers [23–34].

In chapters 5, 6 and 7, the ZBLAN glass is employed to design a fiber amplifier, a continuous-wave fiber laser and a gain-switched fiber laser, respectively.

1.3 Optical amplification in rare earth-doped glasses

1.3.1 Light-matter interaction

The concept of optical amplification is based on the interaction between light and matter, i.e. between the dopant atoms inside the active medium and the photons of the light propagating through it. Each atom has a discrete set of energy levels, each with a well-defined energy value. Electrons can occupy only these states and can exchange energy with their surroundings only with transitions equal to the energy difference between two levels. Since the energy of a photon is given by $E = h\nu = \frac{hc_0}{\lambda}$, where $h = 6.626\,07 \times 10^{-34}\,\text{J}\,\text{s}^{-1}$ is Planck's constant, there is the possibility of energy exchange between atom and radiation only if the energy associated with the photons is greater than or equal to the energy difference between the energy levels considered. Otherwise, the system will be transparent to the incident electromagnetic radiation.

When the density of atoms is high, like in a material, the energy levels undergo strong transformations due to interatomic interactions and energy bands are generated. These bands are composed of many energy levels so close together that they are almost continuous. The energy transitions that occur in a medium, given the interaction with light radiation, are absorption, stimulated emission and spontaneous emission.

When a photon interacts with an atom, it can be absorbed causing an electron to transition from a lower energy level E_1 to a higher one E_2, if its frequency is equal to $\nu = \frac{E_2 - E_1}{h}$. If $\Phi = \frac{I}{h\nu}$ is the photon flux of the incident wave (number of incident photons per unit time per unit area), the absorption rate can be defined as follows:

$$W_{12} = \sigma_{12}(\nu)\Phi = \sigma_{12}(\nu)\frac{I}{h\nu} \tag{1.1}$$

where the coefficient σ_{12} is the absorption cross section for the $1 \rightarrow 2$ transition and has the dimension of a surface. In general, the cross section is a function of the frequency ν.

When an electron is in the excited state E_2 and the system is affected by a photon having energy equal to the difference between that level and an underlying one E_1, there is the stimulated emission of a further photon with energy $h\nu = E_2 - E_1$, accompanying the original photon and the transition of the electron to the lowest energy level.

The main characteristic of the stimulated emission is that the secondary photon has the same frequency and is in phase with the primary photon, producing a coherent emission.

In an analogous way to the case of absorption, the rate of stimulated emission can be defined as follows:

$$W_{21} = \sigma_{21}(\nu)\Phi = \sigma_{21}(\nu)\frac{I}{h\nu} \tag{1.2}$$

where the coefficient σ_{21} is the emission cross section for the $2 \rightarrow 1$ transition and has

the dimension of a surface.

When an electron is in the excited state E_2, in the absence of interactions with the surrounding environment, it remains in that state for a certain time which is defined as the average lifetime τ.

Excited electrons tend to return spontaneously to the lowest energy level through transitions that can be radiative, i.e. with the emission of a photon of energy $h\nu = E_2 - E_1$ equal to the energy difference between the levels, or non-radiative, in which there is no photon emission, but the emission of a phonon with dissipation of energy exchanged with the glass structure in the form of heat. The latter process is also called non-radiative decay. Photons are emitted in a stochastic manner and there are no phase relationships between the photons emitted by the group of de-exciting atoms. Therefore, spontaneous emission results in incoherent emission.

If N_2 is the number of excited atoms at level 2 per unit volume, the decay rate or decay probability is given by:

$$\frac{\mathrm{d}N_2(t)}{\mathrm{d}t} = -A_{21}N_2(t) \tag{1.3}$$

where the coefficient A_{21}, which has units s^{-1}, is called Einstein A coefficient for the $2 \rightarrow 1$ transition and indicates the probability of spontaneous emission per unit time of the single atom. The differential equation (1.3) is well-known in literature and its solution is:

$$N_2(t) = N_2(0)e^{-A_{21}t} = N_2(0)e^{-\frac{t}{\tau_{21}}} \tag{1.4}$$

where $\tau_{21} = \frac{1}{A_{21}}$ is the average lifetime of the spontaneous emission, i.e. the time interval after which the population of excited atoms at level 2 decreases by a factor of $\frac{1}{e} \approx 36.8\,\%$ with respect to the initial value.

1.3.2 Population inversion and optical pumping

Optical amplification within a glass medium doped with rare earths is based on the stimulated emission of photons by electrons, whose decay towards the underlying energy level is induced by the optical signal propagating through the structure.

The first problem to face is that, at room temperature, the fundamental level is much more populated than the excited level. Another problem is that the stimulated emission is in competition with the phenomena of spontaneous decay, radiative and non-radiative. These have the double negative effect of deteriorating the amplification by reducing the population of electrons at the higher level and, in the case of radiative decay, of superimposing noise on the signal of interest. To obtain stimulated emission, it is then necessary to make the population of the upper energy level greater than that of the lower level, i.e. population inversion must be achieved. The population inversion is obtained by sending a suitable optical signal, called pump signal, having a wavelength lower (or equivalently a higher frequency) than that of the signal to be amplified. This operation is called optical pumping.

The probability of a stimulated transition (absorption or emission) increases with the increase of the number of ions excitable from the ground state to the upper level by pumping. Thus, with the same pump power and transverse dimensions of the guiding structure, the amplification strength improves as the dopant concentration increases. However, there is a maximum limit to the dopant concentration in the glass matrix beyond which phenomena of interaction between the dopant ions become prevalent, causing a deterioration of the amplification capability.

1.3.3 Rare earth elements

Rare earths are divided into two groups of 14 elements each: lanthanides and actinides. Lanthanides range from cerium (atomic number $Z = 58$) to lutetium ($Z = 71$). Among the actinides, the best known are thorium (Th), uranium (U) and plutonium (Pu). Only lanthanides are important for optical amplification because they have sta-

ble isotopes. All rare-earth atoms have the same external electronic configuration as Xenon ([Xe] $6s^2$) and the number of electrons occupying the 4f internal orbitals determine their optical characteristics.

Rare-earth ionization usually results in a trivalent form (e.g. Dy^{3+}). Two 6s electrons and one 4f electron are removed, instead the 5s and 5p orbitals do not undergo alterations. The 4f electrons are therefore partially shielded from perturbations of external fields, so the wavelengths of emission and absorption depend less on variations in the external fields than other transition elements.

The main characteristics of rare earths for use in active optical devices are:

- fluorescence and absorption in small wavelength ranges;
- negligible dependence on the host glass material;
- low intensity of emission and absorption transitions;
- rather long average lifetimes of the metastable states (in the order of ms);
- high quantum efficiency (ratio between the radiative emission rate and the overall emission rate).

Moreover, a single active medium can be doped with more than one rare earth, allowing the exploitation of peculiar energy transfer phenomena between different rare earths [35–39]. Fig. 1.2 reports the list of rare earth elements along with their energy levels.

In this thesis, the optical transitions of dysprosium (Dy) rare-earth ions are extensively studied and exploited in order to design fiber lasers and amplifiers operating in the wavelength ranges around 3 µm ($^6H_{13/2} \rightarrow {}^6H_{15/2}$ transition) and 4.4 µm ($^6H_{11/2} \rightarrow {}^6H_{13/2}$ transition).

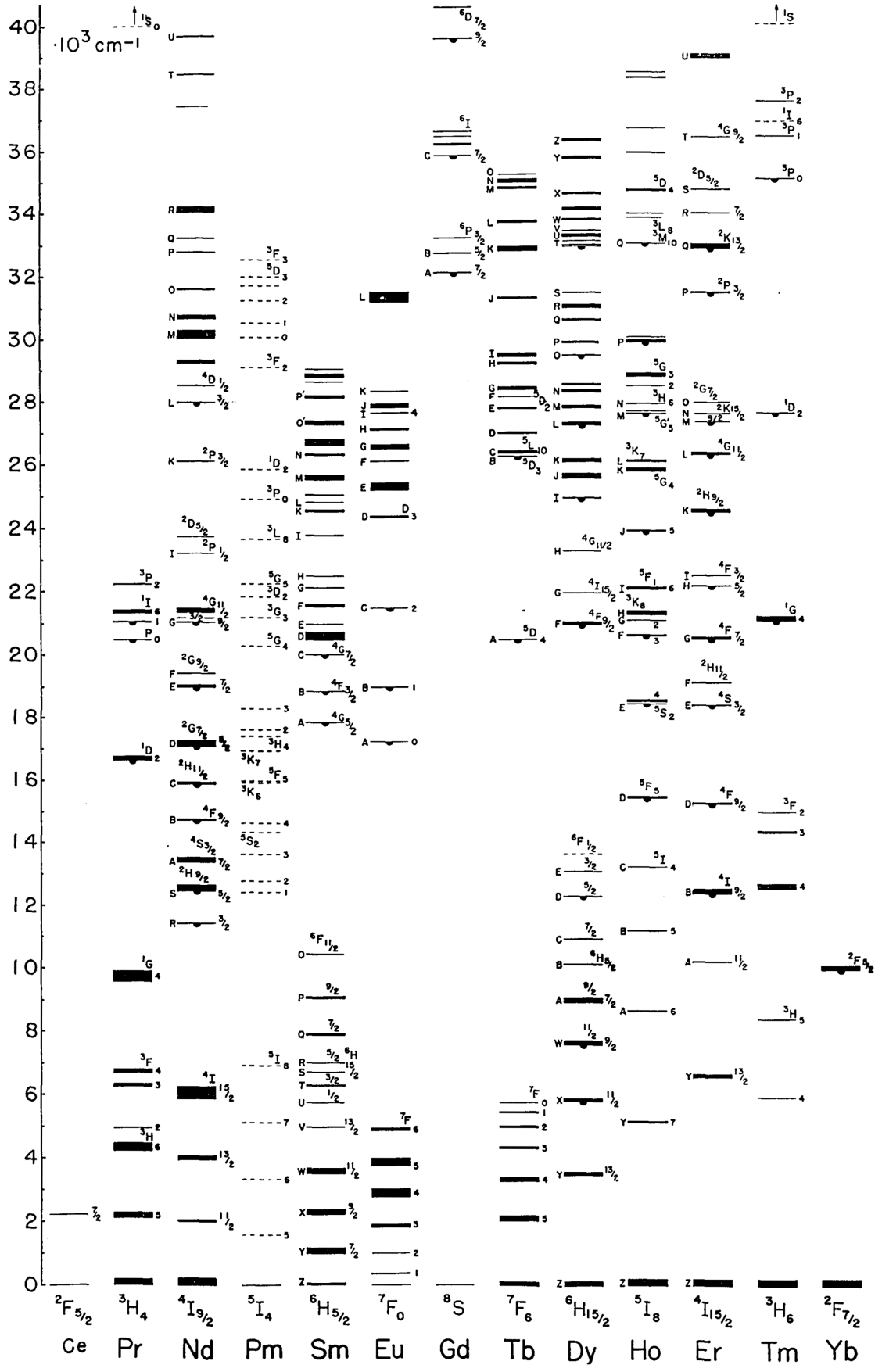

Figure 1.2: Rare earth elements and their energy levels [40].

Chapter 2

Theory

In this chapter, the various analytical models developed for the design and the optimization of rare earth-doped fiber lasers and amplifiers are presented. In particular, in the first section the devices based on the $Ga_5Ge_{20}Sb_{10}S_{65}$ chalcogenide glass are described, whereas in the second section those based on ZBLAN glass are considered. Finally, a brief description of the particle swarm optimization (PSO) algorithm is presented.

2.1 Analytical models for chalcogenide glass-based devices

2.1.1 Master oscillator power amplifier pumped at 1.7 µm

Laser Modeling

The interaction of dysprosium ions with the light is modeled as a three levels laser system, as illustrated in Fig. 2.1. All the relevant energy transitions are taken into account, i.e. those involved in absorption, stimulated and spontaneous emission phenomena. The amplified spontaneous emission (ASE) is neglected for laser operation since its contribution is low compared to the generated signal.

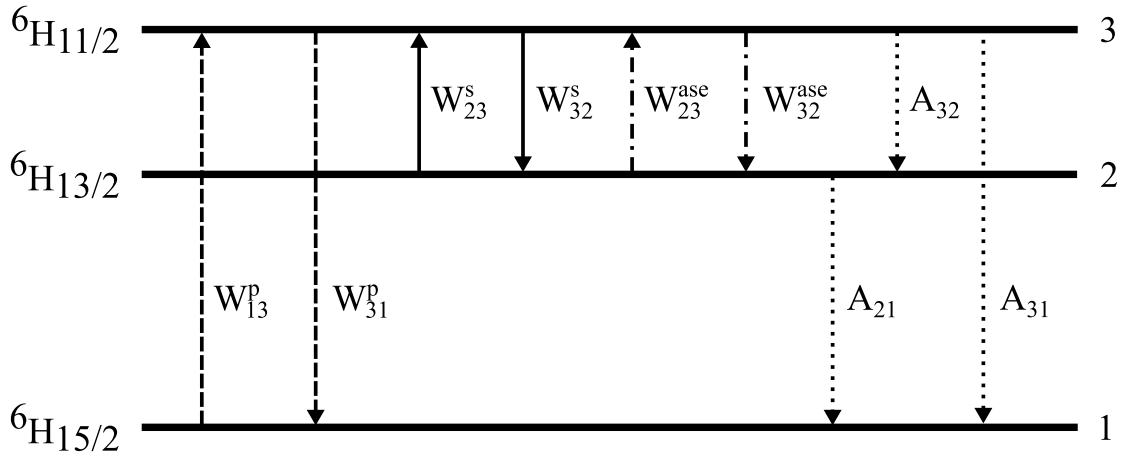

Figure 2.1: Energy levels and transitions for Dy^{3+}.

The laser steady-state rate equations (2.1) are:

$$\begin{bmatrix} C_{11} & C_{12} & C_{13} \\ C_{21} & C_{22} & C_{23} \\ C_{31} & C_{32} & C_{33} \end{bmatrix} \begin{bmatrix} N_1 \\ N_2 \\ N_3 \end{bmatrix} = \begin{bmatrix} 0 \\ 0 \\ N_{\mathrm{Dy}} \end{bmatrix} \tag{2.1}$$

where $C_{11} = W^{\mathrm{p}}_{13}$, $C_{12} = W^{\mathrm{s}}_{23}$, $C_{13} = -W^{\mathrm{p}}_{31} - W^{\mathrm{s}}_{32} - \frac{1}{\tau_3}$, $C_{21} = 0$, $C_{22} = -W^{\mathrm{s}}_{23} - \frac{1}{\tau_2}$, $C_{23} = W^{\mathrm{s}}_{32} + \frac{\beta_{32}}{\tau_3}$ and $C_{31} = C_{32} = C_{33} = 1$, $W_{ij} = \frac{\sigma_{ij}(\nu)}{h\nu} P(z)|E(x,y,\nu)|^2$ are the transition rates and σ_{ij} the cross sections pertaining to the $i \rightarrow j$ transition, h the Planck constant, ν the optical frequency, $P(z) = P^+(z) + P^-(z)$ the optical mode power (superscript + for the forward propagating beam and superscript - for the backward propagating beam), $|E(x,y,\nu)|^2$ the optical mode intensity normalized by putting its surface integral over the waveguide cross-section equal to the unit, τ_i the lifetimes and β_{ij} the branching ratios, $N_i(x,y,z)$ with $i = 1,2,3$ are the steady-state ion populations of the i-th Dy^{3+} energy level.

The laser power propagation equations (2.2) are:

$$\begin{cases} \dfrac{\mathrm{d}P_{\mathrm{p}}}{\mathrm{d}z} = g_{\mathrm{p}}(z)P_{\mathrm{p}}(z) - \alpha(\nu_{\mathrm{p}})P_{\mathrm{p}}(z) \\ \dfrac{\mathrm{d}P^+_{\mathrm{s}}}{\mathrm{d}z} = g_{\mathrm{s}}(z)P^+_{\mathrm{s}}(z) - \alpha(\nu_{\mathrm{s}})P^+_{\mathrm{s}}(z) \\ \dfrac{\mathrm{d}P^-_{\mathrm{s}}}{\mathrm{d}z} = -g_{\mathrm{s}}(z)P^-_{\mathrm{s}}(z) + \alpha(\nu_{\mathrm{s}})P^-_{\mathrm{s}}(z) \end{cases} \tag{2.2}$$

where $g_{\mathrm{p}}(z) = -\sigma_{13}(\nu_{\mathrm{p}})n_1(z,\nu_{\mathrm{p}}) + \sigma_{31}(\nu_{\mathrm{p}})n_3(z,\nu_{\mathrm{p}})$ and $g_{\mathrm{s}}(z) = -\sigma_{23}(\nu_{\mathrm{s}})n_2(z,\nu_{\mathrm{s}}) + \sigma_{32}(\nu_{\mathrm{s}})n_3(z,\nu_{\mathrm{s}})$.

$P_{\mathrm{p}}(z)$ and $P_{\mathrm{s}}^{\pm}(z)$ are the optical powers for pump and signal, respectively. The overlap integral between the normalized optical mode intensity and the population concentrations of the energy levels is given by the following equation:

$$n_i(z,\nu) = \int_{\Omega_{\mathrm{d}}} N_i(x,y,z)|E(x,y,\nu)|^2 \,\mathrm{d}x\mathrm{d}y \tag{2.3}$$

where Ω_{d} is the rare earth-doped region. It is apparent that in (2.3) the overlap integral depends on the optical mode intensity, which gives the frequency dependence of $n_i(z,\nu)$.

Equations (2.1) and (2.2) are integrated with the boundary conditions imposed by the laser mirrors:

$$\begin{cases} P_{\mathrm{s}}^{-}(L_1) = R_2 P_{\mathrm{s}}^{+}(L_1) \\ P_{\mathrm{s}}^{+}(0) = R_1 P_{\mathrm{s}}^{-}(0) \end{cases} \tag{2.4}$$

where L_1 is the laser cavity length.

Amplifier Modeling

The model for the Dy^{3+}-doped fiber amplifier is very similar to that of the laser. In this case, ASE is taken into account in the amplifier model to include the related noise in the signal band. The ASE wavelength range spans from $\lambda = 4200\,\mathrm{nm}$ to $\lambda = 4600\,\mathrm{nm}$, its is sampled with $\Delta\lambda = 0.6\,\mathrm{nm}$ period.

The amplifier steady-state rate equations (2.5) are:

$$\begin{bmatrix} C_{11} & C_{12} + W_{23}^{\mathrm{ase}} & C_{13} - W_{32}^{\mathrm{ase}} \\ C_{21} & C_{22} - W_{23}^{\mathrm{ase}} & C_{23} + W_{32}^{\mathrm{ase}} \\ C_{31} & C_{32} & C_{33} \end{bmatrix} \begin{bmatrix} N_1 \\ N_2 \\ N_3 \end{bmatrix} = \begin{bmatrix} 0 \\ 0 \\ N_{\mathrm{Dy}} \end{bmatrix} \tag{2.5}$$

The transition rates for ASE noise are given by the expression $W_{ij}^{\mathrm{ase}} = \int_0^{+\infty} \frac{\sigma_{ij}(\nu)}{h\nu}$

$S_{\mathrm{ase}}(z,\nu)|E(x,y,\nu)|^2\,\mathrm{d}\nu$. $S_{\mathrm{ase}}(z,\nu)$ is the sum of the forward $S^{+}_{\mathrm{ase}}(z,\nu)$ and backward $S^{-}_{\mathrm{ase}}(z,\nu)$ power spectral densities. The other parameters are the same ones defined previously.

The amplifier power propagation equations (2.6) are:

$$\begin{cases} \dfrac{\mathrm{d}P_{\mathrm{p}}}{\mathrm{d}z} = g_{\mathrm{p}}(z)P_{\mathrm{p}}(z) - \alpha(\nu_{\mathrm{p}})P_{\mathrm{p}}(z) \\ \dfrac{\mathrm{d}P_{\mathrm{s}}}{\mathrm{d}z} = g_{\mathrm{s}}(z)P_{\mathrm{s}}(z) - \alpha(\nu_{\mathrm{s}})P_{\mathrm{s}}(z) \\ \dfrac{\mathrm{d}S^{+}_{\mathrm{ase}}}{\mathrm{d}z} = [g_{\mathrm{ase}}(z,\nu) - \alpha(\nu)]S^{+}_{\mathrm{ase}}(z,\nu) + a_{\mathrm{sp}}(z,\nu) \\ \dfrac{\mathrm{d}S^{-}_{\mathrm{ase}}}{\mathrm{d}z} = -[g_{\mathrm{ase}}(z,\nu) - \alpha(\nu)]S^{-}_{\mathrm{ase}}(z,\nu) - a_{\mathrm{sp}}(z,\nu) \end{cases} \tag{2.6}$$

where $g_{\mathrm{ase}}(z,\nu) = -\sigma_{23}(\nu)n_2(z,\nu) + \sigma_{32}(\nu)n_3(z,\nu)$ and $a_{\mathrm{sp}}(z,\nu) = 2h\nu\sigma_{32}(\nu)n_3(z,\nu)$. The functions $g_{\mathrm{p}}(z)$ and $g_{\mathrm{s}}(z)$ are defined previously.

The optical gain of the amplifier is defined as follows:

$$G = \frac{P_{\mathrm{s}}(L_1 + L_2)}{P_{\mathrm{s}}(L_1)} = \frac{P_{\mathrm{s}}(L)}{P_{\mathrm{s}}(L_1)} \tag{2.7}$$

where L_2 is the length of the fiber amplifier and $L = L_1 + L_2$.

The noise factor is:

$$F = \frac{1}{G}\left(1 + \frac{S^{+}_{\mathrm{ase}}(L,\nu_{\mathrm{s}})}{h\nu_{\mathrm{s}}}\right) \tag{2.8}$$

while the noise figure is given by

$$NF = 10\log_{10}(F) \tag{2.9}$$

The total efficiency η of the MOPA is defined as the ratio of the amplifier output signal power to the laser input pump power:

$$\eta = \frac{P_{\mathrm{s}}(L_1 + L_2)}{P_{\mathrm{p}}(0)} = \frac{P_{\mathrm{s}}(L)}{P_{\mathrm{p}}(0)}\,. \tag{2.10}$$

The previous expression can be rewritten in terms of the amplifier optical gain G and the laser efficiency η_{laser}:

$$\eta = \frac{P_{\text{s}}(L)}{P_{\text{s}}(L_1)} \frac{P_{\text{s}}(L_1)}{P_{\text{p}}(0)} = G\eta_{\text{laser}} \tag{2.11}$$

2.1.2 Double pumping at 2.85 µm and 4.1 µm

The rare earth-light interaction is modeled as a three level laser system (see Fig. 2.1). The model includes the pump absorption and stimulated emission close to the pump wavelengths $\lambda_{\text{p1}} = 2850\,\text{nm}$ (pump #1) and $\lambda_{\text{p2}} = 4092\,\text{nm}$ (pump #2), and the signal absorption and stimulated emission to the wavelength $\lambda_{\text{s}} = 4384\,\text{nm}$.

The rate equations (2.12) are:

$$\begin{bmatrix} C_{11} & C_{12} & C_{13} \\ C_{21} & C_{22} & C_{23} \\ C_{31} & C_{32} & C_{33} \end{bmatrix} \begin{bmatrix} N_1 \\ N_2 \\ N_3 \end{bmatrix} = \begin{bmatrix} 0 \\ 0 \\ N_{\text{Dy}} \end{bmatrix} \tag{2.12}$$

where $C_{11} = 0$, $C_{12} = W_{23}^{\text{p}} + W_{23}^{\text{s}}$, $C_{13} = -W_{32}^{\text{p}} - W_{32}^{\text{s}} - \frac{1}{\tau_3}$, $C_{21} = -W_{12}^{\text{p}}$, $C_{22} = W_{21}^{\text{p}} + \frac{1}{\tau_2}$, $C_{23} = \frac{\beta_{31}}{\tau_3}$ and $C_{31} = C_{32} = C_{33} = 1$, $N_i(x, y, z)$ with $i = 1, 2, 3$ are the steady-state ion populations of the Dy^{3+} energy levels, $W_{ij} = \frac{\sigma_{ij}(\nu)}{h\nu} P(z)|E(x, y, \nu)|^2$ the transition rates, σ_{ij} the cross section pertaining the $i \rightarrow j$ transition, h the Planck constant, ν the optical frequency, $P(z)$ the optical mode power, $E(x, y, \nu)$ the normalized optical mode intensity, τ_i the lifetimes and β_{ij} the branching ratios.

The power propagation equations (2.13) are:

$$\begin{cases} \dfrac{\mathrm{d}P_{\text{p1}}}{\mathrm{d}z} = g_{\text{p1}}(z)P_{\text{p1}}(z) - \alpha(\nu_{\text{p1}})P_{\text{p1}}(z) \\ \dfrac{\mathrm{d}P_{\text{p2}}}{\mathrm{d}z} = g_{\text{p2}}(z)P_{\text{p2}}(z) - \alpha(\nu_{\text{p2}})P_{\text{p2}}(z) \\ \dfrac{\mathrm{d}P_{\text{s}}^{+}}{\mathrm{d}z} = g_{\text{s}}(z)P_{\text{s}}^{+}(z) - \alpha(\nu_{\text{s}})P_{\text{s}}^{+}(z) \\ \dfrac{\mathrm{d}P_{\text{s}}^{-}}{\mathrm{d}z} = -g_{\text{s}}(z)P_{\text{s}}^{-}(z) + \alpha(\nu_{\text{s}})P_{\text{s}}^{-}(z) \end{cases} \tag{2.13}$$

where $g_{\text{p1}}(z) = -\sigma_{12}(\nu_{\text{p1}})n_1(z, \nu_{\text{p1}}) + \sigma_{21}(\nu_{\text{p1}})n_2(z, \nu_{\text{p1}})$, $g_{\text{p2}}(z) = -\sigma_{23}(\nu_{\text{p2}})n_2(z, \nu_{\text{p2}}) +$

$\sigma_{32}(\nu_{\mathrm{p2}})n_3(z,\nu_{\mathrm{p2}})$ and $g_{\mathrm{s}}(z) = -\sigma_{23}(\nu_{\mathrm{s}})n_2(z,\nu_{\mathrm{s}}) + \sigma_{32}(\nu_{\mathrm{s}})n_3(z,\nu_{\mathrm{s}})$.

$P_{\mathrm{p1}}(z)$, $P_{\mathrm{p2}}(z)$, $P_{\mathrm{s}}^{\pm}(z)$ are the optical powers for pump #1, pump #2 and signal, respectively. Positive sign is associated with forward direction, negative one with backward direction. The overlap integral between the normalized optical mode intensity and the population concentrations of the energy levels is given by the following equation:

$$n_i(z,\nu) = \int_{\Omega_{\mathrm{d}}} N_i(x,y,z)|E(x,y,\nu)|^2 \,\mathrm{d}x\mathrm{d}y \tag{2.14}$$

where Ω_{d} is the rare earth-doped region.

Equations (2.12) and (2.13) are integrated with the boundary conditions imposed by the laser mirrors:

$$\begin{cases} P_{\mathrm{s}}^{-}(L) = R_2 P_{\mathrm{s}}^{+}(L) \\ P_{\mathrm{s}}^{+}(0) = R_1 P_{\mathrm{s}}^{-}(0) \end{cases} \tag{2.15}$$

2.2 Analytical models for ZBLAN glass-based devices

2.2.1 Amplifier for 3 µm optical signals

The interaction of dysprosium ions with light, for the case of in-band pumping at 2.6–2.8 µm, can be modeled by employing a two energy levels system, as shown in Fig. 2.2. The $^6\mathrm{H}_{15/2}$ and $^6\mathrm{H}_{13/2}$ energy levels are the ground state and the excited state, respectively. All the most common rare earth-light interactions, i.e. absorption, stimulated emission, radiative and nonradiative decays, are taken into account and also the amplified spontaneous emission (ASE) noise contribution is considered. The

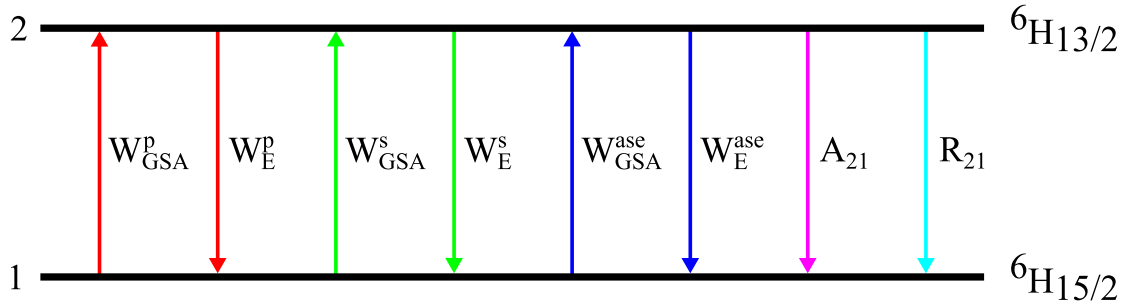

Figure 2.2: Diagram of energy levels and transitions for Dy^{3+} ions in ZBLAN glass.

level populations $N_1(x, y, z, t)$ and $N_2(x, y, z, t)$ obey the following equation system:

$$\begin{cases} \dfrac{\partial N_2}{\partial t} = (W^{\mathrm{p}}_{\mathrm{GSA}} + W^{\mathrm{s}}_{\mathrm{GSA}} + W^{\mathrm{ase}}_{\mathrm{GSA}})N_1 - (W^{\mathrm{p}}_{\mathrm{E}} + W^{\mathrm{s}}_{\mathrm{E}} + W^{\mathrm{ase}}_{\mathrm{E}} + A_{21} + R_{21})N_2 \\ \dfrac{\partial N_1}{\partial t} = -(W^{\mathrm{p}}_{\mathrm{GSA}} + W^{\mathrm{s}}_{\mathrm{GSA}} + W^{\mathrm{ase}}_{\mathrm{GSA}})N_1 + (W^{\mathrm{p}}_{\mathrm{E}} + W^{\mathrm{s}}_{\mathrm{E}} + W^{\mathrm{ase}}_{\mathrm{E}} + A_{21} + R_{21})N_2 \end{cases} \tag{2.16}$$

where $A_{21} = \frac{1}{\tau_2}$ and $R_{21} = \frac{1}{T_2}$ are the radiative and nonradiative decay rates for the $^6H_{13/2} \rightarrow {}^6H_{15/2}$ transition, respectively. The pump, signal and ASE noise transition rates are given by:

$$\begin{aligned} W^{\mathrm{p}}_{\mathrm{GSA}}(x, y, z) &= \frac{\sigma_{12}(\nu_{\mathrm{p}})}{h\nu_{\mathrm{p}}} P_{\mathrm{p}}(z) i_{\mathrm{p}}(x, y) \\ W^{\mathrm{p}}_{\mathrm{E}}(x, y, z) &= \frac{\sigma_{21}(\nu_{\mathrm{p}})}{h\nu_{\mathrm{p}}} P_{\mathrm{p}}(z) i_{\mathrm{p}}(x, y) \\ W^{\mathrm{s}}_{\mathrm{GSA}}(x, y, z) &= \frac{\sigma_{12}(\nu_{\mathrm{s}})}{h\nu_{\mathrm{s}}} P_{\mathrm{s}}(z) i_{\mathrm{s}}(x, y) \\ W^{\mathrm{s}}_{\mathrm{E}}(x, y, z) &= \frac{\sigma_{21}(\nu_{\mathrm{s}})}{h\nu_{\mathrm{s}}} P_{\mathrm{s}}(z) i_{\mathrm{s}}(x, y) \\ W^{\mathrm{ase}}_{\mathrm{GSA}}(x, y, z) &= \int_0^{+\infty} \frac{\sigma_{12}(\nu)}{h\nu} S_{\mathrm{ase}}(z, \nu) i_{\mathrm{s}}(x, y)\, \mathrm{d}\nu \\ W^{\mathrm{ase}}_{\mathrm{E}}(x, y, z) &= \int_0^{+\infty} \frac{\sigma_{21}(\nu)}{h\nu} S_{\mathrm{ase}}(z, \nu) i_{\mathrm{s}}(x, y)\, \mathrm{d}\nu \end{aligned}$$

where h is the Planck constant, ν_{p} and ν_{s} are the pump and signal frequencies, respectively, $\sigma_{12}(\nu)$ and $\sigma_{21}(\nu)$ are the absorption and emission cross sections, respectively. P_{p} and P_{s} represent the (forward) pump and signal powers, whereas $S_{\mathrm{ase}} = S^+_{\mathrm{ase}} + S^-_{\mathrm{ase}}$ is the total ASE power spectral density, i.e. the sum of forward and backward ASE noise. Finally, i_{p} and i_{s} are the normalized transverse intensity profiles for the pump and signal optical beams, respectively. Since the sum of level populations must be

equal to the total dopant concentration N_{Dy}, the system of equations (2.16) can be simplified by discarding one equation. Moreover, in continuous-wave operation, the time derivatives vanish. Therefore, the following system of linear algebraic equations is obtained:

$$\begin{cases} (W_{\mathrm{GSA}}^{\mathrm{p}} + W_{\mathrm{GSA}}^{\mathrm{s}} + W_{\mathrm{GSA}}^{\mathrm{ase}})N_1 - (W_{\mathrm{E}}^{\mathrm{p}} + W_{\mathrm{E}}^{\mathrm{s}} + W_{\mathrm{E}}^{\mathrm{ase}} + A_{21} + R_{21})N_2 = 0 \\ N_1 + N_2 = N_{\mathrm{Dy}}(x, y) \end{cases}$$

whose solution is:

$$\begin{cases} N_2(x, y, z) = \dfrac{W_{\mathrm{GSA}}^{\mathrm{p}} + W_{\mathrm{GSA}}^{\mathrm{s}} + W_{\mathrm{GSA}}^{\mathrm{ase}}}{W_{\mathrm{GSA}}^{\mathrm{p}} + W_{\mathrm{GSA}}^{\mathrm{s}} + W_{\mathrm{GSA}}^{\mathrm{ase}} + W_{\mathrm{E}}^{\mathrm{p}} + W_{\mathrm{E}}^{\mathrm{s}} + W_{\mathrm{E}}^{\mathrm{ase}} + A_{21} + R_{21}} N_{\mathrm{Dy}}(x, y) \\ N_1(x, y, z) = \dfrac{W_{\mathrm{E}}^{\mathrm{p}} + W_{\mathrm{E}}^{\mathrm{s}} + W_{\mathrm{E}}^{\mathrm{ase}} + A_{21} + R_{21}}{W_{\mathrm{GSA}}^{\mathrm{p}} + W_{\mathrm{GSA}}^{\mathrm{s}} + W_{\mathrm{GSA}}^{\mathrm{ase}} + W_{\mathrm{E}}^{\mathrm{p}} + W_{\mathrm{E}}^{\mathrm{s}} + W_{\mathrm{E}}^{\mathrm{ase}} + A_{21} + R_{21}} N_{\mathrm{Dy}}(x, y) \end{cases}$$

The evolution of the pump, signal and ASE noise powers along the fiber is governed by the following nonlinear ordinary differential equations (ODEs):

$$\begin{cases} \dfrac{\mathrm{d}P_{\mathrm{p}}}{\mathrm{d}z} = [-\sigma_{12}(\nu_{\mathrm{p}})n_{1\mathrm{p}}(z) + \sigma_{21}(\nu_{\mathrm{p}})n_{2\mathrm{p}}(z) - \alpha(\nu_{\mathrm{p}})]P_{\mathrm{p}} \\ \dfrac{\mathrm{d}P_{\mathrm{s}}}{\mathrm{d}z} = [-\sigma_{12}(\nu_{\mathrm{s}})n_{1\mathrm{s}}(z) + \sigma_{21}(\nu_{\mathrm{s}})n_{2\mathrm{s}}(z) - \alpha(\nu_{\mathrm{s}})]P_{\mathrm{s}} \\ \dfrac{\mathrm{d}S_{\mathrm{ase}}^{+}}{\mathrm{d}z} = [-\sigma_{12}(\nu)n_{1\mathrm{s}}(z) + \sigma_{21}(\nu)n_{2\mathrm{s}}(z) - \alpha(\nu)]S_{\mathrm{ase}}^{+} + 2h\nu\sigma_{21}(\nu)n_{2\mathrm{s}}(z) \\ \dfrac{\mathrm{d}S_{\mathrm{ase}}^{-}}{\mathrm{d}z} = [\sigma_{12}(\nu)n_{1\mathrm{s}}(z) - \sigma_{21}(\nu)n_{2\mathrm{s}}(z) + \alpha(\nu)]S_{\mathrm{ase}}^{-} - 2h\nu\sigma_{21}(\nu)n_{2\mathrm{s}}(z) \end{cases} \tag{2.17}$$

where $\alpha(\nu)$ is the optical loss of the glass. The overlap integrals between the ion populations and the optical modes of both pump and signal can be calculated by means of the following integrals over the rare earth-doped region Ω_{d}:

$$\begin{aligned} n_{1\mathrm{p}}(z) &= \iint_{\Omega_{\mathrm{d}}} N_1(x, y, z) i_{\mathrm{p}}(x, y)\, \mathrm{d}A \\ n_{2\mathrm{p}}(z) &= \iint_{\Omega_{\mathrm{d}}} N_2(x, y, z) i_{\mathrm{p}}(x, y)\, \mathrm{d}A \\ n_{1\mathrm{s}}(z) &= \iint_{\Omega_{\mathrm{d}}} N_1(x, y, z) i_{\mathrm{s}}(x, y)\, \mathrm{d}A \\ n_{2\mathrm{s}}(z) &= \iint_{\Omega_{\mathrm{d}}} N_2(x, y, z) i_{\mathrm{s}}(x, y)\, \mathrm{d}A \end{aligned}$$

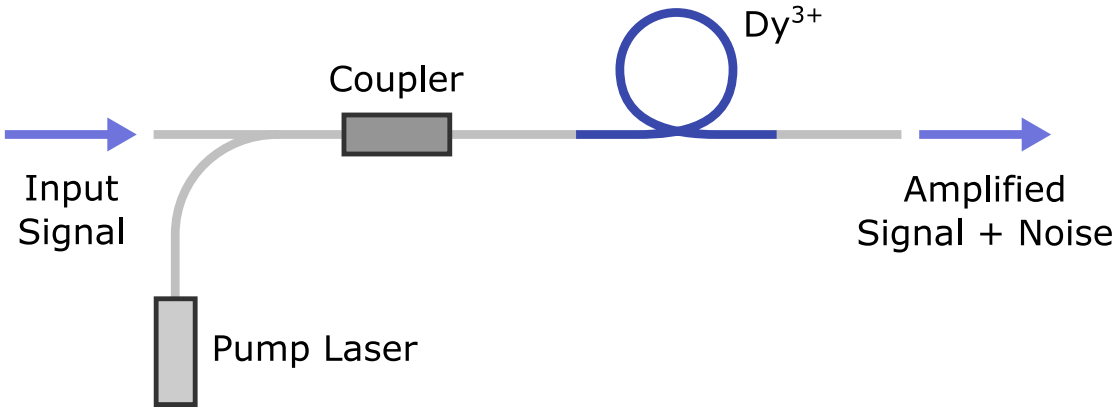

Figure 2.3: Schematic of the amplifier.

In order to solve the ODEs (2.17), suitable boundary conditions must be imposed (see Fig. 2.3):

$$P_{\mathrm{p}}(0) = P_{\mathrm{p0}}$$

$$P_{\mathrm{s}}(0) = P_{\mathrm{s0}}$$

$$S^{+}_{\mathrm{ase}}(0,\nu) = 0$$

$$S^{-}_{\mathrm{ase}}(L,\nu) = 0$$

The optical gain G and the noise figure NF of the fiber amplifier can be calculated as follows:

$$G = \frac{P_{\mathrm{s}}(L)}{P_{\mathrm{s}}(0)} = \frac{P_{\mathrm{s}}(L)}{P_{\mathrm{s0}}}$$

$$NF = 10\log_{10}\left[\frac{1}{G}\left(1 + \frac{S^{+}_{\mathrm{ase}}(L,\nu_{\mathrm{s}})}{h\nu_{\mathrm{s}}}\right)\right]$$

2.2.2 Continuous-wave laser emitting at 3 µm

In the case of in-band pumping, the Dy^{3+} active ions can be modeled as a two levels laser system (see Fig. 2.2). The electronic transitions involved are the following: i) pump absorption and stimulated emission, ii) signal absorption and stimulated emission, iii) radiative decay and multiphonon relaxation from the upper laser level $^{6}H_{13/2}$. Amplified spontaneous emission (ASE) is neglected.

The rate equations in steady-state form can be written as:

$$\begin{cases} (W^{\mathrm{p}}_{\mathrm{GSA}} + W^{\mathrm{s}}_{\mathrm{GSA}})N_1(x,y,z) = (W^{\mathrm{p}}_{\mathrm{E}} + W^{\mathrm{s}}_{\mathrm{E}} + A_{21} + R_{21})N_2(x,y,z) \\ N_1(x,y,z) + N_2(x,y,z) = N_{\mathrm{Dy}}(x,y) \end{cases} \tag{2.18}$$

where N_1 and N_2 are the ion populations, N_{Dy} is the dysprosium concentration, $A_{21} = \frac{1}{\tau_2}$ is the radiative decay rate with $\tau_2 = 13.7\,\mathrm{ms}$, $R_{21} = 1539\,\mathrm{s}^{-1}$ is the multiphonon relaxation rate. The transition rates can be computed as follows:

$$\begin{aligned} W^{\mathrm{p}}_{\mathrm{GSA}}(x,y,z) &= \frac{\sigma_{12}(\nu_{\mathrm{p}})P_{\mathrm{p}}(z)|E(x,y,\nu_{\mathrm{p}})|^2}{h\nu_{\mathrm{p}}} \\ W^{\mathrm{p}}_{\mathrm{E}}(x,y,z) &= \frac{\sigma_{21}(\nu_{\mathrm{p}})P_{\mathrm{p}}(z)|E(x,y,\nu_{\mathrm{p}})|^2}{h\nu_{\mathrm{p}}} \\ W^{\mathrm{s}}_{\mathrm{GSA}}(x,y,z) &= \frac{\sigma_{12}(\nu_{\mathrm{s}})P_{\mathrm{s}}(z)|E(x,y,\nu_{\mathrm{s}})|^2}{h\nu_{\mathrm{s}}} \\ W^{\mathrm{s}}_{\mathrm{E}}(x,y,z) &= \frac{\sigma_{21}(\nu_{\mathrm{s}})P_{\mathrm{s}}(z)|E(x,y,\nu_{\mathrm{s}})|^2}{h\nu_{\mathrm{s}}} \end{aligned}$$

where σ_{ij} is the cross section for the $i \to j$ electronic transition, h is the Planck constant, $\nu_{\mathrm{p/s}}$ is the pump/signal frequency, $P_{\mathrm{p}}(z)$ is the pump power, $P_{\mathrm{s}}(z) = P^{+}_{\mathrm{s}}(z) + P^{-}_{\mathrm{s}}(z)$ is the sum of forward (plus sign) and backward (minus sign) signal powers and $E(x,y,\nu_{\mathrm{p/s}})$ is the transverse profile of the normalized electric field at frequency $\nu_{\mathrm{p/s}}$.

The solution of the rate equations (2.18) is straightforward:

$$\begin{cases} N_2(x,y,z) = \dfrac{W^{\mathrm{p}}_{\mathrm{GSA}} + W^{\mathrm{s}}_{\mathrm{GSA}}}{W^{\mathrm{p}}_{\mathrm{GSA}} + W^{\mathrm{s}}_{\mathrm{GSA}} + W^{\mathrm{p}}_{\mathrm{E}} + W^{\mathrm{s}}_{\mathrm{E}} + A_{21} + R_{21}} N_{\mathrm{Dy}}(x,y) \\ N_1(x,y,z) = \dfrac{W^{\mathrm{p}}_{\mathrm{E}} + W^{\mathrm{s}}_{\mathrm{E}} + A_{21} + R_{21}}{W^{\mathrm{p}}_{\mathrm{GSA}} + W^{\mathrm{s}}_{\mathrm{GSA}} + W^{\mathrm{p}}_{\mathrm{E}} + W^{\mathrm{s}}_{\mathrm{E}} + A_{21} + R_{21}} N_{\mathrm{Dy}}(x,y) \end{cases}$$

In order to compute the evolution of the pump and signal beams along the fiber, the following power propagation equations must be solved:

$$\begin{cases} \dfrac{\mathrm{d}P_{\mathrm{p}}}{\mathrm{d}z} = g_{\mathrm{p}}(z)P_{\mathrm{p}}(z) - \alpha(\nu_{\mathrm{p}})P_{\mathrm{p}}(z) \\ \dfrac{\mathrm{d}P^{+}_{\mathrm{s}}}{\mathrm{d}z} = g_{\mathrm{s}}(z)P^{+}_{\mathrm{s}}(z) - \alpha(\nu_{\mathrm{s}})P^{+}_{\mathrm{s}}(z) \\ \dfrac{\mathrm{d}P^{-}_{\mathrm{s}}}{\mathrm{d}z} = -g_{\mathrm{s}}(z)P^{-}_{\mathrm{s}}(z) + \alpha(\nu_{\mathrm{s}})P^{-}_{\mathrm{s}}(z) \end{cases} \tag{2.19}$$

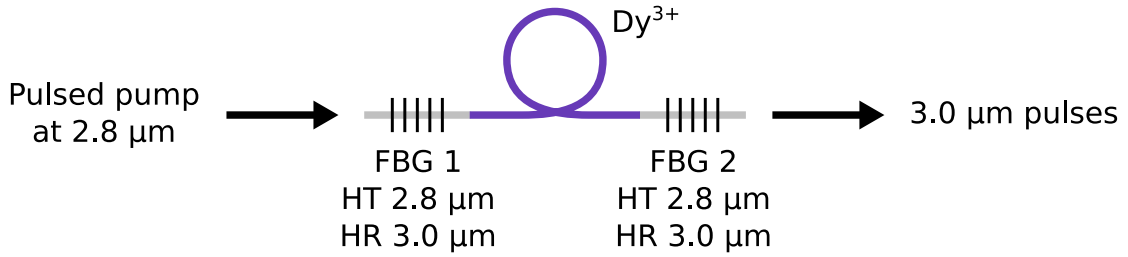

Figure 2.4: Schematic of the device.

where $g_{\mathrm{p}}(z) = -\sigma_{12}(\nu_{\mathrm{p}})n_1(z,\nu_{\mathrm{p}}) + \sigma_{21}(\nu_{\mathrm{p}})n_2(z,\nu_{\mathrm{p}})$ and $g_{\mathrm{s}}(z) = -\sigma_{12}(\nu_{\mathrm{s}})n_1(z,\nu_{\mathrm{s}}) + \sigma_{21}(\nu_{\mathrm{s}})n_2(z,\nu_{\mathrm{s}})$ are the gain coefficients for the pump and signal beams respectively, and $\alpha(\nu)$ denotes the fiber attenuation coefficient at frequency ν. The overlap integrals $n_i(z,\nu)$ over the doped region Ω_{d} can be computed as follows:

$$n_i(z,\nu) = \iint_{\Omega_{\mathrm{d}}} N_i(x,y,z)|E(x,y,\nu)|^2 \,\mathrm{d}x\mathrm{d}y$$

Finally, in order to solve the differential equation system (2.19), the following boundary conditions imposed by the cavity mirrors must be satisfied:

$$P_{\mathrm{s}}^{-}(L) = R_2 P_{\mathrm{s}}^{+}(L)$$
$$P_{\mathrm{s}}^{+}(0) = R_1 P_{\mathrm{s}}^{-}(0)$$

where L is the fiber length, while R_1 and R_2 are the reflectivities of the input and output mirrors at the signal frequency ν_{s}, respectively.

2.2.3 Gain-switched fiber laser

Theoretical model

In the proposed model, the rate equations coupled with the time-varying power propagation equations for the pump and signal beams are solved by including the time derivatives. Group velocity for all propagating waves is taken into account [41–43]. The optical behavior of dysprosium ions, for in-band pumping at $\lambda_{\mathrm{p}} = 2.8\,\mu\mathrm{m}$ wavelength, can be suitably modeled by employing a two levels laser system, as shown

in Fig. 2.2. The $^6H_{15/2}$ and $^6H_{13/2}$ energy levels are the fundamental state and the excited state, respectively. By taking into account the typical light-rare earth interactions, i.e. absorption, stimulated emission, radiative and nonradiative decays, the following equation system for the level populations $N_1(x, y, z, t)$ and $N_2(x, y, z, t)$ can be written:

$$\begin{cases} \dfrac{\partial N_2}{\partial t} = W_{\mathrm{GSA}} N_1 - (W_{\mathrm{E}} + A_{21} + R_{21}) N_2 \\ \dfrac{\partial N_1}{\partial t} = -W_{\mathrm{GSA}} N_1 + (W_{\mathrm{E}} + A_{21} + R_{21}) N_2 \end{cases} \tag{2.20}$$

where $W_{\mathrm{GSA}} = W^{\mathrm{p}}_{\mathrm{GSA}} + W^{\mathrm{s}}_{\mathrm{GSA}}$ is the total transition rate pertaining to the ground state absorption (GSA), $W_{\mathrm{E}} = W^{\mathrm{p}}_{\mathrm{E}} + W^{\mathrm{s}}_{\mathrm{E}}$ is the total transition rate pertaining to the stimulated emission (E), while $A_{21} = \tau_2^{-1}$ and $R_{21} = T_2^{-1}$ are the radiative and nonradiative decay rates for the $^6H_{13/2} \rightarrow {}^6H_{15/2}$ transition, respectively. The transition rates for the pump (p) and the signal (s) can be calculated as follows:

$$\begin{aligned} W^{\mathrm{p}}_{\mathrm{GSA}} &= \frac{\sigma_{12}(\nu_{\mathrm{p}})}{h\nu_{\mathrm{p}}} [P^{+}_{\mathrm{p}}(z,t) + P^{-}_{\mathrm{p}}(z,t)] i_{\mathrm{p}}(x,y) \\ W^{\mathrm{p}}_{\mathrm{E}} &= \frac{\sigma_{21}(\nu_{\mathrm{p}})}{h\nu_{\mathrm{p}}} [P^{+}_{\mathrm{p}}(z,t) + P^{-}_{\mathrm{p}}(z,t)] i_{\mathrm{p}}(x,y) \\ W^{\mathrm{s}}_{\mathrm{GSA}} &= \frac{\sigma_{12}(\nu_{\mathrm{s}})}{h\nu_{\mathrm{s}}} [P^{+}_{\mathrm{s}}(z,t) + P^{-}_{\mathrm{s}}(z,t)] i_{\mathrm{s}}(x,y) \\ W^{\mathrm{s}}_{\mathrm{E}} &= \frac{\sigma_{21}(\nu_{\mathrm{s}})}{h\nu_{\mathrm{s}}} [P^{+}_{\mathrm{s}}(z,t) + P^{-}_{\mathrm{s}}(z,t)] i_{\mathrm{s}}(x,y) \end{aligned}$$

where h is the Planck constant, ν_{p} is the pump frequency, ν_{s} is the signal frequency, $\sigma_{12}(\nu)$ and $\sigma_{21}(\nu)$ are the frequency-dependent absorption and emission cross sections, respectively, $P^{\pm}_{\mathrm{p}}$ is the forward/backward pump power and $P^{\pm}_{\mathrm{s}}$ is the forward/backward signal power, i_{p} and i_{s} are the normalized transverse intensity profiles of pump and signal beams, respectively. The previous system of differential equations (2.20) can be simplified because the sum of level populations is equal to the total

dopant concentration $N_{\mathrm{Dy}}(x,y,z) = N_1(x,y,z,t) + N_2(x,y,z,t)$:

$$\begin{cases} \dfrac{\partial N_2}{\partial t} = W_{\mathrm{GSA}} N_1 - (W_{\mathrm{E}} + A_{21} + R_{21}) N_2 \\ N_1(x,y,z,t) = N_{\mathrm{Dy}}(x,y,z) - N_2(x,y,z,t) \end{cases} \tag{2.21}$$

The propagation of the pump and signal optical beams is taken into account by the following nonlinear partial differential equations (PDEs):

$$\begin{cases} \dfrac{\partial P_{\mathrm{p}}^{+}}{\partial z} + \dfrac{1}{v_{\mathrm{g}}^{\mathrm{p}}} \dfrac{\partial P_{\mathrm{p}}^{+}}{\partial t} = [g_{\mathrm{p}}(z,t) - \alpha(\nu_{\mathrm{p}})] P_{\mathrm{p}}^{+} \\ \dfrac{\partial P_{\mathrm{p}}^{-}}{\partial z} - \dfrac{1}{v_{\mathrm{g}}^{\mathrm{p}}} \dfrac{\partial P_{\mathrm{p}}^{-}}{\partial t} = [-g_{\mathrm{p}}(z,t) + \alpha(\nu_{\mathrm{p}})] P_{\mathrm{p}}^{-} \\ \dfrac{\partial P_{\mathrm{s}}^{+}}{\partial z} + \dfrac{1}{v_{\mathrm{g}}^{\mathrm{s}}} \dfrac{\partial P_{\mathrm{s}}^{+}}{\partial t} = [g_{\mathrm{s}}(z,t) - \alpha(\nu_{\mathrm{s}})] P_{\mathrm{s}}^{+} + a_{\mathrm{sp}}(z,t) \\ \dfrac{\partial P_{\mathrm{s}}^{-}}{\partial z} - \dfrac{1}{v_{\mathrm{g}}^{\mathrm{s}}} \dfrac{\partial P_{\mathrm{s}}^{-}}{\partial t} = [-g_{\mathrm{s}}(z,t) + \alpha(\nu_{\mathrm{s}})] P_{\mathrm{s}}^{-} - a_{\mathrm{sp}}(z,t) \end{cases} \tag{2.22}$$

where

$$\begin{aligned} g_{\mathrm{p}}(z,t) &= -\sigma_{12}(\nu_{\mathrm{p}}) n_{1\mathrm{p}}(z,t) + \sigma_{21}(\nu_{\mathrm{p}}) n_{2\mathrm{p}}(z,t), \\ g_{\mathrm{s}}(z,t) &= -\sigma_{12}(\nu_{\mathrm{s}}) n_{1\mathrm{s}}(z,t) + \sigma_{21}(\nu_{\mathrm{s}}) n_{2\mathrm{s}}(z,t), \\ a_{\mathrm{sp}}(z,t) &= 2h\nu_{\mathrm{s}} B_{\mathrm{ase}} \sigma_{21}(\nu_{\mathrm{s}}) n_{2\mathrm{s}}(z,t), \end{aligned}$$

are the gain coefficient for the pump, the gain coefficient for the signal and the spontaneous emission term, respectively, $v_{\mathrm{g}}^{\mathrm{p}}$ and $v_{\mathrm{g}}^{\mathrm{s}}$ are the group velocities for the pump and the signal, respectively, $\alpha(\nu)$ is the frequency-dependent optical loss of the glass and B_{ase} is the equivalent noise bandwidth for the amplified spontaneous emission (ASE). The overlap integrals over the rare earth-doped region Ω_{d} between the ion populations

and the pump/signal optical modes are calculated as follows:

$$
\begin{aligned}
n_{1\mathrm{p}}(z,t) &= \int_{\Omega_\mathrm{d}} N_1(x,y,z,t) i_\mathrm{p}(x,y)\,\mathrm{d}x\mathrm{d}y \\
n_{2\mathrm{p}}(z,t) &= \int_{\Omega_\mathrm{d}} N_2(x,y,z,t) i_\mathrm{p}(x,y)\,\mathrm{d}x\mathrm{d}y \\
n_{1\mathrm{s}}(z,t) &= \int_{\Omega_\mathrm{d}} N_1(x,y,z,t) i_\mathrm{s}(x,y)\,\mathrm{d}x\mathrm{d}y \\
n_{2\mathrm{s}}(z,t) &= \int_{\Omega_\mathrm{d}} N_2(x,y,z,t) i_\mathrm{s}(x,y)\,\mathrm{d}x\mathrm{d}y
\end{aligned}
$$

Therefore, the actual spatial distribution of both the ion population and the electromagnetic field is taken into account.

In order to solve the previous PDEs (2.22), suitable boundary and initial conditions are imposed (see Fig. 2.4):

$$
\begin{aligned}
P_\mathrm{p}^+(0,t) &= P_{\mathrm{p}0}^+(t) \\
P_\mathrm{p}^-(L,t) &= P_{\mathrm{p}0}^-(t) \\
P_\mathrm{s}^+(0,t) &= R_1(\nu_\mathrm{s}) P_\mathrm{s}^-(0,t) \\
P_\mathrm{s}^-(L,t) &= R_2(\nu_\mathrm{s}) P_\mathrm{s}^+(L,t)
\end{aligned}
$$

where $z = 0$ and $z = L$ represent the endpoints of the laser cavity, $P_{\mathrm{p}0}^{\pm}(t)$ is the input forward/backward pump power signal, $R_1(\nu_\mathrm{s})$ is the first mirror reflectivity and $R_2(\nu_\mathrm{s})$ is the second mirror reflectivity. In addition, the system is considered to be initially at rest, therefore all rare earth ions are in the ground state and all the signals are zero everywhere:

$$
\begin{aligned}
N_1(x,y,z,0) &= N_{\mathrm{Dy}}(x,y,z) \\
N_2(x,y,z,0) &= 0 \\
P_\mathrm{p}^+(z,0) = P_\mathrm{p}^-(z,0) &= P_\mathrm{s}^+(z,0) = P_\mathrm{s}^-(z,0) = 0
\end{aligned}
$$

The time evolution of the generated optical pulses can be obtained as follows:

$$P_{\mathrm{s}}^{\mathrm{out}}(t) = [1 - R_2(\nu_{\mathrm{s}})]P_{\mathrm{s}}^{+}(L,t) \tag{2.23}$$

Description of the FDTD algorithm

In order to solve the PDEs (2.22) along with the rate equations (2.21), a suitable numerical algorithm must be employed. In this case, a finite-difference time-domain (FDTD) algorithm is chosen. First of all, the computational domain $\Omega = [0, L] \times [0, T]$ is divided into a number of grid points, by choosing a space step size Δz and a time step size Δt:

$$z_0 = 0, z_1 = \Delta z, \ldots, z_i = i\Delta z, \ldots, z_{N_{\mathrm{z}}} = N_{\mathrm{z}}\Delta z = L$$
$$t_0 = 0, t_1 = \Delta t, \ldots, t_j = j\Delta t, \ldots, t_{N_{\mathrm{t}}} = N_{\mathrm{t}}\Delta t = T$$

Then, the partial derivatives are approximated by employing a finite difference scheme. For example, let us consider the forward pump power $P_{\mathrm{p}}^{+}(z,t)$, for which it is natural to use a first-order forward difference at position $z = z_i$:

$$\left.\frac{\partial P_{\mathrm{p}}^{+}}{\partial z}\right|_{(z_i,t_j)} \approx \frac{P_{\mathrm{p}}^{+}(z_{i+1},t_j) - P_{\mathrm{p}}^{+}(z_i,t_j)}{\Delta z}$$

On the other hand, since the function is known at the previous time step, it is convenient to use a first-order backward difference at time $t = t_j$.

$$\left.\frac{\partial P_{\mathrm{p}}^{+}}{\partial t}\right|_{(z_i,t_j)} \approx \frac{P_{\mathrm{p}}^{+}(z_i,t_j) - P_{\mathrm{p}}^{+}(z_i,t_{j-1})}{\Delta t}$$

These expressions are put in the first equation of PDEs (2.22), yielding:

$$\frac{P_{\mathrm{p}}^{+}(z_{i+1},t_j) - P_{\mathrm{p}}^{+}(z_i,t_j)}{\Delta z} + \frac{1}{v_{\mathrm{g}}^{\mathrm{p}}}\frac{P_{\mathrm{p}}^{+}(z_i,t_j) - P_{\mathrm{p}}^{+}(z_i,t_{j-1})}{\Delta t} = [g_{\mathrm{p}}(z_i,t_j) - \alpha(\nu_{\mathrm{p}})]P_{\mathrm{p}}^{+}(z_i,t_j)$$

which can be solved for $P_{\mathrm{p}}^{+}(z_{i+1}, t_j)$:

$$P_{\mathrm{p}}^{+}(z_{i+1}, t_j) = \left(1 - \frac{\Delta z}{v_{\mathrm{g}}^{\mathrm{p}} \Delta t}\right) P_{\mathrm{p}}^{+}(z_i, t_j) + \frac{\Delta z}{v_{\mathrm{g}}^{\mathrm{p}} \Delta t} P_{\mathrm{p}}^{+}(z_i, t_{j-1}) + [g_{\mathrm{p}}(z_i, t_j) - \alpha(\nu_{\mathrm{p}})] P_{\mathrm{p}}^{+}(z_i, t_j) \Delta z$$

In order for the algorithm to be numerically stable, the following condition on the Courant number $C = \frac{v_{\mathrm{g}}^{\mathrm{p}} \Delta t}{\Delta z}$ must be met:

$$C > 1 \tag{2.24}$$

Intuitively, this condition means that the chosen space step size Δz has to be smaller than the distance $v_{\mathrm{g}}^{\mathrm{p}} \Delta t$ traveled by light during the time Δt. The discretization of the backward pump power $P_{\mathrm{p}}^{-}(z, t)$ is similar, except that a first-order backward difference at position $z = z_i$ is employed:

$$\left.\frac{\partial P_{\mathrm{p}}^{-}}{\partial z}\right|_{(z_i, t_j)} \approx \frac{P_{\mathrm{p}}^{-}(z_i, t_j) - P_{\mathrm{p}}^{-}(z_{i-1}, t_j)}{\Delta z}$$

from which it follows that:

$$P_{\mathrm{p}}^{-}(z_{i-1}, t_j) = \left(1 - \frac{\Delta z}{v_{\mathrm{g}}^{\mathrm{p}} \Delta t}\right) P_{\mathrm{p}}^{-}(z_i, t_j) + \frac{\Delta z}{v_{\mathrm{g}}^{\mathrm{p}} \Delta t} P_{\mathrm{p}}^{-}(z_i, t_{j-1}) - [-g_{\mathrm{p}}(z_i, t_j) + \alpha(\nu_{\mathrm{p}})] P_{\mathrm{p}}^{-}(z_i, t_j) \Delta z$$

The discretized equations for the forward and backward signal powers are:

$$\begin{aligned} P_{\mathrm{s}}^{+}(z_{i+1}, t_j) &= \left(1 - \frac{\Delta z}{v_{\mathrm{g}}^{\mathrm{s}} \Delta t}\right) P_{\mathrm{s}}^{+}(z_i, t_j) + \frac{\Delta z}{v_{\mathrm{g}}^{\mathrm{s}} \Delta t} P_{\mathrm{s}}^{+}(z_i, t_{j-1}) \\ &\quad + [g_{\mathrm{s}}(z_i, t_j) - \alpha(\nu_{\mathrm{s}})] P_{\mathrm{s}}^{+}(z_i, t_j) \Delta z + a_{\mathrm{sp}}(z_i, t_j) \Delta z \\ P_{\mathrm{s}}^{-}(z_{i-1}, t_j) &= \left(1 - \frac{\Delta z}{v_{\mathrm{g}}^{\mathrm{s}} \Delta t}\right) P_{\mathrm{s}}^{-}(z_i, t_j) + \frac{\Delta z}{v_{\mathrm{g}}^{\mathrm{s}} \Delta t} P_{\mathrm{s}}^{-}(z_i, t_{j-1}) \\ &\quad - [-g_{\mathrm{s}}(z_i, t_j) + \alpha(\nu_{\mathrm{s}})] P_{\mathrm{s}}^{-}(z_i, t_j) \Delta z + a_{\mathrm{sp}}(z_i, t_j) \Delta z \end{aligned}$$

The rate equations are defined on the 4D computational domain $\Lambda = [-\frac{X}{2}, \frac{X}{2}] \times [-\frac{Y}{2}, \frac{Y}{2}] \times [0, L] \times [0, T]$, therefore two additional space step sizes Δx and Δy are needed. The related sampling points are:

$$x_{-\frac{N_\mathrm{x}-1}{2}}, \ldots, x_{-1} = -\Delta x, x_0 = 0, x_1 = \Delta x, \ldots, x_k = k\Delta x, \ldots, x_{\frac{N_\mathrm{x}-1}{2}} = \frac{N_\mathrm{x}-1}{2}\Delta x = \frac{X}{2}$$
$$y_{-\frac{N_\mathrm{y}-1}{2}}, \ldots, y_{-1} = -\Delta y, y_0 = 0, y_1 = \Delta y, \ldots, y_l = l\Delta y, \ldots, y_{\frac{N_\mathrm{y}-1}{2}} = \frac{N_\mathrm{y}-1}{2}\Delta y = \frac{Y}{2}$$

The only partial derivative to be approximated with a finite difference is the time derivative of the second level population $N_2(x, y, z, t)$, for which it is natural to use a first-order forward-time scheme:

$$\left.\frac{\partial N_2}{\partial t}\right|_{(x_k, y_l, z_i, t_j)} \approx \frac{N_2(x_k, y_l, z_i, t_{j+1}) - N_2(x_k, y_l, z_i, t_j)}{\Delta t}$$

By exploiting this relation, the rate equations become:

$$\begin{cases} N_2(x_k, y_l, z_i, t_{j+1}) = W_\mathrm{GSA}(x_k, y_l, z_i, t_j) N_1(x_k, y_l, z_i, t_j)\Delta t \\ \qquad\qquad\qquad\qquad + [1 - (W_\mathrm{E}(x_k, y_l, z_i, t_j) + A_{21} + R_{21})\Delta t] N_2(x_k, y_l, z_i, t_j) \\ N_1(x_k, y_l, z_i, t_{j+1}) = N_\mathrm{Dy}(x_k, y_l, z_i) - N_2(x_k, y_l, z_i, t_{j+1}) \end{cases}$$

The evaluation of the transition rates is straightforward:

$$W^\mathrm{p}_\mathrm{GSA}(x_k, y_l, z_i, t_j) = \frac{\sigma_{12}(\nu_\mathrm{p})}{h\nu_\mathrm{p}}[P^+_\mathrm{p}(z_i, t_j) + P^-_\mathrm{p}(z_i, t_j)] i_\mathrm{p}(x_k, y_l)$$
$$W^\mathrm{p}_\mathrm{E}(x_k, y_l, z_i, t_j) = \frac{\sigma_{21}(\nu_\mathrm{p})}{h\nu_\mathrm{p}}[P^+_\mathrm{p}(z_i, t_j) + P^-_\mathrm{p}(z_i, t_j)] i_\mathrm{p}(x_k, y_l)$$
$$W^\mathrm{s}_\mathrm{GSA}(x_k, y_l, z_i, t_j) = \frac{\sigma_{12}(\nu_\mathrm{s})}{h\nu_\mathrm{s}}[P^+_\mathrm{s}(z_i, t_j) + P^-_\mathrm{s}(z_i, t_j)] i_\mathrm{s}(x_k, y_l)$$
$$W^\mathrm{s}_\mathrm{E}(x_k, y_l, z_i, t_j) = \frac{\sigma_{21}(\nu_\mathrm{s})}{h\nu_\mathrm{s}}[P^+_\mathrm{s}(z_i, t_j) + P^-_\mathrm{s}(z_i, t_j)] i_\mathrm{s}(x_k, y_l)$$

Finally, the discretized boundary and initial conditions are as follows:

$$
\begin{aligned}
P_{\mathrm{p}}^{+}(0,t_j) &= P_{\mathrm{p0}}^{+}(t_j) \\
P_{\mathrm{p}}^{-}(L,t_j) &= P_{\mathrm{p0}}^{-}(t_j) \\
P_{\mathrm{s}}^{+}(0,t_{j+1}) &= R_1(\nu_{\mathrm{s}})P_{\mathrm{s}}^{-}(0,t_j) \\
P_{\mathrm{s}}^{-}(L,t_{j+1}) &= R_2(\nu_{\mathrm{s}})P_{\mathrm{s}}^{+}(L,t_j) \\
N_1(x_k,y_l,z_i,0) &= N_{\mathrm{Dy}}(x_k,y_l,z_i) \\
N_2(x_k,y_l,z_i,0) &= 0 \\
P_{\mathrm{p}}^{+}(z_i,0) = P_{\mathrm{p}}^{-}(z_i,0) &= P_{\mathrm{s}}^{+}(z_i,0) = P_{\mathrm{s}}^{-}(z_i,0) = 0
\end{aligned}
$$

2.3 Particle swarm optimization (PSO) algorithm

The particle swarm optimization (PSO) algorithm is a global search numerical method, inspired by the social behavior exhibited by a variety of animals during their search for food, e.g. bees, fishes, birds [44–47]. In the PSO algorithm, a population of N tentative solutions or particles corresponds to the swarm of bees. The tentative solutions are updated in the multidimensional solution space with the aim of optimizing a suitable fitness function. For a D-dimensional search space, the position of each particle is identified by a D-dimensional vector $\mathbf{p}_j$, which constitutes the tentative solution (a set of tentative values of the independent variables). The fitness function is optimized (e.g. maximized or minimized) during the execution. Each particle trajectory is updated till the convergence criterion is reached. The particle trajectory depends on i) the location in the solution space where the best fitness value is found by the single particle, called personal best $\mathbf{p}^{\mathrm{PB}}$, and ii) the best location found by the entire swarm, called global best $\mathbf{p}^{\mathrm{GB}}$. The movement of each particle is affected by three factors: i) the cognitive factor, related to the location in the solution space corresponding to the best value of objective function for the considered particle; ii) the social factor, related to the location corresponding to the best value of objective function for the whole

swarm; iii) the inertial factor, i.e. a suitable resistance to the change of the particle direction. Each of these factors is weighted by an ad hoc parameter: the cognitive parameter c_1, the social parameter c_2 and the inertial weight w.

The change of the current particle position is obtained by applying a velocity, $\mathbf{v}_j$, which depends on both the personal experience and the collective experience of the swarm. The position and the velocity of the particle are updated at the $n+1$ iteration according to the following equations [44]:

$$\mathbf{v}_j(n+1) = \chi[\mathbf{v}_j(n) + c_1 r_1(\mathbf{p}_j(n)^{\mathrm{PB}} - \mathbf{p}_j(n)) + c_2 r_2(\mathbf{p}^{\mathrm{GB}} - \mathbf{p}_j(n))]$$
$$\mathbf{p}_j(n+1) = \mathbf{p}_j(n) + \mathbf{v}_j(n+1)$$

with $j = 1, 2, \ldots, N$. The constriction factor C_{F} is given by:

$$C_{\mathrm{F}} = \frac{2}{|2 - \chi - \sqrt{\chi^2 - 4\chi}|}$$

where $\chi = c_1 + c_2$ and $\chi > 4$. r_1 and r_2 are two random numbers uniformly distributed in the range $[0, 1]$, employed to obtain an efficient search. Once the convergence criterion is reached, the PSO procedure ends and the global best position $\mathbf{p}^{\mathrm{GB}}$ is the optimized solution, i.e. the position where the fitness is maximized or minimized.

Chapter 3

Design of a Dy^{3+}-doped chalcogenide master oscillator power amplifier (MOPA)

3.1 Introduction

This chapter describes the design of a middle-infrared fiber laser based on a dysprosium-doped chalcogenide glass, Dy^{3+}:$Ga_5Ge_{20}Sb_{10}S_{65}$. To obtain a high efficiency, the fiber laser is followed by an optical amplifier, exploiting a master oscillator power amplifier (MOPA) configuration. The MOPA pump and signal wavelengths are 1709 nm and 4384 nm, respectively. Spectroscopic parameters measured on preliminary samples of chalcogenide glasses are taken into account to fulfill realistic simulations. The MOPA emission is maximized by applying a particle swarm optimization (PSO) approach. For the dysprosium concentration 6×10^{25} ions/m^3 and the input pump power of 3 W, an output power of 637 mW can be obtained for optical fiber losses close to 1 dB m^{-1}. The optimized MOPA configuration allows a laser efficiency larger than 21 %.

Among all the rare earths, dysprosium is one of the most promising candidate for the generation of coherent radiation at $\lambda = 4.4\,\mu m$, by exploiting the $^6H_{11/2} \rightarrow {}^6H_{13/2}$ laser transition. However, high efficiencies cannot be easily reached since the lower

laser level $^6H_{13/2}$ has a long lifetime [12]. Different solutions which employ an auxiliary idler laser signal have been proposed in literature [12,48,49]. Cascade lasing, involving both the $^6H_{11/2} \rightarrow {}^6H_{13/2}$ and $^6H_{13/2} \rightarrow {}^6H_{15/2}$ transitions, allows the $^6H_{13/2}$ level depopulation and the increase of the $^6H_{15/2}$ ground state population [12]. Both these effects are useful to increase $\lambda_{s1} = 4.4$–$4.8\,\mu m$ wavelength emission. Direct pumping into the upper laser level $^6H_{11/2}$ at $\lambda_p = 1.7\,\mu m$ wavelength can be used in order to promote the dysprosium ions in the $^6H_{11/2}$ upper laser level. A first couple of fiber Bragg gratings (FBGs) are designed to obtain the signal lasing λ_{s1}. A second couple of FBGs allows a simultaneous secondary lasing at $\lambda_{s2} = 2.7$–$3.4\,\mu m$. Therefore, the purpose of this second lasing (idler) is the increase of signal intensity at the wavelength λ_{s1}. The aforesaid approach was predicted in [12]. A similar cascade configuration was simulated in [48]. In both cases, no experimental work definitely demonstrated the set-up feasibility. In fact, these pumping strategies are challenging, requiring the construction of two pairs of resonant cavities and thus two pairs of fiber Bragg gratings and the handling of soft glasses.

Rare earth-doped chalcogenide optical fiber fabrication exhibits different types of obstacles concerning the cross section shaping. Defects originated by glass crystallization during their drawing can occur due to the not completely mature technology, limiting the design of the PCF transversal microstructure. Recently, strong improvements have been reached. For example, losses have been reduced to few $dB\,m^{-1}$. While very low losses are required for supercontinuum generation [50], efficient lasing simply requires the loss/gain ratio reduction. A good trade-off, can be reached i) by optimizing the host material in order to obtain a good dopant solubility even with losses of few $dB\,m^{-1}$ and ii) by refining the laser design. Therefore, the feasibility investigation of chalcogenide optical fiber lasers is necessary.

In [49] the authors numerically compared different pumping techniques for dysprosium-doped chalcogenide fiber lasers. The investigated configurations included different approaches: the pumping scheme proposed in [12]; a simple dysprosium-doped fiber, by directly launching the pump power and by exploiting Fresnel reflection at the chalco-

genide glass-air interface; a pumping scheme based on bulk optical elements (beam splitter and mirrors); an all-fiber structure. A laser efficiency close to $\eta = 15\,\%$ was simulated for a fiber laser cavity with a dysprosium concentration $N_{\mathrm{Dy}} = 7 \times 10^{25}\,\mathrm{ions/m^3}$ and close to $\eta = 7\,\%$ for a dysprosium concentration $N_{\mathrm{Dy}} = 3 \times 10^{25}\,\mathrm{ions/m^3}$.

In this chapter, a new approach in order to obtain efficient lasing in dysprosium-doped chalcogenide optical fiber is proposed. A master oscillator power amplifier (MOPA) configuration is employed. It allows high pump power absorption inside the laser cavity and high fabrication easiness, since it requires a single pump. The long lifetime of the $^6\mathrm{H}_{13/2}$ energy level leads to a weak population inversion, severely affecting the slope efficiency of fiber cavity laser configuration, even when high pump powers are employed. This drawback is worsened if the fiber cavity exhibits high losses. Preliminary simulations confirm the poor performance of this approach. On the other end, optical amplification can be obtained even if the population inversion is weak. This suggests that, by employing a fiber amplifier of proper length, the low output of the laser stage can be boosted to a much higher level, enhancing the overall efficiency of the system. The MOPA configuration is ideal for this application [51]. It is composed of a FBG-based fiber laser and a fiber amplifier in cascade, i.e. the amplifier is integrated on the same fiber after the laser cavity as in [51]. The drawbacks related to the amplifier noise are not relevant for practical mid-IR applications. The pump and signal wavelengths are $\lambda_{\mathrm{p}} = 1709\,\mathrm{nm}$ and $\lambda_{\mathrm{s}} = 4384\,\mathrm{nm}$, respectively. A single-mode photonic crystal fiber, which allows good light confinement, is employed. The chalcogenide glass allows the light propagation at the wavelength $\lambda_{\mathrm{s}} = 4384\,\mathrm{nm}$. The PCF technology is considered instead of a conventional fiber fabrication process i) in order to maximize the mode area of the pump, thus reducing the thermal load density and avoiding nonlinear effects in the chalcogenide glass; ii) to obtain a high beam quality, not obtainable with QCL sources. This choice, for the simulated power levels, is not strictly necessary and a similar set-up could be designed by considering a simpler conventional fiber. This could allow to avoid potential technological drawbacks. However, the simulated fiber section geometry is pertaining to a fabricated chalcogenide

PCF [52]. Finally, to maximize the output power, the device is optimized by means of a particle swarm optimization (PSO) algorithm [45, 53, 54].

The theoretical model is described in section 2.1.1.

3.2 MOPA design

Fig. 3.1 illustrates the MOPA configuration. It is composed of a fiber laser cavity obtained by employing two suitable FBGs mirror. A fiber amplifier is integrated after the laser cavity, via a proper design or by a subsequent splicing [55, 56]. Moreover, a proper angle cleaving of fiber end can make negligible the Fresnel reflection at output glass-air interface. The pump and signal wavelengths are $\lambda_p = 1709\,\text{nm}$ and $\lambda_s = 4384\,\text{nm}$, respectively. Pumping at 1709 nm can be performed with Er:YLF lasers [57] or with laser diodes [58] or QCLs.

The chalcogenide glass allows light propagation for wavelengths up to $\lambda = 15\,\mu\text{m}$; therefore propagation at $\lambda_s = 4384\,\text{nm}$ occurs without drawbacks. The PCF technology is considered instead of the conventional fiber fabrication process in order to maximize the mode area of the pump [59]. This allows to reduce the thermal load density, avoiding nonlinear effects in the chalcogenide glass. In particular, the fiber cross section is made of three rings of air holes surrounding the rare earth-doped solid core [17, 60]. The fabrication of this kind of fiber was reported in [52]. Table 3.1 reports both the geometrical [17, 52] and spectroscopic parameters employed in the simulation; nominal values for all MOPA parameters are also included. The emission and absorption cross sections and the fiber losses refer to fabricated glass samples. Fig. 3.2 illustrates the emission and absorption cross sections close to 1709 nm and 4384 nm, which were both evaluated using the Futchbauer-Ladenburg relation from fluorescence measurements. The 1.7 µm absorption cross-section has been calculated from the absorption spectrum, the 4.3 µm excited state absorption cross-section has been calculated from the emission cross-section by using the McCumber formula. Similar values were calculated for selenide matrix [12, 49, 61]. The fiber losses can be reduced till $\alpha = 1\,\text{dB}\,\text{m}^{-1}$

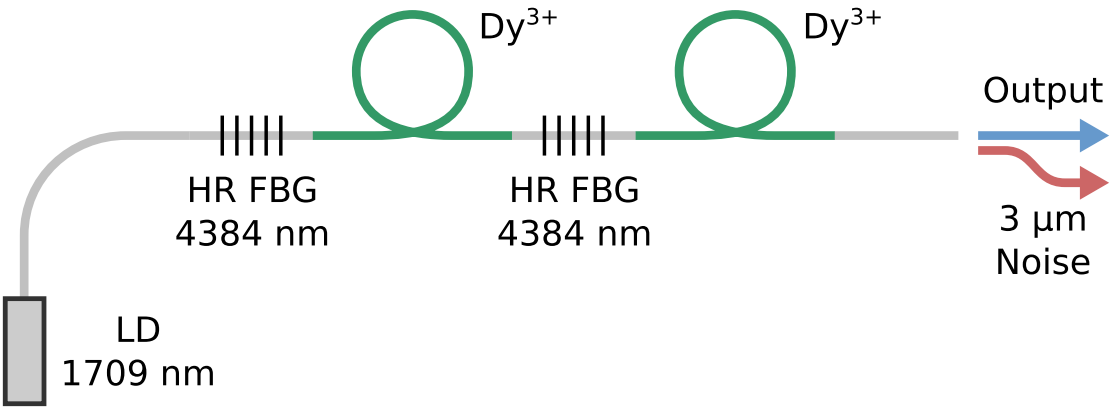

Figure 3.1: Schematic of the laser cavity and the following amplifier section.

Table 3.1: Spectroscopic parameters of the dysprosium ions in chalcogenide glass, geometrical parameters of the PCF and nominal values of MOPA parameters

Parameter	Value
Lifetime of level 2, τ_2	7.03 ms
Lifetime of level 3, τ_3	1.48 ms
Branching ratio for $3 \rightarrow 2$ transition, β_{32}	0.088
Air-hole diameter, d	3.2 µm
Pitch, Λ	8 µm
Doped region radius, R_d	4 µm
Nominal laser cavity length, L_1	0.3 m
Nominal amplifier length, L_2	1 m
Nominal dopant concentration, N_{Dy}	6×10^{25} ions/m^3
Nominal FBG1 reflectivity, R_1	99 %
Nominal FBG2 reflectivity, R_2	70 %
Pump power, $P_{\mathrm{p}}(0)$	0.5–5 W

via an accurate glass purification [18, 62]. These loss values are considered as feasible ones. Perfectly matched layers are used to avoid the reflections into the computational domain of the outgoing waves. The thickness of the PML layers is $t_{\mathrm{PML}} = 12\,\mu\mathrm{m}$.

In Fig. 3.3 the fiber laser output signal $P_{\mathrm{s}}(L_1)$ versus dopant concentration N_{Dy} is shown for different input pump powers $P_{\mathrm{p}}(0) = 0.5\,\mathrm{W}$ (dotted curve), $P_{\mathrm{p}}(0) = 1\,\mathrm{W}$ (dashed curve), $P_{\mathrm{p}}(0) = 3\,\mathrm{W}$ (dash-dot curve), $P_{\mathrm{p}}(0) = 5\,\mathrm{W}$ (solid curve); laser cavity length $L_1 = 0.3\,\mathrm{m}$; first fiber grating FBG_1 $R_1 = 99\,\%$; second fiber grating FBG_2 reflectivity $R_2 = 70\,\%$. These results refer to the laser cavity alone, without the cascade amplification stage. Pump powers higher than $P_{\mathrm{p}}(0) = 5\,\mathrm{W}$ are not considered since deleterious nonlinear effects could rise, although the PCF section allows a reduction

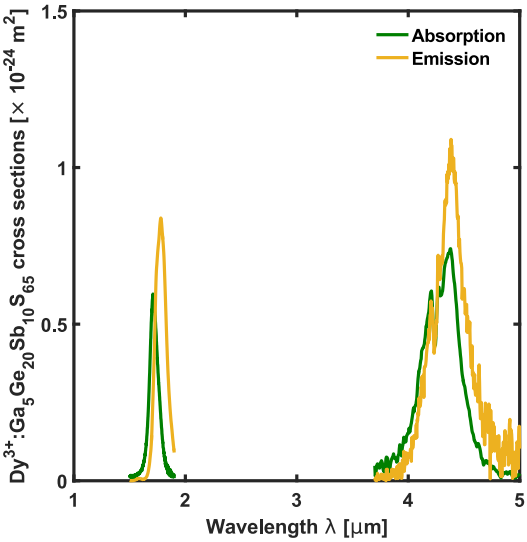

Figure 3.2: Dy^{3+}:$Ga_5Ge_{20}Sb_{10}S_{65}$ glass absorption and emission cross-sections.

of pump power density. By employing the laser without cascade amplifier, even by considering high dopant concentrations, only few milliwatts of output power $P_s(L_1)$ can be obtained. It is worthwhile noting that an increasing behavior of the output power $P_s(L_1)$ is more apparent for dysprosium concentrations higher than $N_{Dy} = 6 \times 10^{25}$ ions/m^3. Unfortunately, these values should be avoided since they might cause glass devitrification.

Fig. 3.4 shows the residual (i.e. not absorbed) pump power $P_p(L_1)$ versus dopant concentration for the same parameters of Fig. 3.3. For high input pump powers, the residual pump power is not negligible, e.g. about 83 % of $P_p(0) = 5$ W is wasted. A decreasing behavior of the curves is obtained for concentrations higher than $N_{Dy} = 6 \times 10^{25}$ ions/m^3 (not allowed). To overcome these problems, the MOPA configuration is exploited [51].

Fig. 3.5 shows the optical signal power $P_s(L)$ of the Dy^{3+}-doped MOPA versus laser cavity length L_1, for different input pump powers; fiber amplifier length $L_2 = 1$ m; dopant concentration $N_{Dy} = 6 \times 10^{25}$ ions/m^3; first mirror reflectivity $R_1 = 99$ %; second mirror reflectivity $R_2 = 70$ %. For low pump powers, $P_p(0) = 0.5$–1 W, the output power is almost constant for the laser cavity length L_1 from $L_1 = 5$ cm to $L_1 = 25$ cm, while it decreases for longer cavities. For high pump powers, $P_p(0) =$

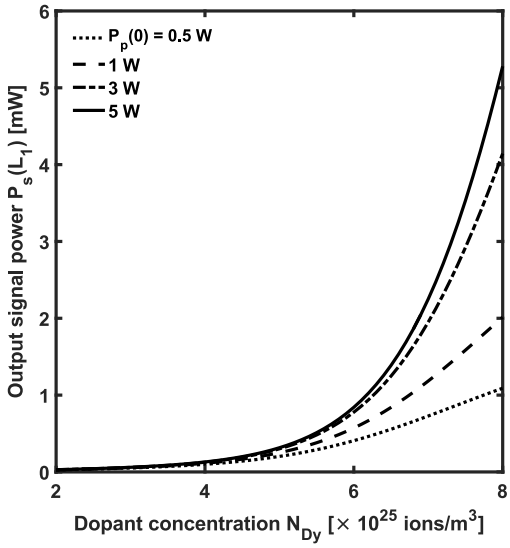

Figure 3.3: Output signal power $P_{\mathrm{s}}(L_1)$ of the Dy^{3+}-doped fiber laser without amplification stage versus dopant concentration N_{Dy}, for different input pump powers $P_{\mathrm{p}}(0) = 0.5\,\mathrm{W}$ (dotted curve), $P_{\mathrm{p}}(0) = 1\,\mathrm{W}$ (dashed curve), $P_{\mathrm{p}}(0) = 3\,\mathrm{W}$ (dash-dot curve), $P_{\mathrm{p}}(0) = 5\,\mathrm{W}$ (solid curve). Laser cavity length $L_1 = 0.3\,\mathrm{m}$; first mirror reflectivity $R_1 = 99\,\%$; second mirror reflectivity $R_2 = 70\,\%$.

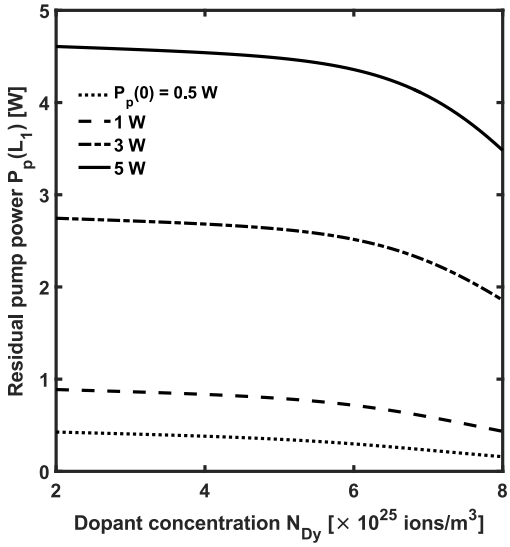

Figure 3.4: Residual pump power $P_{\mathrm{p}}(L_1)$ of the Dy^{3+}-doped fiber laser without amplification stage versus dopant concentration N_{Dy}, for different input pump powers $P_{\mathrm{p}}(0) = 0.5\,\mathrm{W}$ (dotted curve), $P_{\mathrm{p}}(0) = 1\,\mathrm{W}$ (dashed curve), $P_{\mathrm{p}}(0) = 3\,\mathrm{W}$ (dash-dot curve), $P_{\mathrm{p}}(0) = 5\,\mathrm{W}$ (solid curve). Laser cavity length $L_1 = 0.3\,\mathrm{m}$; first mirror reflectivity $R_1 = 99\,\%$; second mirror reflectivity $R_2 = 70\,\%$.

2–5 W, it increases by increasing the cavity length L_1 and reaches the maximum close to $L_1 = 30\,\mathrm{cm}$.

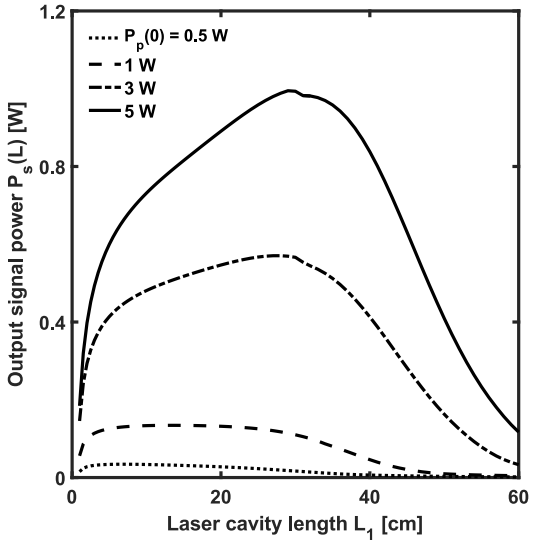

Figure 3.5: Optical signal power $P_{\mathrm{s}}(L)$ of the Dy^{3+}-doped MOPA versus laser cavity length L_1, for different input pump powers $P_{\mathrm{p}}(0) = 0.5\,\mathrm{W}$ (dotted curve), $P_{\mathrm{p}}(0) = 1\,\mathrm{W}$ (dashed curve), $P_{\mathrm{p}}(0) = 3\,\mathrm{W}$ (dash-dot curve), $P_{\mathrm{p}}(0) = 5\,\mathrm{W}$ (solid curve). Fiber amplifier length $L_2 = 1\,\mathrm{m}$; dopant concentration $N_{\mathrm{Dy}} = 6 \times 10^{25}\,\mathrm{ions/m^3}$; first mirror reflectivity $R_1 = 99\,\%$; second mirror reflectivity $R_2 = 70\,\%$.

Fig. 3.6 shows the optical signal power $P_{\mathrm{s}}(L)$ of the Dy^{3+}-doped MOPA versus fiber amplifier length L_2, for different input pump powers; laser cavity length $L_1 = 0.3\,\mathrm{m}$; dopant concentration $N_{\mathrm{Dy}} = 6 \times 10^{25}\,\mathrm{ions/m^3}$; first mirror reflectivity $R_1 = 99\,\%$; second mirror reflectivity $R_2 = 70\,\%$. For short fibers, the power increases with the length and reaches the maximum for lengths in the range from $L_2 = 90\,\mathrm{cm}$ to about $L_2 = 110\,\mathrm{cm}$. After $L_2 = 110\,\mathrm{cm}$, the power decreases since the pump is almost completely absorbed, therefore optical attenuation is predominant with respect to amplification.

Fig. 3.7 illustrates the output signal power $P_{\mathrm{s}}(L)$ of the Dy^{3+}-doped MOPA versus laser cavity length L_1 and fiber amplifier length L_2. The input pump power is $P_{\mathrm{p}}(0) = 3\,\mathrm{W}$, the dopant concentration is $N_{\mathrm{Dy}} = 6 \times 10^{25}\,\mathrm{ions/m^3}$, the first mirror reflectivity is $R_1 = 99\,\%$, while the second mirror reflectivity is $R_2 = 70\,\%$. It allows a quick identification of the best MOPA configuration via a three-dimensional plot in which the origin of the axes is suitably chosen.

Fig. 3.8 depicts the optical signal power $P_{\mathrm{s}}(L)$ of the Dy^{3+}-doped MOPA versus

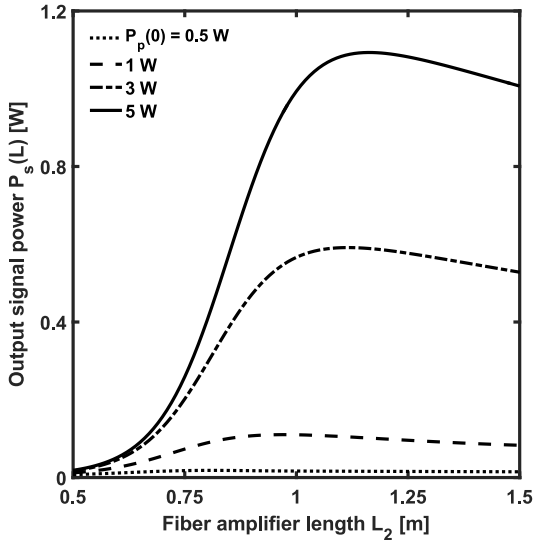

Figure 3.6: Optical signal power $P_{\mathrm{s}}(L)$ of the Dy^{3+}-doped MOPA versus fiber amplifier length L_2, for different input pump powers; laser cavity length $L_1 = 0.3\,\mathrm{m}$; dopant concentration $N_{\mathrm{Dy}} = 6 \times 10^{25}\,\mathrm{ions/m^3}$; first mirror reflectivity $R_1 = 99\,\%$; second mirror reflectivity $R_2 = 70\,\%$.

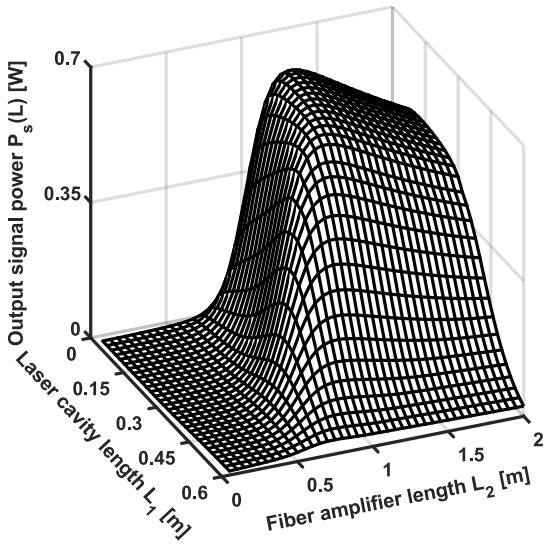

Figure 3.7: Output signal power $P_{\mathrm{s}}(L)$ of the Dy^{3+}-doped MOPA versus laser cavity length L_1 and fiber amplifier length L_2. Input pump power $P_{\mathrm{p}}(0) = 3\,\mathrm{W}$; dopant concentration $N_{\mathrm{Dy}} = 6 \times 10^{25}\,\mathrm{ions/m^3}$; first mirror reflectivity $R_1 = 99\,\%$; second mirror reflectivity $R_2 = 70\,\%$.

dopant concentration N_{Dy}, for different input pump powers; laser cavity length $L_1 = 0.3\,\mathrm{m}$; fiber amplifier length $L_2 = 1\,\mathrm{m}$; first mirror reflectivity $R_1 = 99\,\%$; second mirror reflectivity $R_2 = 70\,\%$. The output power increases by increasing the dopant

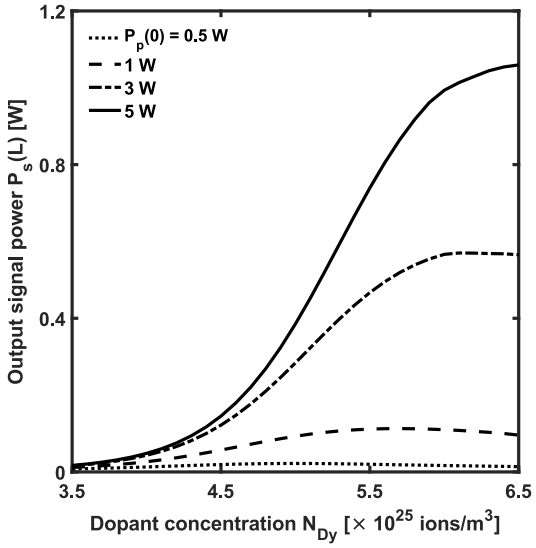

Figure 3.8: Optical signal power $P_{\mathrm{s}}(L)$ of the Dy^{3+}-doped MOPA versus dopant concentration N_{Dy}, for different input pump powers $P_{\mathrm{p}}(0) = 0.5\,\mathrm{W}$ (dotted curve), $P_{\mathrm{p}}(0) = 1\,\mathrm{W}$ (dashed curve), $P_{\mathrm{p}}(0) = 3\,\mathrm{W}$ (dash-dot curve), $P_{\mathrm{p}}(0) = 5\,\mathrm{W}$ (solid curve). Laser cavity length $L_1 = 0.3\,\mathrm{m}$; fiber amplifier length $L_2 = 1\,\mathrm{m}$; first mirror reflectivity $R_1 = 99\,\%$; second mirror reflectivity $R_2 = 70\,\%$.

concentration. Efficiencies close to $\eta = 8\,\%$ can be achieved for dopant concentrations close to $N_{\mathrm{Dy}} = 5 \times 10^{25}\,\mathrm{ions/m^3}$, below glass devitrification limit.

Fig. 3.9 depicts the optical signal power $P_{\mathrm{s}}(L)$ of the Dy^{3+}-doped MOPA versus second mirror reflectivity R_2, for different input pump powers $P_{\mathrm{p}}(0) = 0.5\,\mathrm{W}$ (dotted curve), $P_{\mathrm{p}}(0) = 1\,\mathrm{W}$ (dashed curve), $P_{\mathrm{p}}(0) = 3\,\mathrm{W}$ (dash-dot curve), $P_{\mathrm{p}}(0) = 5\,\mathrm{W}$ (solid curve); laser cavity length $L_1 = 0.3\,\mathrm{m}$; fiber amplifier length $L_2 = 1\,\mathrm{m}$; dopant concentration $N_{\mathrm{Dy}} = 6 \times 10^{25}\,\mathrm{ions/m^3}$; first mirror reflectivity $R_1 = 99\,\%$. The output signal is nearly constant for all the pump powers and changes only for very low or very high reflectivities.

3.3 Refinement of MOPA via particle swarm optimization

The high number of parameters of the MOPA configuration allows excellent design flexibility. Unfortunately, this makes the MOPA optimization very difficult if a trial-

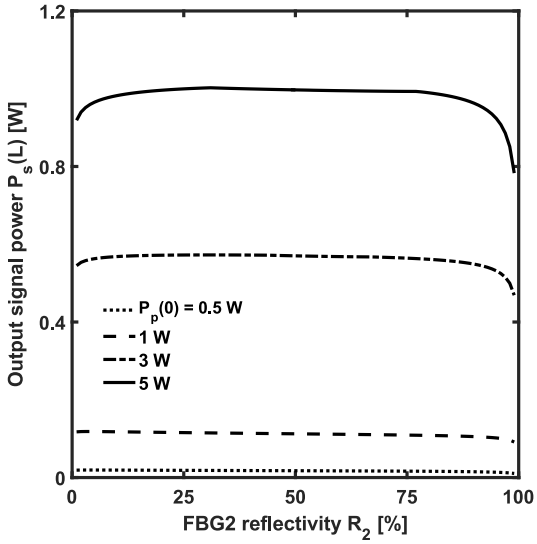

Figure 3.9: Optical signal power $P_\mathrm{s}(L)$ of the Dy^{3+}-doped MOPA versus second mirror reflectivity R_2, for different input pump powers $P_\mathrm{p}(0) = 0.5\,\mathrm{W}$ (dotted curve), $P_\mathrm{p}(0) = 1\,\mathrm{W}$ (dashed curve), $P_\mathrm{p}(0) = 3\,\mathrm{W}$ (dash-dot curve), $P_\mathrm{p}(0) = 5\,\mathrm{W}$ (solid curve). Laser cavity length $L_1 = 0.3\,\mathrm{m}$; fiber amplifier length $L_2 = 1\,\mathrm{m}$; dopant concentration $N_\mathrm{Dy} = 6 \times 10^{25}\,\mathrm{ions/m^3}$; first mirror reflectivity $R_1 = 99\,\%$.

Table 3.2: Parameters and search ranges used in PSO algorithm

Parameter	Value/Solution space limits
Solution space dimension	4
Number of particles	40
Iteration limit	40
Laser cavity length L_1	1–80 cm
Amplifier length L_2	1–200 cm
Dopant concentration N_Dy	1×10^{25}–$6 \times 10^{25}\,\mathrm{ions/m^3}$
FBG1 reflectivity R_1	99 %
FBG2 reflectivity R_2	1–99 %
Pump power $P_\mathrm{p}(0)$	3 W

and-error approach is used, i.e. by varying a single parameter at a time. In fact, the optimization of the amplifier, i.e. of the overall source, depends nonlinearly on its input signal and pump powers. These powers must be evaluated as output of the first laser stage. To overcome this problem, the Particle Swarm Optimization approach is employed to globally optimize the optical source. It is an evolutionary optimization technique inspired by the social behavior of a swarm of bees during their food-searching activities. It is suitable for multi-core CPU processing [45, 53, 54].

Table 3.3: PSO optimized MOPA

Parameter	Value for $\alpha = 1\,\mathrm{dB\,m^{-1}}$	Value for $\alpha = 1.5\,\mathrm{dB\,m^{-1}}$	Value for $\alpha = 2\,\mathrm{dB\,m^{-1}}$	Value for $\alpha = 2.5\,\mathrm{dB\,m^{-1}}$	Value for $\alpha = 3\,\mathrm{dB\,m^{-1}}$	Unit
Laser cavity length L_1	10.68	10.16	8.08	7.43	8	cm
Amplifier length L_2	1.224	1.203	1.194	1.186	1.165	m
Dopant concentration N_{Dy}	6×10^{25}	6×10^{25}	6×10^{25}	6×10^{25}	6×10^{25}	ions/m^3
FBG1 reflectivity R_1	99	99	99	99	99	%
FBG2 reflectivity R_2	70.85	52.33	71.39	67.41	52.75	%
Pump power $P_{\mathrm{p}}(0)$	3	3	3	3	3	W
Output power $P_{\mathrm{s}}(L)$	637.1	536.9	455.2	385.7	326.3	mW
Efficiency η	21.2	17.9	15.2	12.8	10.9	%

The parameters used in PSO algorithm, reported in Table 3.2, are the laser cavity length L_1, the amplifier length L_2, the dopant concentration N_{Dy} and the second mirror reflectivity R_2, while the first mirror reflectivity and the pump power are fixed to $R_1 = 99\,\%$ and $P_{\mathrm{p}}(0) = 3\,\mathrm{W}$ respectively. The output signal power $P_{\mathrm{s}}(L)$ is the fitness function which must be maximized by the ad-hoc implemented PSO algorithm. A number of simulations are performed in order to investigate the goodness of the MOPA even for optical losses larger than $\alpha = 1\,\mathrm{dB\,m^{-1}}$. In fact, soft glasses can exhibit higher losses. Propagation losses from $1\,\mathrm{dB\,m^{-1}}$ to $3\,\mathrm{dB\,m^{-1}}$ are considered in PSO optimizations. The PSO optimized parameters and the pertaining efficiencies η are reported in Table 3.3 for different fiber losses. The maximum output power, obtained with the PSO optimized MOPA, is $P_{\mathrm{s}}(L) = 637\,\mathrm{mW}$. Therefore, an efficiency close to $\eta = 21.2\,\%$ is reached. Fig. 3.10 illustrates PSO fitness function versus the iteration number I. It shows that $I = 25$ iterations are required to achieve a fitness function value very close to the optimum $P_{\mathrm{s}}(L) = 637\,\mathrm{mW}$ calculated for $I = 40$. The computation requires a time of about $T_c = 19\,\mathrm{h}$ by employing a quad-core Intel Xeon

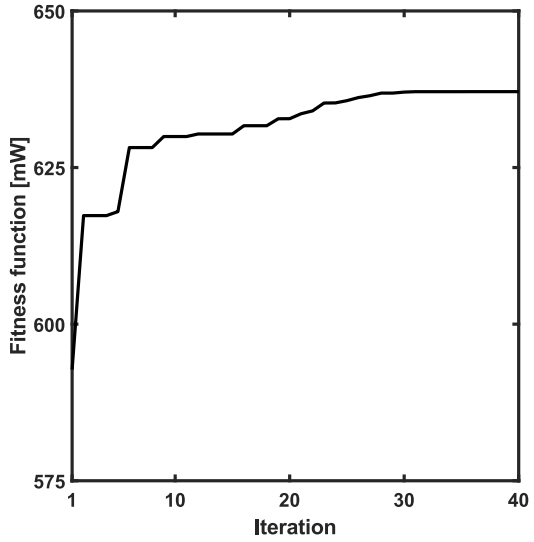

Figure 3.10: Global best fitness value versus iteration.

CPU.

The results of Table 3.3 also show that the output power decreases by increasing the optical losses. For the optical losses $\alpha = 3\,\mathrm{dB\,m^{-1}}$, it is almost halved with respect to the case $\alpha = 1\,\mathrm{dB\,m^{-1}}$, the efficiency in the worst case is about $\eta = 10.9\,\%$. This is particularly interesting since similar output powers are reported in literature, without the MOPA scheme, by considering higher dopant concentration $N_{\mathrm{Dy}} = 7 \times 10^{25}\,\mathrm{ions/m^3}$ and lower optical losses $\alpha = 1\,\mathrm{dB\,m^{-1}}$, therefore very close or beyond the technological limits [49].

Moreover, the spectrum of the laser signal close to $\lambda_{\mathrm{s}} = 4384\,\mathrm{nm}$ is calculated by considering the ASE effect. It is illustrated in Fig. 3.11. A signal-to-noise ratio (SNR) better than 40 dB is simulated. To reduce the effects of ASE noise amplification on the laser spectral purity, and thus improving the beam quality, a suitable filter after the first stage could be implemented by means of classical approaches [63, 64].

3.4 Conclusion

An efficient MOPA pumping scheme for a mid-IR laser based on dysprosium-doped chalcogenide glass is proposed. It is composed of a laser followed by an amplifier which

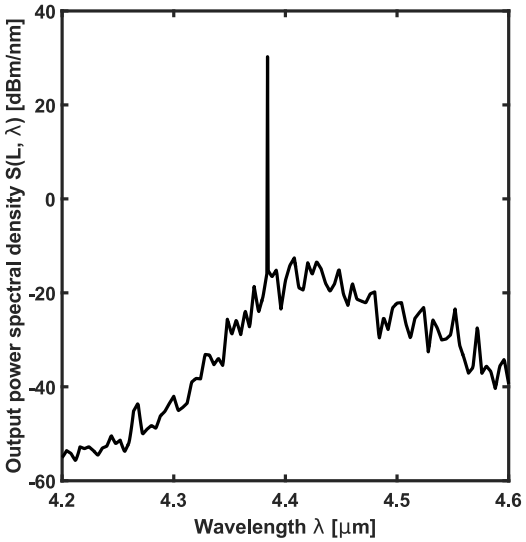

Figure 3.11: Output power spectral density $S(L, \lambda)$ of the PSO optimized Dy^{3+}-doped MOPA versus wavelength λ.

can be integrated in the same PCF or, as an alternative, suitably spliced. The proposed device is promising even for its fabrication easiness. The MOPA configuration allows to obtain sufficiently high signal power even when the population inversion is weak, provided that a suitable length for the amplifier stage is chosen. The simulations show that an output signal power of $P_s(L) = 637\,\mathrm{mW}$ at $\lambda_s = 4384\,\mathrm{nm}$ wavelength can be achieved with a pump power of $P_p(0) = 3\,\mathrm{W}$. Efficiencies larger than $\eta = 21\,\%$ can be obtained.

Chapter 4

Design and optimization of an innovative pumping scheme for a Dy^{3+}-doped chalcogenide PCF fiber laser

4.1 Introduction

This chapter reports the design of a novel pumping scheme for a mid-IR laser based on a photonic crystal fiber (PCF) made of dysprosium doped chalcogenide glass, Dy^{3+}:$Ga_5Ge_{20}Sb_{10}S_{65}$. In order to perform a realistic investigation, the simulation is performed by taking into account the spectroscopic parameters measured on the rare earth-doped glass sample. The simulated results show that an optical beam emission close to 4400 nm wavelength can be obtained by employing two pump beams at 2850 nm (pump #1) and 4092 nm (pump #2) wavelengths. The pump beams can be provided by commercial quantum cascade lasers (QCLs). As an example, for the pump powers 50 mW (pump #1) and 1 W (pump #2), input mirror reflectivity 99 %, output mirror reflectivity 30 %, optical cavity length 50 cm, a signal power close to 350 mW at the wavelength of 4384 nm can be generated.

The feasibility investigation is conducted numerically. A simulated pump efficiency of about 35 % is calculated. It is very high with respect to the literature results. The proposed PCF laser cavity can provide very high beam quality, typical of the single mode PCF guided light, in mid-IR wavelength range, by employing commercial QCL pump lasers with minor quality beam characteristics at slightly shorter wavelengths. The interest in this kind of source is motivated by the need of diffraction-limited mid-IR laser beams, necessary in a number of technological challenges as optical free propagation links, optical remote sensing, laser therapy and diagnostics.

The theoretical model is described in section 2.1.2.

4.2 Design of the double pumping scheme

The designed optical source employs a simple but optimized pumping scheme. Two optical pumps, with suitable wavelengths and powers, are injected within a single-mode photonic crystal fiber (PCF) by employing an optical combiner. An end pump combiner has two multi-mode pump input fiber legs and a single output fiber which is spliced to the Dy^{3+}:$Ga_5Ge_{20}Sb_{10}S_{65}$ fiber. The Dy^{3+}:$Ga_5Ge_{20}Sb_{10}S_{65}$ PCF laser is designed to obtain signal generation close to $\lambda_s = 4400\,\text{nm}$ wavelength. The optical cavity is obtained by using two suitable fiber Bragg gratings (FBG1, FBG2) inscribed in the core. The PCF cross-section is depicted in Fig. 4.1. It allows single mode propagation at both the pump and signal wavelengths. Three rings of air holes surround the rare earth-doped solid core. The geometrical parameters are the following: hole-to-hole spacing (or pitch) $\Lambda = 8\,\mu\text{m}$, hole diameter $d = 3.2\,\mu\text{m}$, doped region radius $R_d = 4\,\mu\text{m}$. The design is performed by considering the measured PCF parameters reported in [17, 60]. However, both the pumps could also be launched in a single core or in a double clad fiber. The measured refractive index wavelength dispersion of the $Ga_5Ge_{20}Sb_{10}S_{65}$ chalcogenide glass [17, 60] is taken into account by a Cauchy equation:

$$n(\lambda) = B + \frac{C}{\lambda^2} + \frac{D}{\lambda^4} \tag{4.1}$$

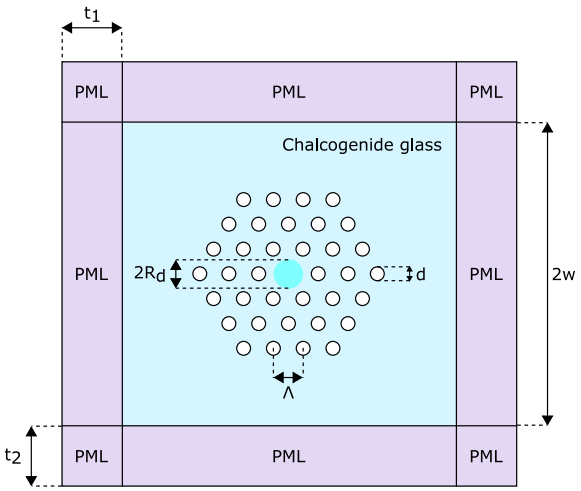

Figure 4.1: Cross-section of the photonic crystal fiber.

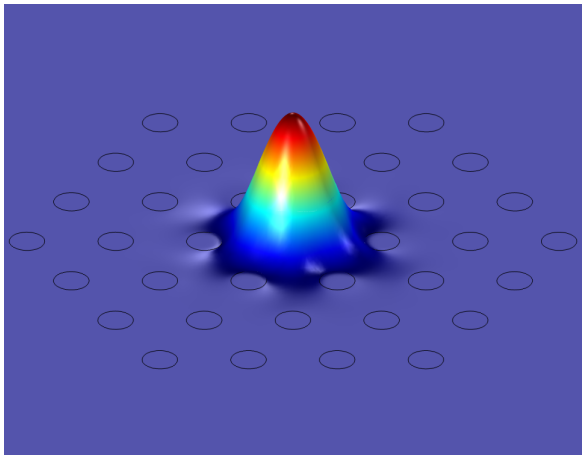

Figure 4.2: Distribution of the electric field norm for the fundamental mode at signal wavelength $\lambda_s = 4384\,\text{nm}$.

where $B = 2.2181$, $C = 0.0551$ and $D = -0.0003$. A full vectorial finite element method (FEM) commercial code (COMSOL Multiphysics, `http://www.comsol.com/`) is employed for the PCF electromagnetic investigation. Perfectly matched layers (PMLs) are used to avoid the numerical drawbacks due to the reflections into the computational domain of the outgoing waves. The computational domain is a square having width $w = 48\,\mu\text{m}$. The PML thickness is $t_{\text{PML}} = 12\,\mu\text{m}$. Fig. 4.2 illustrates the electric field norm distribution of the fundamental mode at the wavelength $\lambda_s = 4384\,\text{nm}$.

The emission cross-sections spectra at $3.0\,\mu\text{m}$ and $4.3\,\mu\text{m}$ were both estimated using the Futchbauer-Ladenburg relation from fluorescence measurements (Fig. 4.3). The $3.0\,\mu\text{m}$ absorption cross-section has been calculated from the absorption spec-

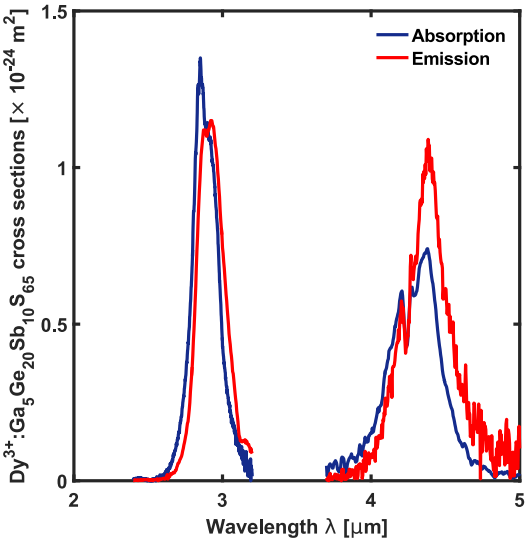

Figure 4.3: Calculated emission and absorption cross-sections for the Dy^{3+}:$Ga_5Ge_{20}Sb_{10}S_{65}$ glass.

Table 4.1: Calculated spectroscopic parameters of the Dy^{3+}-doped chalcogenide glass

Energy transition	Wavelength (nm)	Branching ratio	Lifetime (ms)
$^6H_{13/2} \rightarrow {}^6H_{15/2}$	2920	100 %	7.03
$^6H_{11/2} \rightarrow {}^6H_{13/2}$	4384	8.8 %	1.48
$^6H_{11/2} \rightarrow {}^6H_{15/2}$	1709	91.2 %	1.48

trum, while the 4.3 µm excited state absorption cross-section has been calculated from the emission cross-section using the reciprocity properties, also called the McCumber formula. These values are in agreement with other calculated parameters in selenide matrix [12, 49, 61]. Table 4.1 reports the calculated branching ratios and fluorescence lifetimes taking into account calculated multiphonon relaxation [5]. Propagation losses $\alpha(\nu) = 3\,\mathrm{dB\,m^{-1}}$ for all frequencies ν are supposed [12]. In the simulation, dopant concentrations lower than $N_{\mathrm{Dy}} = 6 \times 10^{25}\,\mathrm{ions/m^3}$ are considered in order to avoid the glass devitrification.

Fig. 4.4 illustrates the optical signal power P_{s} of the Dy^{3+}-doped fiber laser versus the optical cavity length L and dopant concentration N_{Dy}. The input pump #1 power is $P_{\mathrm{p1}}(0) = 50\,\mathrm{mW}$ at the wavelength $\lambda_{\mathrm{p1}} = 2850\,\mathrm{nm}$ and the input pump #2 power is $P_{\mathrm{p2}}(0) = 1000\,\mathrm{mW}$ at the wavelength $\lambda_{\mathrm{p2}} = 4092\,\mathrm{nm}$, the first mirror reflectivity is $R_1 = 99\,\%$, while the second mirror reflectivity is $R_2 = 30\,\%$. The reflectivities of

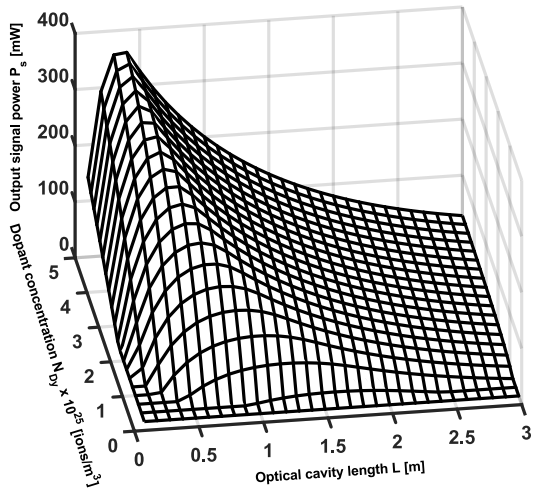

Figure 4.4: Optical signal power P_s of the Dy^{3+}-doped PCF laser versus optical cavity length L and dopant concentration N_Dy. Input pump #1 power $P_\mathrm{p1}(0) = 50\,\mathrm{mW}$ at the wavelength $\lambda_\mathrm{p1} = 2850\,\mathrm{nm}$; input pump #2 power $P_\mathrm{p2}(0) = 1000\,\mathrm{mW}$ at the wavelength $\lambda_\mathrm{p2} = 4092\,\mathrm{nm}$; first mirror reflectivity $R_1 = 99\,\%$; second mirror reflectivity $R_2 = 30\,\%$.

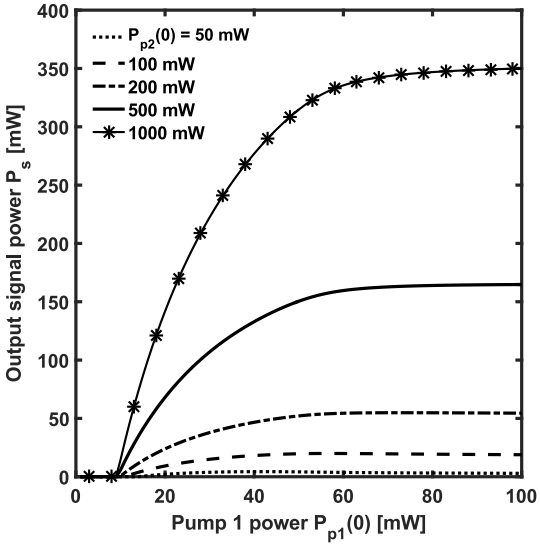

Figure 4.5: Optical signal power P_s of the Dy^{3+}-doped PCF laser, versus the input pump #1 power $P_\mathrm{p1}(0)$ at the wavelength $\lambda_\mathrm{p1} = 2850\,\mathrm{nm}$ for different input pump #2 powers at the wavelength $\lambda_\mathrm{p2} = 4092\,\mathrm{nm}$, $P_\mathrm{p2}(0) = 50\,\mathrm{mW}$ (dotted curve), $P_\mathrm{p2}(0) = 100\,\mathrm{mW}$ (dashed curve), $P_\mathrm{p2}(0) = 200\,\mathrm{mW}$ (dash-dot curve), $P_\mathrm{p2}(0) = 500\,\mathrm{mW}$ (solid curve), $P_\mathrm{p2}(0) = 1000\,\mathrm{mW}$ (solid curve with asterisk markers). Optical cavity length $L = 0.5\,\mathrm{m}$; dopant concentration $N_\mathrm{Dy} = 4 \times 10^{25}\,\mathrm{ions/m^3}$; first mirror reflectivity $R_1 = 99\,\%$; second mirror reflectivity $R_2 = 30\,\%$.

the mirrors at both λ_p1 and λ_p2 wavelengths are $R_1 = R_2 = 0\,\%$. A laser signal close to $P_\mathrm{s} = 360\,\mathrm{mW}$ can be obtained for the optical cavity length $L = 0.4\,\mathrm{m}$ and dopant

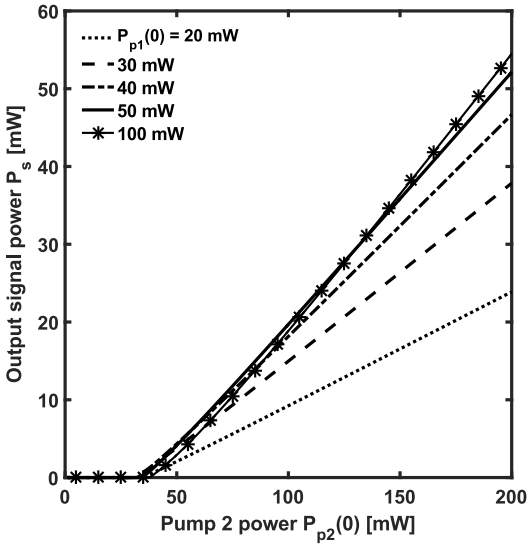

Figure 4.6: Optical signal power P_{s} of the Dy^{3+}-doped PCF laser, versus the input pump #2 power $P_{\mathrm{p2}}(0)$ at the wavelength $\lambda_{\mathrm{p2}} = 4092\,\mathrm{nm}$, for different input pump #1 powers at the wavelength $\lambda_{\mathrm{p1}} = 2850\,\mathrm{nm}$, $P_{\mathrm{p1}}(0) = 20\,\mathrm{mW}$ (dotted curve), $P_{\mathrm{p1}}(0) = 30\,\mathrm{mW}$ (dashed curve), $P_{\mathrm{p1}}(0) = 40\,\mathrm{mW}$ (dash-dot curve), $P_{\mathrm{p1}}(0) = 50\,\mathrm{mW}$ (solid curve), $P_{\mathrm{p1}}(0) = 100\,\mathrm{mW}$ (solid curve with asterisk markers). Optical cavity length $L = 0.5\,\mathrm{m}$; dopant concentration $N_{\mathrm{Dy}} = 4 \times 10^{25}\,\mathrm{ions/m^3}$; first mirror reflectivity $R_1 = 99\,\%$; second mirror reflectivity $R_2 = 30\,\%$.

concentration $N_{\mathrm{Dy}} = 5 \times 10^{25}\,\mathrm{ions/m^3}$. This result is particularly interesting since poor laser slope efficiencies (close to 10–15 %) are reported in literature for different pumping schemes [49].

Fig. 4.5 illustrates the optical signal power P_{s} of the Dy^{3+}-doped PCF laser, versus the input pump #1 power $P_{\mathrm{p1}}(0)$ for different input pump #2 powers, $P_{\mathrm{p2}}(0) = 50\,\mathrm{mW}$ (dotted curve), $P_{\mathrm{p2}}(0) = 100\,\mathrm{mW}$ (dashed curve), $P_{\mathrm{p2}}(0) = 200\,\mathrm{mW}$ (dash-dot curve), $P_{\mathrm{p2}}(0) = 500\,\mathrm{mW}$ (solid curve), $P_{\mathrm{p2}}(0) = 1000\,\mathrm{mW}$ (solid curve with asterisk markers). The optical cavity length is $L = 0.5\,\mathrm{m}$, the dopant concentration is $N_{\mathrm{Dy}} = 4 \times 10^{25}\,\mathrm{ions/m^3}$, the first mirror reflectivity is $R_1 = 99\,\%$ and the second mirror reflectivity is $R_2 = 30\,\%$. All the curves exhibit a slope which strongly decreases for input pump #1 power $P_{\mathrm{p1}}(0)$ higher than 50–60 mW. For the input pump #1 power $P_{\mathrm{p1}}(0) = 100\,\mathrm{mW}$, all the simulated signal powers are close to their saturation values (maximum values obtained by increasing $P_{\mathrm{p1}}(0)$).

Fig. 4.6 depicts the signal power P_{s} of the Dy^{3+}-doped PCF laser, versus the

input pump #2 power $P_{p2}(0)$, for different input pump #1 powers, $P_{p1}(0) = 20\,\text{mW}$ (dotted curve), $P_{p1}(0) = 30\,\text{mW}$ (dashed curve), $P_{p1}(0) = 40\,\text{mW}$ (dash-dot curve), $P_{p1}(0) = 50\,\text{mW}$ (solid curve), $P_{p1}(0) = 100\,\text{mW}$ (solid curve with asterisk markers). The other laser parameters are the same of Fig. 4.5. The laser characteristics are linear with respect to $P_{p2}(0)$. The slope efficiency increases by increasing the input pump #1 $P_{p1}(0)$ power. For input pump #1 power larger than $P_{p1}(0) = 50\,\text{mW}$ the slope efficiency slightly increases. A slope efficiency close to 36 % and a laser signal power close to $P_s = 54\,\text{mW}$ is obtained by employing the input pump powers $P_{p1}(0) = 100\,\text{mW}$ and $P_{p2}(0) = 200\,\text{mW}$ (solid curve with asterisk markers). The slope efficiency can be increased till about 38 % by considering an optimized cavity length close to $L = 40\,\text{cm}$, as it can be inferred from Fig. 4.4. The slope efficiency is calculated by considering only the pump 2 power $P_{p2}(0)$. However, it is almost coincident with the efficiency calculated by considering both P_{p1} and P_{p2} powers if $P_{p1}(0)$ is much lower than $P_{p2}(0)$ as in Fig. 4.4.

The simulations promise a feasible high beam quality laser in the mid-IR range. Possible drawbacks could be related to the construction of the multimode combiner which requires a good control of chalcogenide fiber fusion. Other crucial points are related to the optimization of the effective PCF losses and of the grating writing on chalcogenide fiber core.

4.3 Conclusion

An efficient and high beam quality laser source at the wavelength $\lambda_s = 4384\,\text{nm}$ is simulated. It is based on a novel double pumping configuration. A slope efficiency of about 33 % is calculated for the input pump #1 power $P_{p1} = 50\,\text{mW}$ at the wavelength $\lambda_{p1} = 2850\,\text{nm}$ and the input pump #2 power $P_{p2} = 1000\,\text{mW}$ at the wavelength $\lambda_{p2} = 4092\,\text{nm}$, with first mirror reflectivity $R_1 = 99\,\%$ and second mirror reflectivity $R_2 = 30\,\%$. The employment of commercial QCL pump lasers at slightly shorter wavelengths makes the system feasible and encourages the authors to construct the prototype. Since

possible drawbacks could be related to the construction of the multimode chalcogenide combiner, alternative coupling technique, based e.g. on lenses and objective, could be employed for the laser set-up implementation.

Chapter 5

Particle swarm optimization of a Dy^{3+}:ZBLAN fiber amplifier

5.1 Introduction

A Dy^{3+}-doped ZBLAN fiber amplifier based on an in-band pumped configuration is designed and optimized via an evolutionary approach. The complete amplifier model allows the definition of the fitness function to be optimized. Realistic values for optical and spectroscopic parameters are considered. For a fiber with dopant concentration of 2000 ppm, by employing an input pump power of 1 W at 2.72 µm wavelength, an optical gain of about 15.56 dB at 2.95 µm wavelength is obtained.

The theoretical model is described in section 2.2.1.

5.2 Results

The PSO algorithm is based on a stochastic technique inspired by the social behavior of a swarm of bees or a school of fish during their food-searching activities. Its main strengths are the simple implementation, the low number of tuning parameters and the ability to avoid local maxima. Moreover, it is derivative free and can be easily parallelized for multicore processing. It is particularly suitable for problems depending on

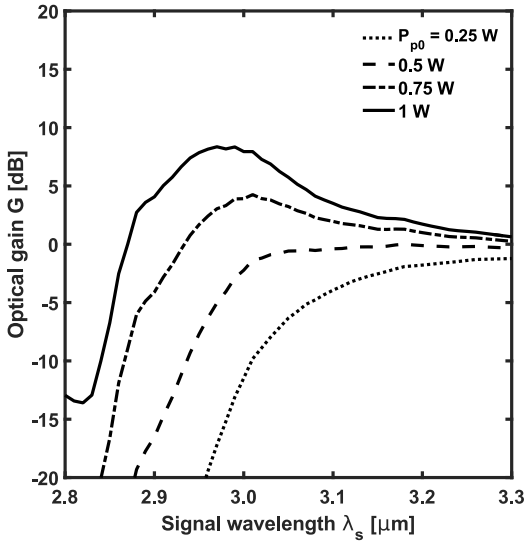

Figure 5.1: Optical gain G as a function of signal wavelength λ_s for different input pump powers, $P_{\mathrm{p}0} = 0.25\,\mathrm{W}$ (dotted curve), $P_{\mathrm{p}0} = 0.5\,\mathrm{W}$ (dashed curve), $P_{\mathrm{p}0} = 0.75\,\mathrm{W}$ (dash-dot curve), $P_{\mathrm{p}0} = 1\,\mathrm{W}$ (solid curve). Fiber length $L = 2\,\mathrm{m}$; dopant concentration $N_{\mathrm{Dy}} = 2000\,\mathrm{ppm}$; pump wavelength $\lambda_\mathrm{p} = 2.6\,\mu\mathrm{m}$; input signal power $P_{\mathrm{s}0} = 1\,\mu\mathrm{W}$.

several variables which must be varied simultaneously in order to maximize/minimize a certain fitness function. The fitness function to be maximized, for the case of the fiber amplifier, is the optical gain expressed in dB. Preliminary simulations are performed in order to investigate the possibility of obtaining a positive optical gain.

Fig. 5.1 shows the optical gain G as a function of signal wavelength λ_s for different input pump powers. A negative optical gain is obtained for input pump powers as high as 0.5 W regardless of the signal wavelength, which implies that $\lambda_\mathrm{p} = 2.6\,\mu\mathrm{m}$ is not a good choice for pumping this amplifier, i.e. the population inversion is too weak. Fig. 5.2 shows the optical gain G when the pump wavelength is increased to $\lambda_\mathrm{p} = 2.7\,\mu\mathrm{m}$. It can be seen that, with an input pump power of 0.5 W, a positive, although very small, optical gain is obtained. By increasing the pump power till 1 W, the maximum optical gain increases and the peak shifts towards shorter wavelengths, with a bandwidth of over 450 nm. Finally, the pump wavelength is increased to $\lambda_\mathrm{p} = 2.8\,\mu\mathrm{m}$ and the results are shown in Fig. 5.3. In this case, the performance is similar, but the optical gain begins to deteriorate, thus suggesting that the best pump wavelength lies between $2.7\,\mu\mathrm{m}$ and $2.8\,\mu\mathrm{m}$.

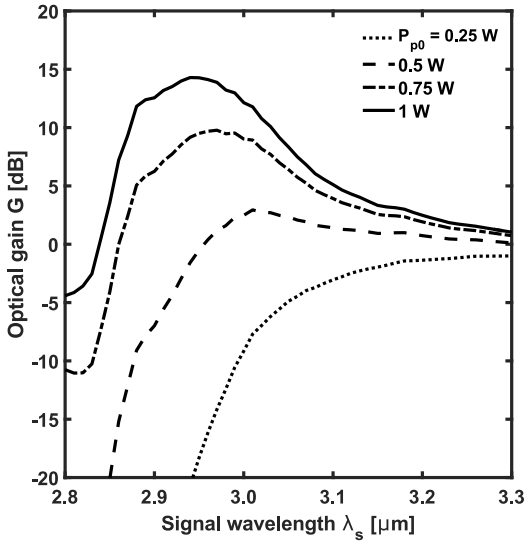

Figure 5.2: Optical gain G as a function of signal wavelength λ_s for different input pump powers, $P_\mathrm{p0} = 0.25\,\mathrm{W}$ (dotted curve), $P_\mathrm{p0} = 0.5\,\mathrm{W}$ (dashed curve), $P_\mathrm{p0} = 0.75\,\mathrm{W}$ (dash-dot curve), $P_\mathrm{p0} = 1\,\mathrm{W}$ (solid curve). Fiber length $L = 2\,\mathrm{m}$; dopant concentration $N_\mathrm{Dy} = 2000\,\mathrm{ppm}$; pump wavelength $\lambda_\mathrm{p} = 2.7\,\mu\mathrm{m}$; input signal power $P_\mathrm{s0} = 1\,\mu\mathrm{W}$.

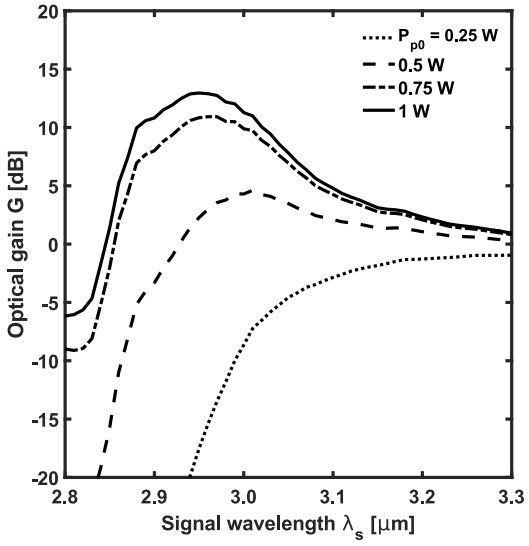

Figure 5.3: Optical gain G as a function of signal wavelength λ_s for different input pump powers, $P_\mathrm{p0} = 0.25\,\mathrm{W}$ (dotted curve), $P_\mathrm{p0} = 0.5\,\mathrm{W}$ (dashed curve), $P_\mathrm{p0} = 0.75\,\mathrm{W}$ (dash-dot curve), $P_\mathrm{p0} = 1\,\mathrm{W}$ (solid curve). Fiber length $L = 2\,\mathrm{m}$; dopant concentration $N_\mathrm{Dy} = 2000\,\mathrm{ppm}$; pump wavelength $\lambda_\mathrm{p} = 2.8\,\mu\mathrm{m}$; input signal power $P_\mathrm{s0} = 1\,\mu\mathrm{W}$.

Fig. 5.4 shows the noise figure NF as a function of signal wavelength λ_s for different input pump powers. The simulation parameters are the same of Fig. 5.1. It can be seen that noise figure exhibits a decreasing behavior with respect to the signal wavelength. The best achievable value of just above 3 dB can be obtained for signal wavelengths

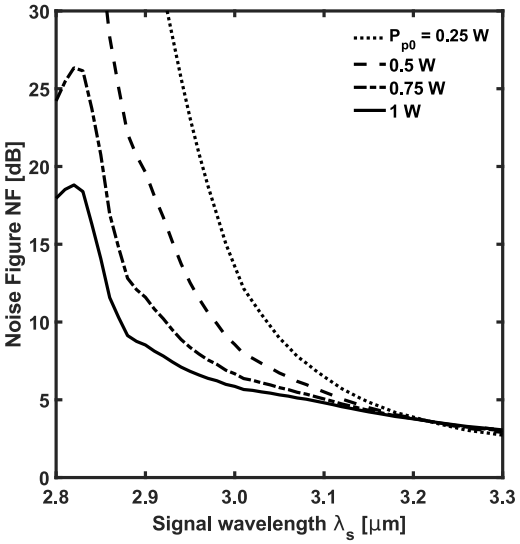

Figure 5.4: Noise Figure NF as a function of signal wavelength λ_s for different input pump powers, $P_\mathrm{p0} = 0.25\,\mathrm{W}$ (dotted curve), $P_\mathrm{p0} = 0.5\,\mathrm{W}$ (dashed curve), $P_\mathrm{p0} = 0.75\,\mathrm{W}$ (dash-dot curve), $P_\mathrm{p0} = 1\,\mathrm{W}$ (solid curve). Fiber length $L = 2\,\mathrm{m}$; dopant concentration $N_\mathrm{Dy} = 2000\,\mathrm{ppm}$; pump wavelength $\lambda_\mathrm{p} = 2.6\,\mu\mathrm{m}$; input signal power $P_\mathrm{s0} = 1\,\mu\mathrm{W}$.

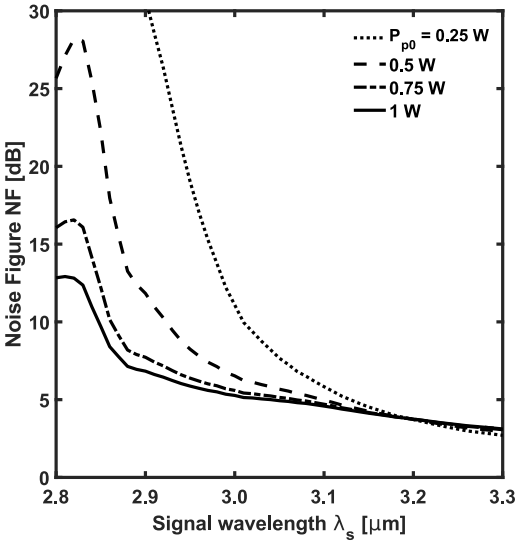

Figure 5.5: Noise Figure NF as a function of signal wavelength λ_s for different input pump powers, $P_\mathrm{p0} = 0.25\,\mathrm{W}$ (dotted curve), $P_\mathrm{p0} = 0.5\,\mathrm{W}$ (dashed curve), $P_\mathrm{p0} = 0.75\,\mathrm{W}$ (dash-dot curve), $P_\mathrm{p0} = 1\,\mathrm{W}$ (solid curve). Fiber length $L = 2\,\mathrm{m}$; dopant concentration $N_\mathrm{Dy} = 2000\,\mathrm{ppm}$; pump wavelength $\lambda_\mathrm{p} = 2.7\,\mu\mathrm{m}$; input signal power $P_\mathrm{s0} = 1\,\mu\mathrm{W}$.

longer than $\lambda_\mathrm{s} = 3.2\,\mu\mathrm{m}$, unfortunately where the optical gain is low or near zero. Conversely, around the wavelength $\lambda_\mathrm{s} = 2.95\,\mu\mathrm{m}$, where the optical gain is maximum, the noise figure increases to about 7 dB, which is still a rather good value. Fig. 5.5 shows the noise figure NF when the pump wavelength is increased to $\lambda_\mathrm{p} = 2.7\,\mu\mathrm{m}$. It

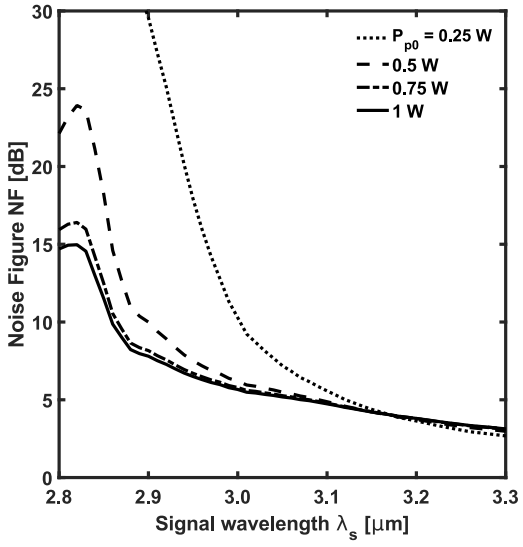

Figure 5.6: Noise Figure NF as a function of signal wavelength λ_s for different input pump powers, $P_\mathrm{p0} = 0.25\,\mathrm{W}$ (dotted curve), $P_\mathrm{p0} = 0.5\,\mathrm{W}$ (dashed curve), $P_\mathrm{p0} = 0.75\,\mathrm{W}$ (dash-dot curve), $P_\mathrm{p0} = 1\,\mathrm{W}$ (solid curve). Fiber length $L = 2\,\mathrm{m}$; dopant concentration $N_\mathrm{Dy} = 2000\,\mathrm{ppm}$; pump wavelength $\lambda_\mathrm{p} = 2.8\,\mu\mathrm{m}$; input signal power $P_\mathrm{s0} = 1\,\mu\mathrm{W}$.

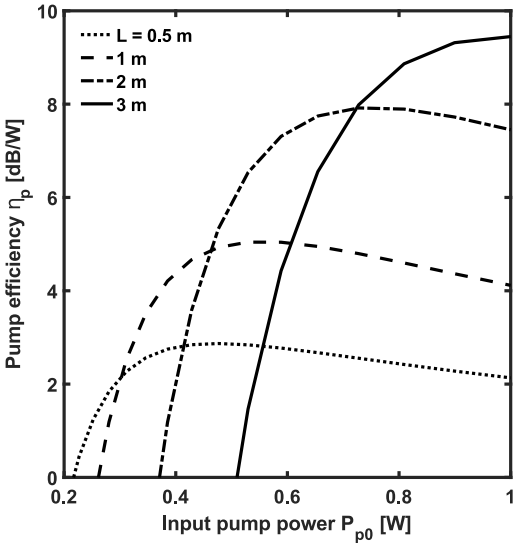

Figure 5.7: Pump efficiency η_p as a function of input pump power P_p0 for different fiber lengths, $L = 0.5\,\mathrm{m}$ (dotted curve), $L = 1\,\mathrm{m}$ (dashed curve), $L = 2\,\mathrm{m}$ (dash-dot curve), $L = 3\,\mathrm{m}$ (solid curve). Dopant concentration $N_\mathrm{Dy} = 1000\,\mathrm{ppm}$; pump wavelength $\lambda_\mathrm{p} = 2.7\,\mu\mathrm{m}$; signal wavelength $\lambda_\mathrm{s} = 2.94\,\mu\mathrm{m}$; input signal power $P_\mathrm{s0} = 1\,\mu\mathrm{W}$.

can be seen that the noise figure improves a bit for all the signal wavelengths, with the same decreasing behavior. The trend is confirmed in Fig. 5.6 where, for $\lambda_\mathrm{p} = 2.8\,\mu\mathrm{m}$, the noise figure curves for the input pump powers of $0.75\,\mathrm{W}$ and $1\,\mathrm{W}$ are almost coincident.

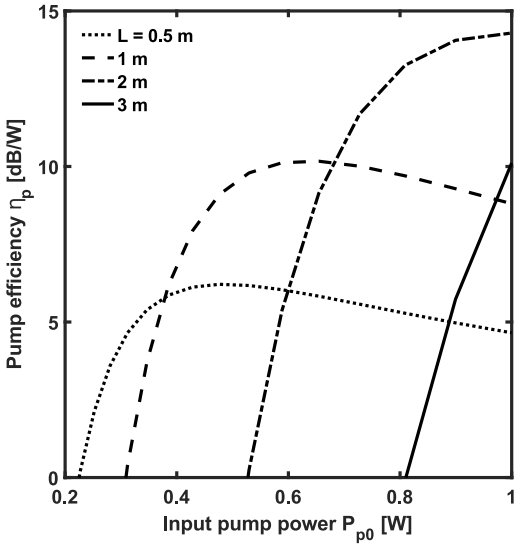

Figure 5.8: Pump efficiency η_{p} as a function of input pump power P_{p0} for different fiber lengths, $L = 0.5\,\mathrm{m}$ (dotted curve), $L = 1\,\mathrm{m}$ (dashed curve), $L = 2\,\mathrm{m}$ (dash-dot curve), $L = 3\,\mathrm{m}$ (solid curve). Dopant concentration $N_{\mathrm{Dy}} = 2000\,\mathrm{ppm}$; pump wavelength $\lambda_{\mathrm{p}} = 2.7\,\mu\mathrm{m}$; signal wavelength $\lambda_{\mathrm{s}} = 2.94\,\mu\mathrm{m}$; input signal power $P_{\mathrm{s0}} = 1\,\mu\mathrm{W}$.

An important parameter for the design of fiber amplifiers is the pump efficiency $\eta_{\mathrm{p}} = \frac{G}{P_{\mathrm{p0}}}$, which allows the identification of the operating conditions in which it is possible to obtain the best optical gain with the least amount of pump power. Fig. 5.7 shows the pump efficiency η_{p} as a function of input pump power P_{p0} for different fiber lengths and for a low dopant concentration $N_{\mathrm{Dy}} = 1000\,\mathrm{ppm}$. The curves exhibit an increasing behavior for low input pump powers and a decreasing behavior for high input pump powers. Moreover, the pump efficiency is higher for longer fibers. The best achievable value is $\eta_{\mathrm{p}} = 9.3\,\mathrm{dB\,W^{-1}}$. The behavior of pump efficiency is investigated also for a higher dopant concentration $N_{\mathrm{Dy}} = 2000\,\mathrm{ppm}$ and the results are illustrated in Fig. 5.8. In this case, the pump efficiency is greatly improved and can exceed $14\,\mathrm{dB\,W^{-1}}$ for a fiber length of $L = 2\,\mathrm{m}$. However, higher input pump powers with respect to the case of low dopant concentration are required.

Fig. 5.9 shows the optical gain G as a function of input signal power P_{s0} for different input pump powers and for a short fiber with $L = 1\,\mathrm{m}$. The optical gain increases by increasing the input pump power, with a maximum close to $9\,\mathrm{dB}$ for $P_{\mathrm{p0}} = 1\,\mathrm{W}$. For input signal powers lower than $0\,\mathrm{dBm}$, no saturation is observed regardless of the

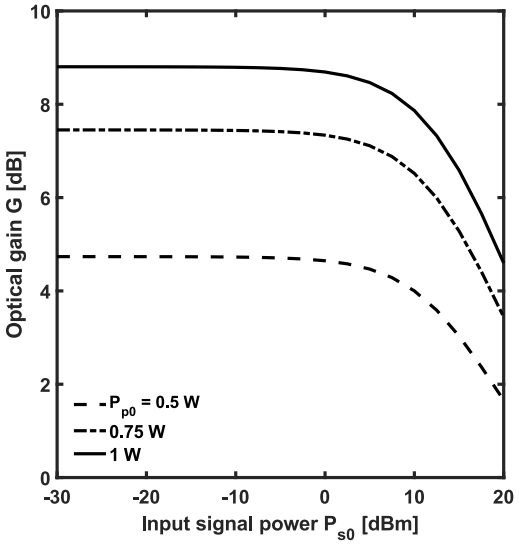

Figure 5.9: Optical gain G as a function of input signal power P_{s0} for different input pump powers, $P_{\mathrm{p0}} = 0.5\,\mathrm{W}$ (dashed curve), $P_{\mathrm{p0}} = 0.75\,\mathrm{W}$ (dash-dot curve), $P_{\mathrm{p0}} = 1\,\mathrm{W}$ (solid curve). Fiber length $L = 1\,\mathrm{m}$; dopant concentration $N_{\mathrm{Dy}} = 2000\,\mathrm{ppm}$; pump wavelength $\lambda_{\mathrm{p}} = 2.7\,\mu\mathrm{m}$; signal wavelength $\lambda_{\mathrm{s}} = 2.94\,\mu\mathrm{m}$.

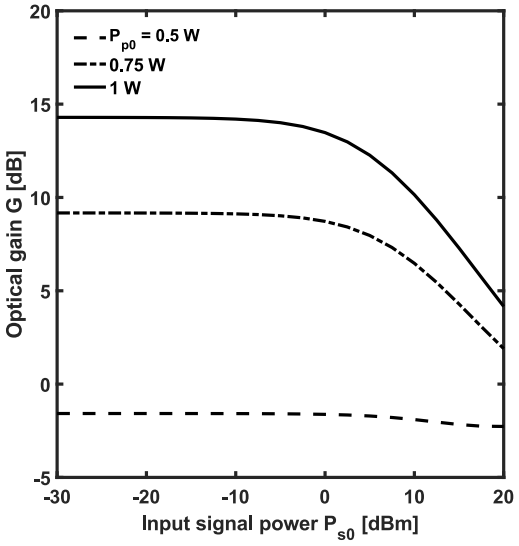

Figure 5.10: Optical gain G as a function of input signal power P_{s0} for different input pump powers, $P_{\mathrm{p0}} = 0.5\,\mathrm{W}$ (dashed curve), $P_{\mathrm{p0}} = 0.75\,\mathrm{W}$ (dash-dot curve), $P_{\mathrm{p0}} = 1\,\mathrm{W}$ (solid curve). Fiber length $L = 2\,\mathrm{m}$; dopant concentration $N_{\mathrm{Dy}} = 2000\,\mathrm{ppm}$; pump wavelength $\lambda_{\mathrm{p}} = 2.7\,\mu\mathrm{m}$; signal wavelength $\lambda_{\mathrm{s}} = 2.94\,\mu\mathrm{m}$.

pump power value. However, when the input signal power is increased towards 10 dBm, saturation occurs and the optical gain begins to deteriorate. Gain saturation curves are also calculated for a long fiber with $L = 2\,\mathrm{m}$. The results are illustrated in Fig. 5.10. The behavior is similar, with a maximum optical gain which can exceed 14 dB for

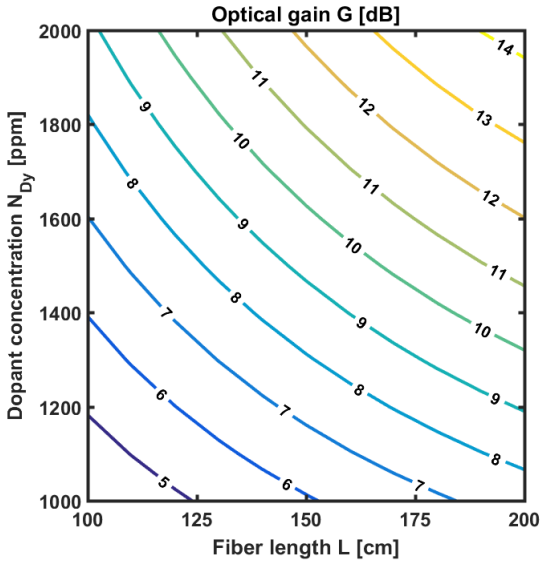

Figure 5.11: Optical gain G as a function of fiber length L and dopant concentration N_{Dy}. Pump wavelength $\lambda_{\mathrm{p}} = 2.7\,\mu\mathrm{m}$; signal wavelength $\lambda_{\mathrm{s}} = 2.94\,\mu\mathrm{m}$; input pump power $P_{\mathrm{p0}} = 1\,\mathrm{W}$; input signal power $P_{\mathrm{s0}} = 1\,\mu\mathrm{W}$.

$P_{\mathrm{p0}} = 1\,\mathrm{W}$. However, saturation occurs for a lower input signal power (0 dBm).

Fig. 5.11 illustrates the optical gain G of the Dy^{3+}-doped ZBLAN fiber amplifier as a function of fiber length L and dopant concentration N_{Dy}. The input pump power is $P_{\mathrm{p0}} = 1\,\mathrm{W}$, the input signal power is $P_{\mathrm{s0}} = 1\,\mu\mathrm{W}$, the pump wavelength is $\lambda_{\mathrm{p}} = 2.7\,\mu\mathrm{m}$ and the signal wavelength is $\lambda_{\mathrm{s}} = 2.94\,\mu\mathrm{m}$. The maximum achievable optical gain is about 14 dB. Moreover, long fibers with lower dopant concentrations provide performance similar to that of short fibers with higher dopant concentrations. Fig. 5.12 illustrates the noise figure NF of the Dy^{3+}-doped ZBLAN fiber amplifier as a function of fiber length L and dopant concentration N_{Dy}, for the same parameters of Fig. 5.11. The calculated noise figure values are between 5 and 6 dB, with longer fibers exhibiting a worse performance. Therefore, a proper trade-off between optical gain and noise figure is necessary.

The obtained results indicate the possibility to optimize the amplifier characteristics by a slight tuning of the operating condition and the design parameters. To this aim, the PSO is applied, by searching the global optimum in a three-dimensional solution space, via the simultaneous variation of the fiber length L, the pump wavelength

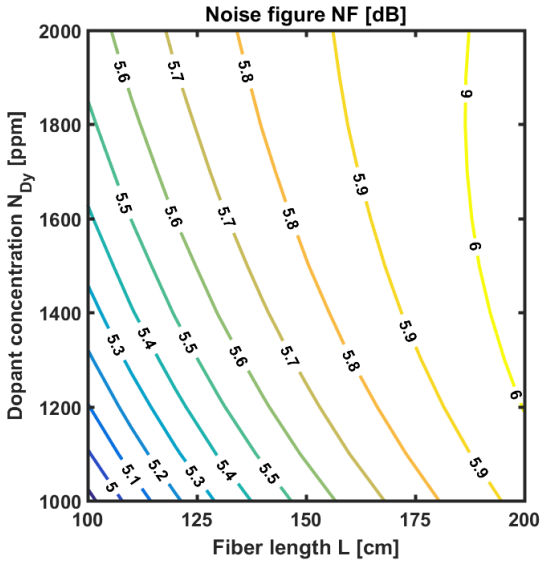

Figure 5.12: Noise Figure NF as a function of fiber length L and dopant concentration N_{Dy}. Pump wavelength $\lambda_{\mathrm{p}} = 2.7\,\mu\mathrm{m}$; signal wavelength $\lambda_{\mathrm{s}} = 2.94\,\mu\mathrm{m}$; input pump power $P_{\mathrm{p0}} = 1\,\mathrm{W}$; input signal power $P_{\mathrm{s0}} = 1\,\mu\mathrm{W}$.

Table 5.1: Parameters employed in the particle swarm optimization

Parameter	Value	Unit
Solution space dimension	3	
Number of particles	30	
Fiber length L	0.1–3.0	m
Pump wavelength λ_{p}	2.5–2.8	µm
Signal wavelength λ_{s}	2.8–3.2	µm
Dopant concentration N_{Dy}	2000	ppm
Input pump power P_{p0}	1	W
Input signal power P_{s0}	1	µW

λ_{p} and the signal wavelength λ_{s}. The dopant concentration N_{Dy}, the input pump power P_{p0} and the input signal power P_{s0} are fixed to 2000 ppm, 1 W and 1 µW, respectively, as summarized in Table 5.1. It is worthwhile noting that the signal wavelength must be greater than the pump wavelength, i.e. $\lambda_{\mathrm{s}} > \lambda_{\mathrm{p}}$, in order to obtain a positive optical gain. Fig. 5.13 shows the fitness function value as a function of iteration number. About 15 iterations are enough to achieve convergence, thus confirming the effectiveness of the PSO algorithm. The values of the input parameters which maximize the optical gain are the following: $L = 2.34\,\mathrm{m}$, $\lambda_{\mathrm{p}} = 2.72\,\mu\mathrm{m}$ and $\lambda_{\mathrm{s}} = 2.95\,\mu\mathrm{m}$. The PSO optimized amplifier yields a maximum optical gain of 15.56 dB and a noise figure of

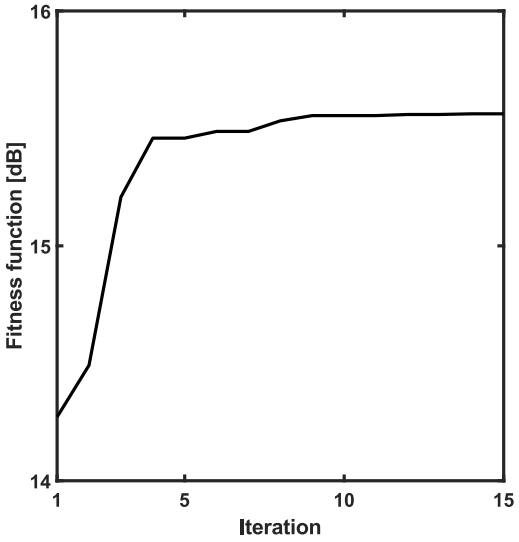

Figure 5.13: Fitness function value as a function of iteration number.

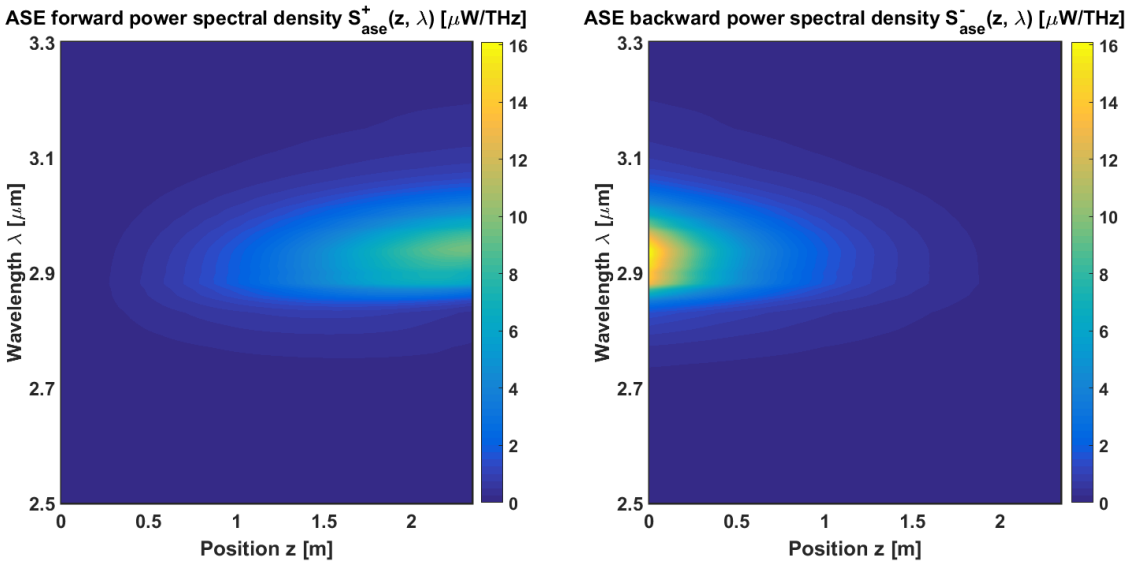

(a) (b)

Figure 5.14: Power spectral density of (a) forward and (b) backward ASE noise as a function of position and wavelength.

5.86 dB. The power spectral density of both forward and backward ASE noise as a function of position z and wavelength λ is shown in Fig. 5.14(a) and 5.14(b). It is apparent that ASE noise is stronger at the beginning of the fiber, where the pump power is maximum, whereas it is weaker at the end of the fiber, where the pump is almost depleted.

5.3 Conclusion

In this chapter, the particle swarm optimization algorithm was applied in order to maximize the optical gain of an in-band pumped Dy^{3+}-doped ZBLAN fiber amplifier. For a fiber with dopant concentration of 2000 ppm and length of 2.34 m, by employing an input pump power of 1 W at 2.72 µm, a maximum optical gain of 15.56 dB at 2.95 µm can be achieved, with a noise figure as low as 5.86 dB.

Chapter 6

Design of a continuous-wave Dy^{3+}:ZBLAN fiber laser

6.1 Introduction

In this chapter, a continuous-wave middle-infrared solid-state laser, based on a ZBLAN fiber doped with trivalent dysprosium ions, emitting at the wavelength $\lambda = 3\,\mu m$ is designed. Single mode laser emission is obtained through in-band pumping at $\lambda = 2.8\,\mu m$. In order to accurately investigate the feasibility and the performance of the device, realistic parameters for the fiber and the rare earth are considered. In particular, the emission and absorption cross sections, the lifetimes, the refractive index wavelength dispersion and the power propagation are accurately modeled. The model is exploited to predict the laser performance in terms of slope efficiency and power threshold. A maximum slope efficiency of about $\eta_s = 54\,\%$ and a threshold power P_{th} in the 150–250 mW range are predicted.

The theoretical model is described in section 2.2.2.

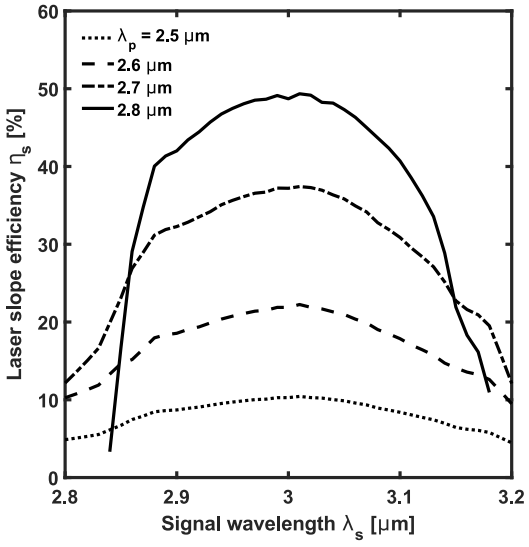

Figure 6.1: Slope efficiency η_s of the Dy^{3+}-doped ZBLAN fiber laser versus the signal wavelength λ_s for four different pump wavelengths, $\lambda_p = 2.5\,\mu m$ (dotted curve), $\lambda_p = 2.6\,\mu m$ (dashed curve), $\lambda_p = 2.7\,\mu m$ (dash-dot curve), $\lambda_p = 2.8\,\mu m$ (solid curve). Fiber length $L = 1\,m$; dopant concentration $N_{Dy} = 2000\,ppm$; first mirror reflectivity $R_1 = 99\,\%$; second mirror reflectivity $R_2 = 50\,\%$.

6.2 Numerical results

In order to accurately simulate the performance of the laser, realistic values for all the physical parameters are considered. In particular, the fiber parameters are the following: refractive index $n = 1.48$ at $\lambda = 2.88\,\mu m$, attenuation $\alpha = 0.9\,dB\,m^{-1}$, core diameter $d_c = 12\,\mu m$, numerical aperture $NA = 0.16$. Fig. 6.1 shows the laser slope efficiency, i.e. the slope η_s of the laser input-output characteristic, as a function of the signal wavelength λ_s for four different pump wavelengths. The maximum slope efficiency $\eta_s = 49\,\%$ is obtained for a signal wavelength $\lambda_s = 3\,\mu m$ by employing a pump wavelength $\lambda_p = 2.8\,\mu m$. A wide tuning range of about 290 nm is predicted. Fig. 6.2 shows the power threshold P_{th} of the laser as a function of the signal wavelength λ_s for the same parameters of Fig. 6.1. The minimum threshold $P_{th} = 233\,mW$ is obtained for the same wavelengths of the previous case. Hence, hereafter the pump and signal wavelengths are fixed to $\lambda_p = 2.8\,\mu m$ and $\lambda_s = 3\,\mu m$, respectively.

In Fig. 6.3, the laser slope efficiency η_s versus the fiber length L is shown for four different dopant concentrations. In the case of low doping $N_{Dy} = 500\,ppm$, the

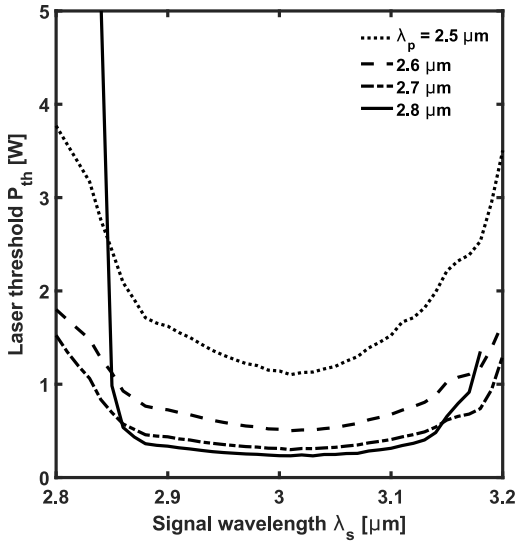

Figure 6.2: Threshold P_{th} of the Dy^{3+}-doped ZBLAN fiber laser versus the signal wavelength λ_{s} for four different pump wavelengths, $\lambda_{\mathrm{p}} = 2.5\,\mu\mathrm{m}$ (dotted curve), $\lambda_{\mathrm{p}} = 2.6\,\mu\mathrm{m}$ (dashed curve), $\lambda_{\mathrm{p}} = 2.7\,\mu\mathrm{m}$ (dash-dot curve), $\lambda_{\mathrm{p}} = 2.8\,\mu\mathrm{m}$ (solid curve). Fiber length $L = 1\,\mathrm{m}$; dopant concentration $N_{\mathrm{Dy}} = 2000\,\mathrm{ppm}$; first mirror reflectivity $R_1 = 99\,\%$; second mirror reflectivity $R_2 = 50\,\%$.

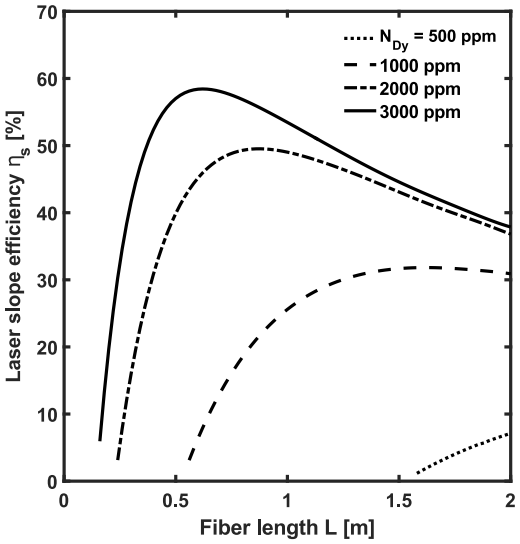

Figure 6.3: Slope efficiency η_{s} of the Dy^{3+}-doped ZBLAN fiber laser versus the fiber length L for four different dopant concentrations, $N_{\mathrm{Dy}} = 500\,\mathrm{ppm}$ (dotted curve), $N_{\mathrm{Dy}} = 1000\,\mathrm{ppm}$ (dashed curve), $N_{\mathrm{Dy}} = 2000\,\mathrm{ppm}$ (dash-dot curve), $N_{\mathrm{Dy}} = 3000\,\mathrm{ppm}$ (solid curve). Pump wavelength $\lambda_{\mathrm{p}} = 2.8\,\mu\mathrm{m}$; signal wavelength $\lambda_{\mathrm{s}} = 3.0\,\mu\mathrm{m}$; first mirror reflectivity $R_1 = 99\,\%$; second mirror reflectivity $R_2 = 50\,\%$.

maximum slope efficiency $\eta_{\mathrm{s}} = 7\,\%$ is obtained for a fiber length longer than $L = 2\,\mathrm{m}$. To increase the efficiency, a higher dopant concentration $N_{\mathrm{Dy}} = 3000\,\mathrm{ppm}$ is required.

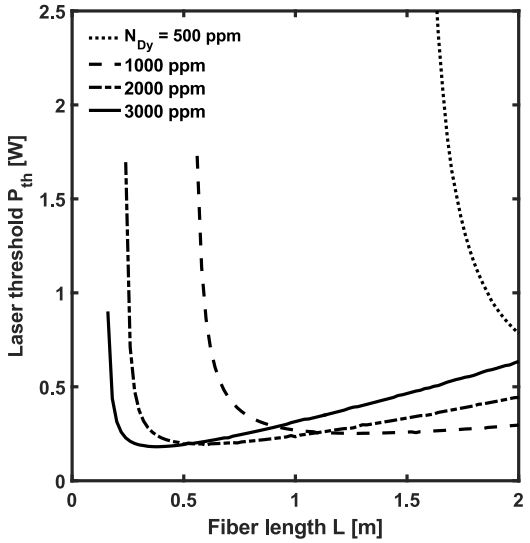

Figure 6.4: Threshold P_{th} of the Dy^{3+}-doped ZBLAN fiber laser versus the fiber length L for four different dopant concentrations, $N_{\mathrm{Dy}} = 500\,\mathrm{ppm}$ (dotted curve), $N_{\mathrm{Dy}} = 1000\,\mathrm{ppm}$ (dashed curve), $N_{\mathrm{Dy}} = 2000\,\mathrm{ppm}$ (dash-dot curve), $N_{\mathrm{Dy}} = 3000\,\mathrm{ppm}$ (solid curve). Pump wavelength $\lambda_{\mathrm{p}} = 2.8\,\mu\mathrm{m}$; signal wavelength $\lambda_{\mathrm{s}} = 3.0\,\mu\mathrm{m}$; first mirror reflectivity $R_1 = 99\,\%$; second mirror reflectivity $R_2 = 50\,\%$.

In this case, the maximum slope efficiency reached $\eta_{\mathrm{s}} = 58\,\%$ for a shorter fiber length $L = 60\,\mathrm{cm}$. Fig. 6.4 shows the power threshold P_{th} of the laser as a function of the fiber length L for the same parameters of Fig. 6.3. In the case of low doping, the minimum threshold $P_{\mathrm{th}} = 784\,\mathrm{mW}$ can be achieved for almost the same configuration of the previous case. Conversely, in the case of high doping, a different fiber length $L = 38\,\mathrm{cm}$ is required in order to obtain the lowest threshold $P_{\mathrm{th}} = 181\,\mathrm{mW}$.

In Fig. 6.5, the laser slope efficiency η_{s} versus the output mirror reflectivity R_2 is shown for four different dopant concentrations. In every case, the function has a maximum for an intermediate value of the mirror reflectivity R_2. The maximum achievable slope efficiencies are $\eta_{\mathrm{s}} = 6.33\,\%$ for the reflectivity $R_2 = 82\,\%$ and dopant concentration $N_{\mathrm{Dy}} = 500\,\mathrm{ppm}$ (i.e. low doping) and $\eta_{\mathrm{s}} = 66.2\,\%$ for $R_2 = 12\,\%$ and dopant concentration $N_{\mathrm{Dy}} = 3000\,\mathrm{ppm}$ (i.e. high doping). Fig. 6.6 shows the power threshold P_{th} of the laser as a function of the output mirror reflectivity R_2 for the same parameters of Fig. 6.5. In every case, the function is monotonically decreasing, which implies that the highest slope efficiency and the lowest threshold cannot be obtained simulta-

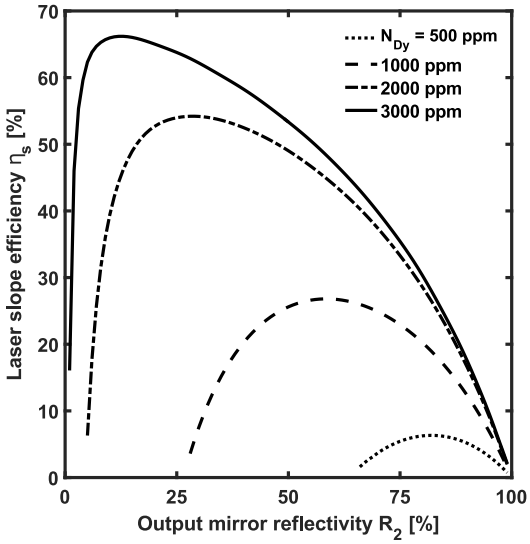

Figure 6.5: Slope efficiency η_s of the Dy^{3+}-doped ZBLAN fiber laser versus the second mirror reflectivity R_2 for four different dopant concentrations, $N_\mathrm{Dy} = 500\,\mathrm{ppm}$ (dotted curve), $N_\mathrm{Dy} = 1000\,\mathrm{ppm}$ (dashed curve), $N_\mathrm{Dy} = 2000\,\mathrm{ppm}$ (dash-dot curve), $N_\mathrm{Dy} = 3000\,\mathrm{ppm}$ (solid curve). Pump wavelength $\lambda_\mathrm{p} = 2.8\,\mu\mathrm{m}$; signal wavelength $\lambda_\mathrm{s} = 3.0\,\mu\mathrm{m}$; fiber length $L = 1\,\mathrm{m}$; first mirror reflectivity $R_1 = 99\,\%$.

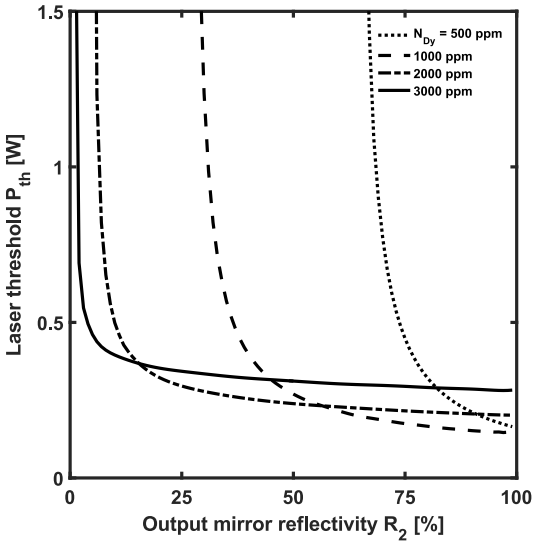

Figure 6.6: Threshold P_th of the Dy^{3+}-doped ZBLAN fiber laser versus the second mirror reflectivity R_2 for four different dopant concentrations, $N_\mathrm{Dy} = 500\,\mathrm{ppm}$ (dotted curve), $N_\mathrm{Dy} = 1000\,\mathrm{ppm}$ (dashed curve), $N_\mathrm{Dy} = 2000\,\mathrm{ppm}$ (dash-dot curve), $N_\mathrm{Dy} = 3000\,\mathrm{ppm}$ (solid curve). Pump wavelength $\lambda_\mathrm{p} = 2.8\,\mu\mathrm{m}$; signal wavelength $\lambda_\mathrm{s} = 3.0\,\mu\mathrm{m}$; fiber length $L = 1\,\mathrm{m}$; first mirror reflectivity $R_1 = 99\,\%$.

neously. The best laser threshold $P_\mathrm{th} = 146\,\mathrm{mW}$ is reached with a mirror reflectivity higher than $R_2 = 99\,\%$ for the case of dopant concentration $N_\mathrm{Dy} = 1000\,\mathrm{ppm}$.

Table 6.1: Parameters for the PSO optimized laser with maximum slope efficiency

Parameter	Value
Fiber length L	1.45 m
Dopant concentration N_{Dy}	2000 ppm
Input mirror reflectivity R_1	99 %
Output mirror reflectivity R_2	12.7 %
Pump wavelength λ_{p}	2.8 µm
Signal wavelength λ_{s}	2.967 µm
Slope efficiency η_{s}	57.76 %
Threshold P_{th}	410 mW

In order to find the configuration providing the maximum possible slope efficiency, a particle swarm optimization (PSO) algorithm [1, 14] is exploited. The PSO input parameters are the fiber length L, the output mirror reflectivity R_2, the pump wavelength λ_{p} and the signal wavelength λ_{s}, while the dopant concentration N_{Dy} and the input mirror reflectivity R_1 are fixed. The laser slope efficiency η_{s} is chosen as the fitness function. The results are reported in Table 6.1. As it can be easily seen, by adopting the PSO algorithm, the slope efficiency of the Dy^{3+}:ZBLAN fiber laser can be increased till $\eta_{\mathrm{s}} = 57.76\,\%$, although a rather high power threshold $P_{\mathrm{th}} = 410\,\mathrm{mW}$ is required. This slope efficiency is comparable to that obtained for the considerably higher dopant concentration $N_{\mathrm{Dy}} = 3000\,\mathrm{ppm}$.

6.3 Preliminary experimental results

In this section, some details on the experimental laser set-up implemented at the laboratory of the Polytechnic of Milan, IFN research group of Prof. Gianluca Galzerano, in collaboration with Polytechnic of Bari, MOE research group of Prof. Francesco Prudenzano, are reported. The developed experimental set-up is preliminary and constitutes a first step towards the actual optimization of the optical sources proposed in this thesis. Fig. 6.7 illustrates the set-up constituted by a dysprosium-doped ZBLAN fiber of 0.6 m m length, a CaF_2 lens, a Brewster plate, a high reflecting plane mirror and an output coupler. It is worthwhile noting that it is a non-optimized set-up. In

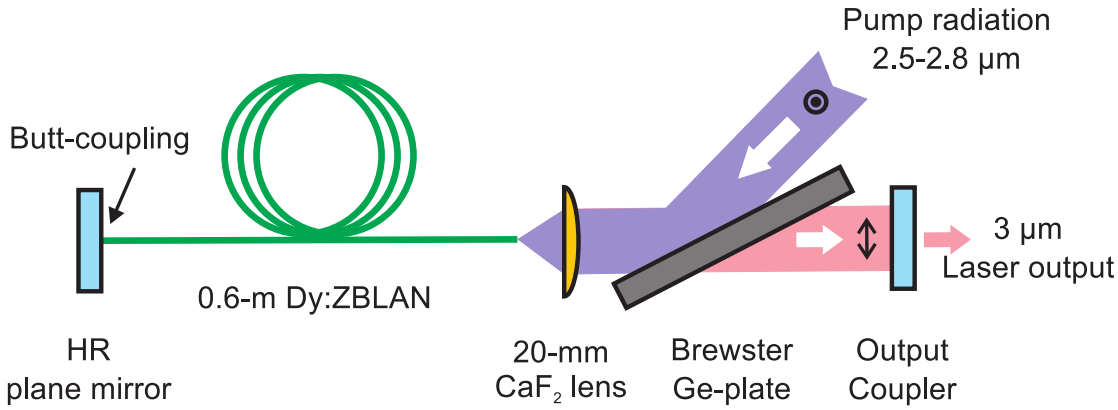

Figure 6.7: Experimental set-up for the CW Dy^{3+}-doped ZBLAN fiber laser.

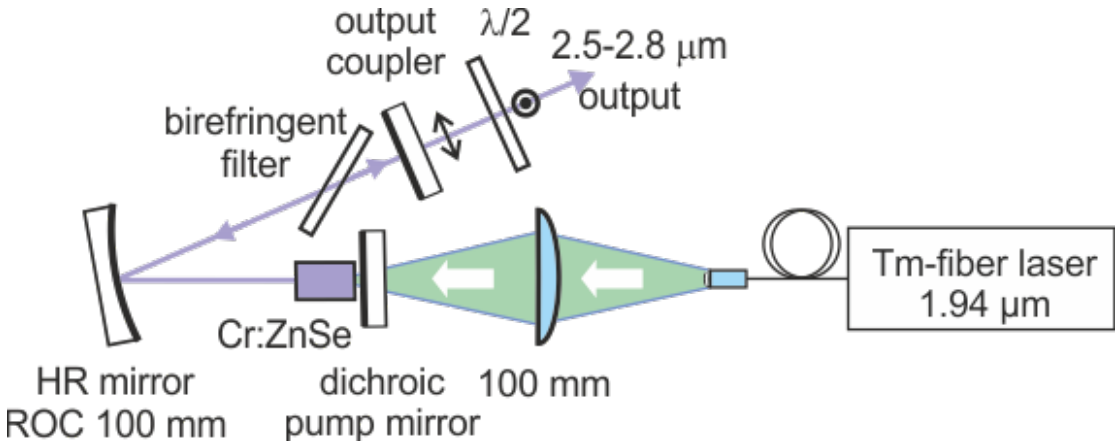

Figure 6.8: Cr:ZnSe pump laser setup.

fact, at this stage, the pump coupling is not yet refined.

Fig. 6.8 shows the folded linear resonator setup of the tunable Cr:ZnSe laser consisting in a dichroic plane mirror (reflectance $R > 99.5\,\%$ from 2350 to 3050 nm and transmittance $T > 95\,\%$ at 1940 nm), a plano-concave folding mirror ($R > 99.5\,\%$ from 2100 to 3000 nm) with a radius of curvature of 100 mm, and a plane output coupler with 70 % reflectivity at 2.9 µm. In the longest resonator arm (170 mm) a 2 mm thick quartz plate is inserted at the Brewster angle as an intracavity tunable birefringent filter. The 6 mm thick AR-coated Cr:ZnSe crystal, mounted on a copper heat sink kept at a constant temperature of 18 °C by a Peltier electric-cooler, is inserted in the shortest resonator arm adjacent to the dichroic plane mirror. The Cr:ZnSe crystal is pumped by a CW Tm:fiber laser (IPG Photonics, model TLR-LP-20) with a maximum output power of 20 W at 1.94 µm through the dichroic pump mirror using an

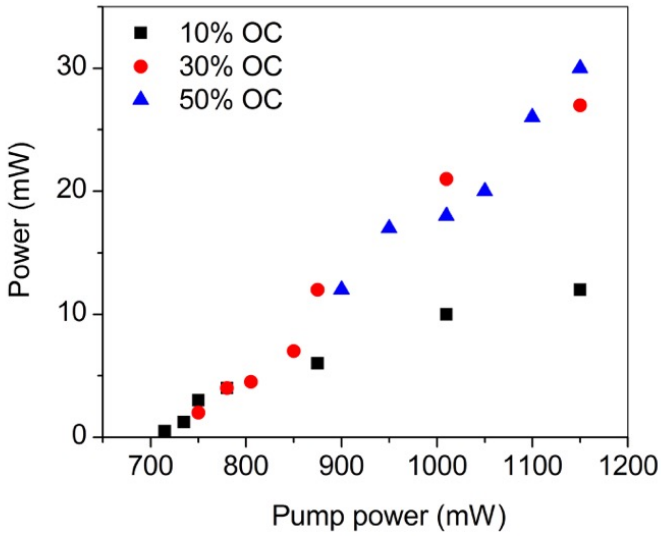

Figure 6.9: Measured input-output characteristics of the CW Dy^{3+}-doped ZBLAN fiber laser.

AR-coated plano-convex lens with a focal length of 100 mm.

A pump coupling efficiency of 50 % is obtained by employing the Ge-plate reflection ($R = 78\,\%$ for TE polarization state), the CaF_2 plano-convex lens transmission ($T = 96\,\%$ at the different pump wavelengths), and the mode-beam matching. The characteristics of the Dy^{3+}:ZBLAN laser were measured in terms of output power versus launched pump power for different output coupler (OC) transmission values of 10 %, 30 %, and 50 % and at different pump wavelengths and are shown in Fig. 6.9. The best result in terms of output power and slope efficiency was obtained for the highest available 50 % output coupling, with a maximum slope efficiency of about 7 %, with respect to the launched pump power (corresponding to about 14 % efficiency with respect to the absorbed pump power). Lower efficiencies and output powers were achieved with the lower output couplings.

It is worthwhile noting that these results are obtained for a set-up with input and output mirrors, fiber length, pump wavelength and pump coupling roughly chosen and different with respect to those identified in the design reported in the previous section.

The components employed in the set-up were available in the lab and therefore not the optimal ones. In fact, in a similar experiment reported in [65], a higher overall

efficiency was found. Anyway, further efforts will be devoted to the development of more performing optical sources, both CW and pulsed, by employing the proper components. In addition, the MOPA configuration and the innovative pumping scheme designed in chapters 3 and 4, respectively, for the chalcogenide glass will be modified in order to be applied to the dysprosium-doped ZBLAN glass.

6.4 Conclusion

A continuous-wave Dy^{3+}:ZBLAN fiber laser has been modeled and numerically investigated. A maximum slope efficiency of $\eta_s = 54\,\%$, higher than half of the Stokes efficiency limit of $93\,\%$, and a power threshold as low as $P_{th} = 147\,\mathrm{mW}$ have been calculated. These characteristics promise high lasing efficiency as demonstrated in similar experimental set-ups [65].

Chapter 7

Design of a gain-switched Dy^{3+}:ZBLAN fiber laser

7.1 Introduction

In this chapter, a time-dependent numerical model of a dysprosium-doped ZBLAN glass fiber is developed in order to design a pulsed laser emitting at about 3 µm wavelength, by employing an in-band pumping scheme. The gain switching method, in which a suitable input pump modulates the optical gain, is considered to achieve pulsed operation. A number of design parameters are changed to optimize the laser performance. Stable single-pulse gain-switching regime with an output signal peak power close to 59 W and a full width at half maximum (FWHM) pulse duration shorter than 184 ns is simulated for a fiber with dopant concentration of 2000 ppm, by employing a pulsed input pump with a peak power of 5 W and a repetition rate of 100 kHz at the wavelength of 2.8 µm. These characteristics are very promising and theoretically predict the feasibility of a laser which can find application in many areas such as chemical, biological and environmental monitoring. In fact, till now only CW Dy^{3+}-doped ZBLAN fiber lasers with in-band pumped configuration have been demonstrated [65–68]. Therefore, this investigation, which employs simulation parameters pertaining to commercially available fluoride fibers [68], could pave the way to

the pulsed operation for this kind of lasers.

The theoretical model is described in section 2.2.3.

7.2 Numerical results

The fiber considered in the simulation is a step-index fluoride fiber, commercially available (Le Verre Fluoré), with core diameter $d_{\text{core}} = 12.5\,\mu\text{m}$, cladding diameter $d_{\text{clad}} = 125\,\mu\text{m}$ and numerical aperture $NA = 0.16$. The absorption and emission cross sections for the pump are $\sigma_{12}(\nu_{\text{p}}) = 3.26 \times 10^{-25}\,\text{m}^2$ and $\sigma_{21}(\nu_{\text{p}}) = 2.04 \times 10^{-25}\,\text{m}^2$, respectively. The absorption and emission cross sections for the signal are $\sigma_{12}(\nu_{\text{s}}) = 9.61 \times 10^{-26}\,\text{m}^2$ and $\sigma_{21}(\nu_{\text{s}}) = 1.65 \times 10^{-25}\,\text{m}^2$, respectively. The ${}^6\text{H}_{13/2} \rightarrow {}^6\text{H}_{15/2}$ radiative lifetime is $\tau_2 = 13.7\,\text{ms}$ and the ${}^6\text{H}_{13/2} \rightarrow {}^6\text{H}_{15/2}$ nonradiative decay rate is $R_{21} = 1539\,\text{s}^{-1}$. The equivalent ASE noise bandwidth is $B_{\text{ase}} = 100\,\text{nm}$. The glass refractive index is $n = 1.48$ at the wavelength $\lambda = 2.88\,\mu\text{m}$. A suitable Sellmeier equation is considered to model the glass cladding refractive index dispersion, while keeping constant the numerical aperture NA. The group velocities for the pump and the signal are $v_{\text{g}}^{\text{p}} = 2.025 \times 10^8\,\text{m}\,\text{s}^{-1}$ and $v_{\text{g}}^{\text{s}} = 2.027 \times 10^8\,\text{m}\,\text{s}^{-1}$, respectively. They are very close, as expected. The optical losses are assumed to be equal to $\alpha = 0.9\,\text{dB}\,\text{m}^{-1}$ at both pump and signal wavelengths, i.e. high enough to include potential losses due to the splicing of the different parts of the laser cavity. The dopant concentration is $N_{\text{Dy}} = 2000\,\text{ppm} = 3.63 \times 10^{25}\,\text{ions/m}^3$. The first mirror reflectivity is $R_1 = 99\,\%$. The pump and signal wavelengths are $\lambda_{\text{p}} = 2.8\,\mu\text{m}$ and $\lambda_{\text{s}} = 3.0\,\mu\text{m}$, respectively. The input pump peak power is $P_{\text{p}}^{\text{peak}} = 5\,\text{W}$. The time step size is $\Delta t = 5\,\text{ns}$ and the space step size is $\Delta z = 1\,\text{cm}$. In the following, the excitation pump waveform is assumed to be a square wave with variable amplitude, repetition rate and duty cycle. The time-dependent model has been validated by considering, as particular case, input pump power pulses with duty cycle $D = 100\,\%$, i.e. CW operation. All the parameters of the laser experimental set-up reported in [65] have been considered. By supposing a realistic coupling efficiency of about $30\,\%$, an output laser power very close to the

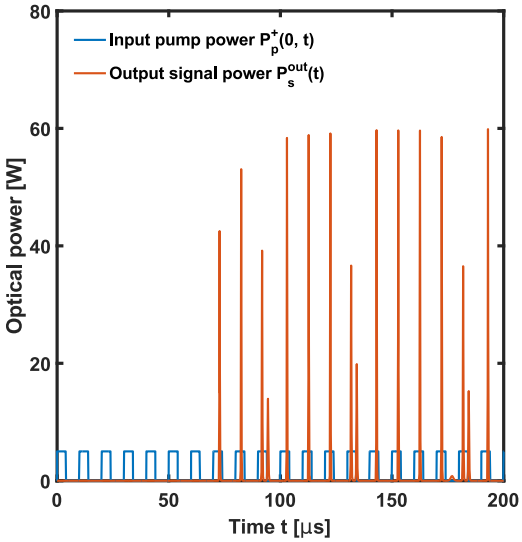

Figure 7.1: Input pump power pulses $P_{\mathrm{p}}^{+}(0,t)$ (blue pulses) and output signal power pulses $P_{\mathrm{s}}^{\mathrm{out}}(t)$ (red pulses) as a function of the time. Input pump duty cycle $D = 40\,\%$, laser cavity length $L = 1\,\mathrm{m}$, pump repetition rate $f_{\mathrm{R}} = 100\,\mathrm{kHz}$, second mirror reflectivity $R_2 = 50\,\%$.

experimental one has been obtained, with an agreement within $5\,\%$.

As an example of time-dependent simulation, Fig. 7.1 shows the unstable output signal pulses and the input pump pulses as a function of the time, input pump duty cycle $D = 40\,\%$, laser cavity length $L = 1\,\mathrm{m}$ and second mirror reflectivity $R_2 = 50\,\%$. It is apparent that a proper design of the laser is mandatory in order to obtain stable single-pulse emission.

The output laser characteristics are investigated as a function of: i) laser cavity length L, see Figs. 7.2–7.4; ii) second mirror reflectivity R_2, see Figs. 7.5–7.7; iii) input pump duty cycle D, see Figs. 7.8–7.10. Only points belonging to single-pulse stability regions are shown.

Fig. 7.2 shows the output signal peak power $P_{\mathrm{s}}^{\mathrm{peak}}$ as a function of the laser cavity length L for different input pump duty cycles. The curves exhibit an increasing behavior for small cavity lengths, they reach the maximum for $L = 0.8\,\mathrm{m}$ and then they decrease by increasing the cavity length. In other words, for a given laser configuration and dopant concentration, even by changing the average input pump power by considering different duty cycle values, the length $L = 0.8\,\mathrm{m}$ seems to be the optimal

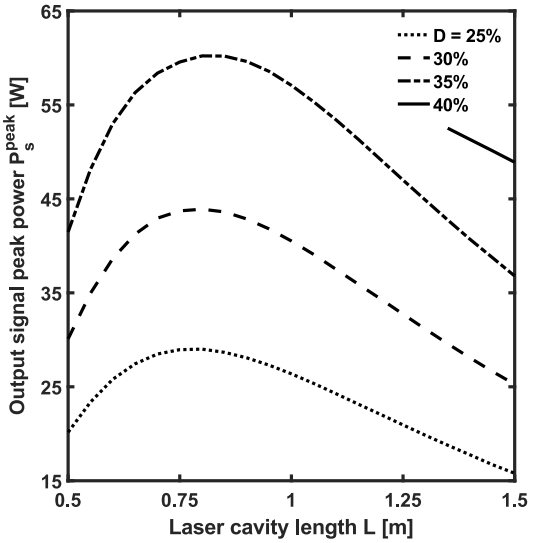

Figure 7.2: Output signal peak power $P_{\mathrm{s}}^{\mathrm{peak}}$ as a function of the cavity length L for different input pump duty cycles, $D = 25\,\%$ (dotted curve), $D = 30\,\%$ (dashed curve), $D = 35\,\%$ (dash-dot curve), $D = 40\,\%$ (solid curve). Pump repetition rate $f_{\mathrm{R}} = 100\,\mathrm{kHz}$; second mirror reflectivity $R_2 = 50\,\%$.

one.

Fig. 7.3 shows the output signal pulse width τ_{s} as a function of the laser cavity length L for different input pump duty cycles. The simulation parameters are the same of Fig. 7.2. For short fibers, the pulse width exhibits a decreasing behavior and reaches a minimum at $L = 0.75$–$0.85\,\mathrm{m}$, then it increases. The shortest achievable duration is about $\tau_{\mathrm{s}} = 180\,\mathrm{ns}$, for $D = 35\,\%$. For $D = 40\,\%$, the performance deteriorates due to the stability region limited by non-optimal cavity lengths. The related pulse energy E_{s} is shown in Fig. 7.4. The maximum achievable pulse energy is about $E_{\mathrm{s}} = 11\,\mu\mathrm{J}$, for $D = 35\,\%$, leading to an optical-to-optical efficiency higher than $\eta = 60\,\%$.

Fig. 7.5 shows the output signal peak power $P_{\mathrm{s}}^{\mathrm{peak}}$ as a function of the output mirror reflectivity R_2 for different input pump duty cycles. The curves exhibit an increasing behavior for low reflectivities and a decreasing behavior for high reflectivities. The maximum is reached around $R_2 = 50\,\%$, even if the pump duty cycle changes from $D = 25\,\%$ to $D = 35\,\%$. It is worthwhile noting that, for higher pump duty cycles, the single-pulse stability region gets narrower and narrower.

Fig. 7.6 shows the output signal pulse width τ_{s} as a function of the output mirror

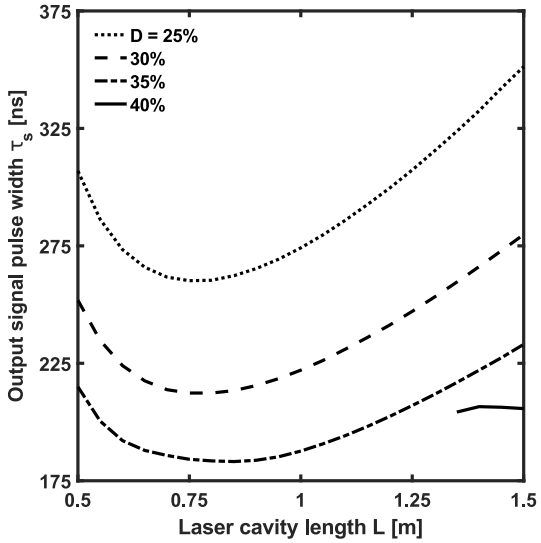

Figure 7.3: Output signal pulse width τ_{s} as a function of the cavity length L for different input pump duty cycles, $D = 25\,\%$ (dotted curve), $D = 30\,\%$ (dashed curve), $D = 35\,\%$ (dash-dot curve), $D = 40\,\%$ (solid curve). Pump repetition rate $f_{\mathrm{R}} = 100\,\mathrm{kHz}$; second mirror reflectivity $R_2 = 50\,\%$.

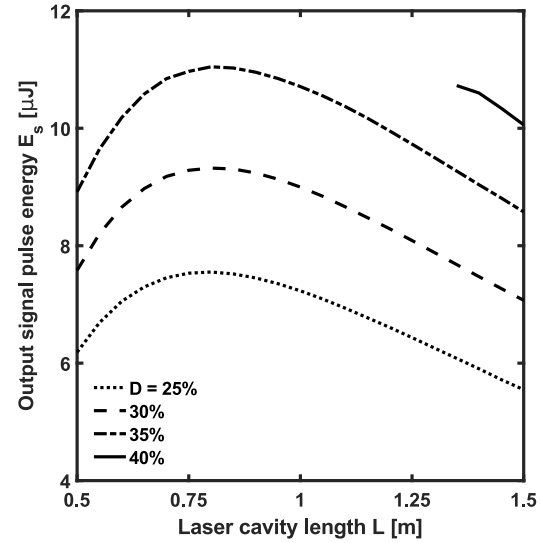

Figure 7.4: Output signal pulse energy E_{s} as a function of the cavity length L for different input pump duty cycles, $D = 25\,\%$ (dotted curve), $D = 30\,\%$ (dashed curve), $D = 35\,\%$ (dash-dot curve), $D = 40\,\%$ (solid curve). Pump repetition rate $f_{\mathrm{R}} = 100\,\mathrm{kHz}$; second mirror reflectivity $R_2 = 50\,\%$.

reflectivity R_2 for different input pump duty cycles. The simulation parameters are the same of Fig. 7.5. The curves exhibit a monotone decreasing behavior, with a very steep slope for low reflectivities. For reflectivities greater than $R_2 = 40\,\%$, the pulse width is almost constant. Again, the best value of about $\tau_{\mathrm{s}} = 180\,\mathrm{ns}$ is obtained for

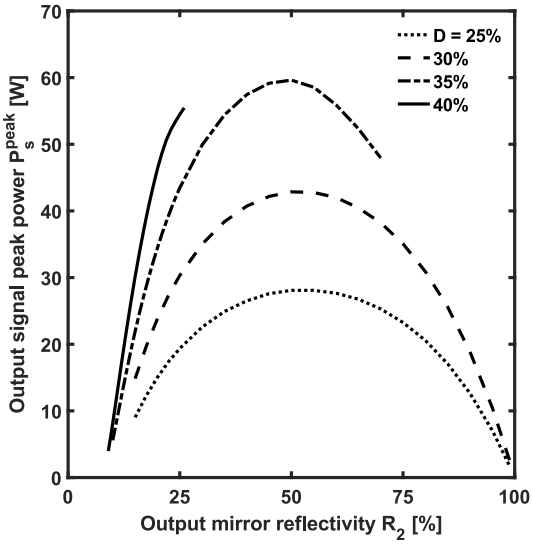

Figure 7.5: Output signal peak power $P_{\mathrm{s}}^{\mathrm{peak}}$ as a function of the output mirror reflectivity R_2 for different input pump duty cycles, $D = 25\,\%$ (dotted curve), $D = 30\,\%$ (dashed curve), $D = 35\,\%$ (dash-dot curve), $D = 40\,\%$ (solid curve). Pump repetition rate $f_{\mathrm{R}} = 100\,\mathrm{kHz}$; cavity length $L = 0.9\,\mathrm{m}$.

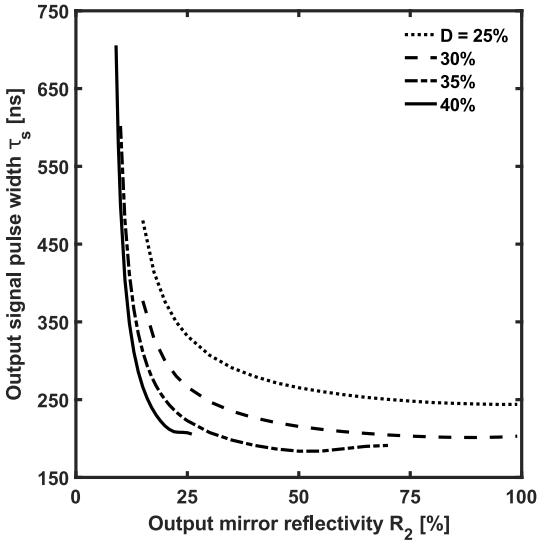

Figure 7.6: Output signal pulse width τ_{s} as a function of the output mirror reflectivity R_2 for different input pump duty cycles, $D = 25\,\%$ (dotted curve), $D = 30\,\%$ (dashed curve), $D = 35\,\%$ (dash-dot curve), $D = 40\,\%$ (solid curve). Pump repetition rate $f_{\mathrm{R}} = 100\,\mathrm{kHz}$; cavity length $L = 0.9\,\mathrm{m}$.

$R_2 = 50\,\%$, for the case $D = 35\,\%$. Fig. 7.7 shows the related pulse energy E_{s}. Like the previous case, the behavior is similar to that of Fig. 7.5, although the maximum pulse energy is obtained for $D = 40\,\%$.

Fig. 7.8 depicts the output signal peak power $P_{\mathrm{s}}^{\mathrm{peak}}$ as a function of the input

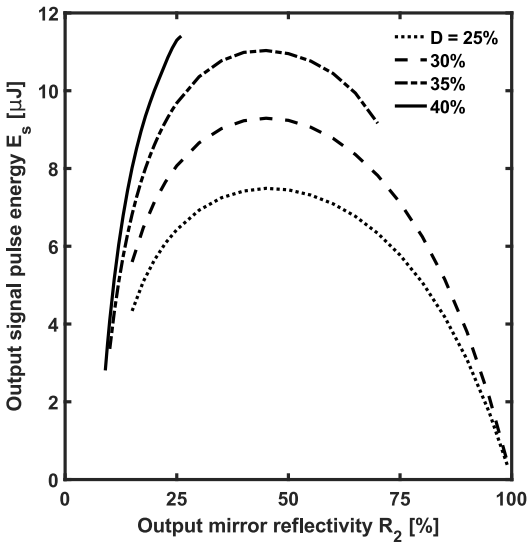

Figure 7.7: Output signal pulse energy E_s as a function of the output mirror reflectivity R_2 for different input pump duty cycles, $D = 25\,\%$ (dotted curve), $D = 30\,\%$ (dashed curve), $D = 35\,\%$ (dash-dot curve), $D = 40\,\%$ (solid curve). Pump repetition rate $f_\mathrm{R} = 100\,\mathrm{kHz}$; cavity length $L = 0.9\,\mathrm{m}$.

pump duty cycle D for different pump repetition rates. It is worthwhile noting that these curves refer to the average signal power, defined as $P_\mathrm{s}^\mathrm{avg} = E_\mathrm{s} f_\mathrm{R}$, varying from $P_\mathrm{s}^\mathrm{avg} = 0.04\,\mathrm{W}$ to $P_\mathrm{s}^\mathrm{avg} = 1.45\,\mathrm{W}$ and represent the regions in which stable output pulses are generated. It can be seen that a repetition rate as high as $f_\mathrm{R} = 140\,\mathrm{kHz}$ is feasible. Fig. 7.9 shows the output signal pulse width τ_s as a function of the input pump duty cycle D for different pump repetition rates, for the same simulation parameters of Fig. 7.8. The curves are monotone decreasing for all repetition rate values, with a slope less and less steep as the repetition rate increases. In addition, the pulse width never falls below $\tau_\mathrm{s} = 180\,\mathrm{ns}$. This is probably due to an inherent limitation of this fiber laser in gain switching operation. Also in this case, the pulse energy E_s, which is shown in Fig. 7.10, exhibits a behavior similar to that of the pulse peak power. Energies of about $E_\mathrm{s} = 10$–$11\,\mu\mathrm{J}$ can be achieved for each value of the repetition rate, which provides great flexibility in the design of the device for both low and high repetition rates applications.

Figs. 7.8–7.10 are obtained for nearly optimized cavity length L and second mirror reflectivity R_2 and allow identifying the maximum pulse peak power $P_\mathrm{s}^\mathrm{peak}$, width τ_s

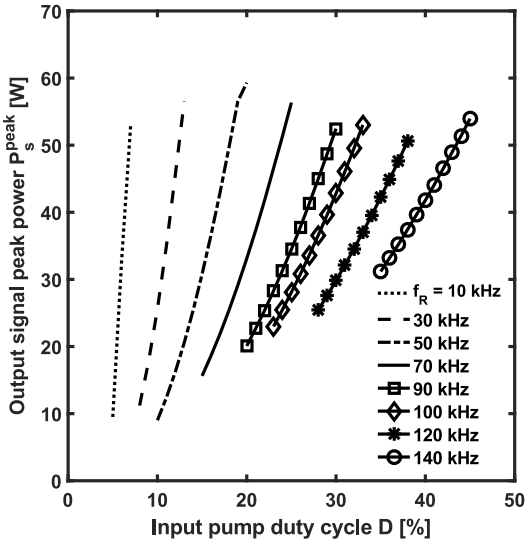

Figure 7.8: Output signal peak power $P_{\mathrm{s}}^{\mathrm{peak}}$ as a function of input pump duty cycle D for different pump repetition rates, $f_{\mathrm{R}} = 10\,\mathrm{kHz}$ (dotted curve), $f_{\mathrm{R}} = 30\,\mathrm{kHz}$ (dashed curve), $f_{\mathrm{R}} = 50\,\mathrm{kHz}$ (dash-dot curve), $f_{\mathrm{R}} = 70\,\mathrm{kHz}$ (solid curve), $f_{\mathrm{R}} = 90\,\mathrm{kHz}$ (solid curve with square markers), $f_{\mathrm{R}} = 100\,\mathrm{kHz}$ (solid curve with diamond markers), $f_{\mathrm{R}} = 120\,\mathrm{kHz}$ (solid curve with asterisk markers), $f_{\mathrm{R}} = 140\,\mathrm{kHz}$ (solid curve with circle markers). Cavity length $L = 0.9\,\mathrm{m}$; second mirror reflectivity $R_2 = 50\,\%$.

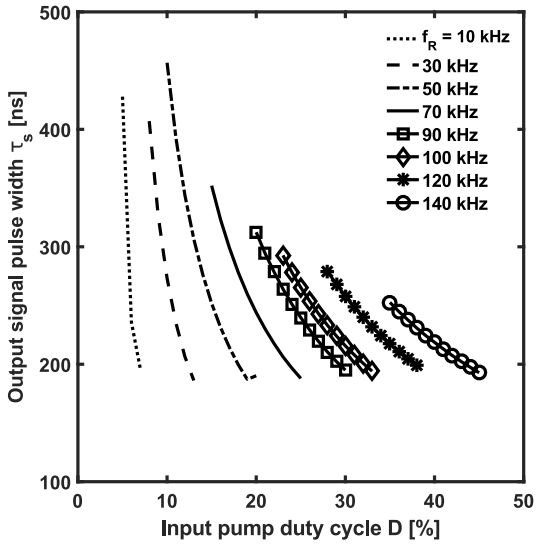

Figure 7.9: Output signal pulse width τ_{s} as a function of input pump duty cycle D for different pump repetition rates, $f_{\mathrm{R}} = 10\,\mathrm{kHz}$ (dotted curve), $f_{\mathrm{R}} = 30\,\mathrm{kHz}$ (dashed curve), $f_{\mathrm{R}} = 50\,\mathrm{kHz}$ (dash-dot curve), $f_{\mathrm{R}} = 70\,\mathrm{kHz}$ (solid curve), $f_{\mathrm{R}} = 90\,\mathrm{kHz}$ (solid curve with square markers), $f_{\mathrm{R}} = 100\,\mathrm{kHz}$ (solid curve with diamond markers), $f_{\mathrm{R}} = 120\,\mathrm{kHz}$ (solid curve with asterisk markers), $f_{\mathrm{R}} = 140\,\mathrm{kHz}$ (solid curve with circle markers). Cavity length $L = 0.9\,\mathrm{m}$; second mirror reflectivity $R_2 = 50\,\%$.

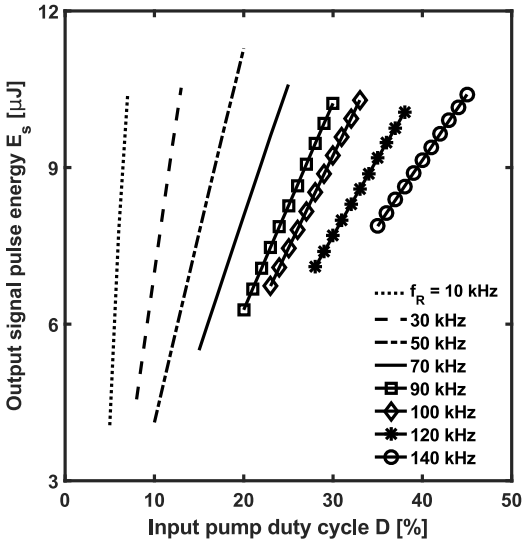

Figure 7.10: Output signal pulse energy E_s as a function of input pump duty cycle D for different pump repetition rates, $f_\mathrm{R} = 10\,\mathrm{kHz}$ (dotted curve), $f_\mathrm{R} = 30\,\mathrm{kHz}$ (dashed curve), $f_\mathrm{R} = 50\,\mathrm{kHz}$ (dash-dot curve), $f_\mathrm{R} = 70\,\mathrm{kHz}$ (solid curve), $f_\mathrm{R} = 90\,\mathrm{kHz}$ (solid curve with square markers), $f_\mathrm{R} = 100\,\mathrm{kHz}$ (solid curve with diamond markers), $f_\mathrm{R} = 120\,\mathrm{kHz}$ (solid curve with asterisk markers), $f_\mathrm{R} = 140\,\mathrm{kHz}$ (solid curve with circle markers). Cavity length $L = 0.9\,\mathrm{m}$; second mirror reflectivity $R_2 = 50\,\%$.

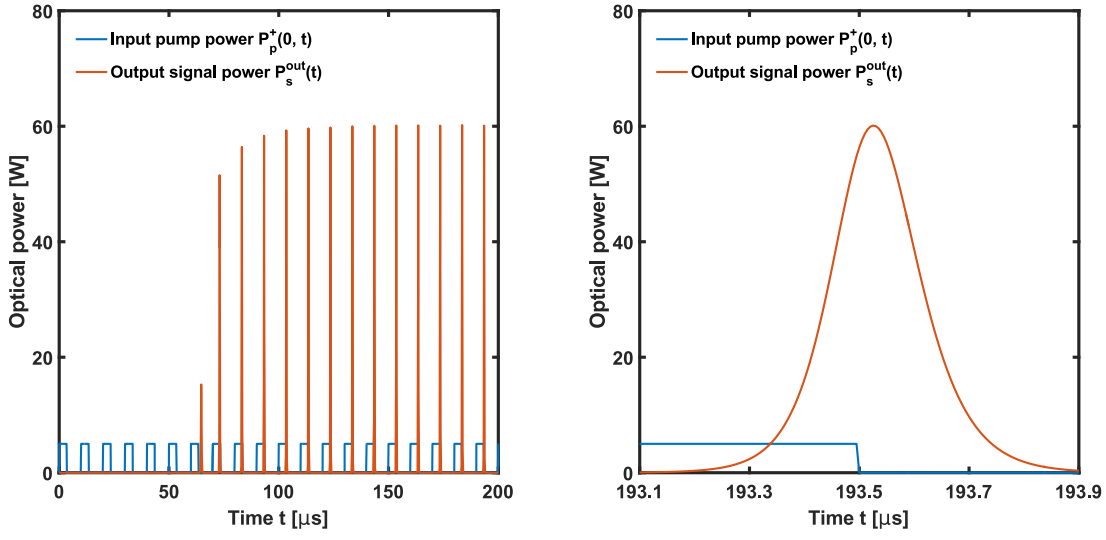

(a) (b)

Figure 7.11: (a) Input pump power pulses $P_\mathrm{p}^{+}(0,t)$ (blue pulses) and output signal power pulses $P_\mathrm{s}^\mathrm{out}(t)$ (red pulses) as a function of the time. Input pump duty cycle $D = 35\,\%$, laser cavity length $L = 0.8\,\mathrm{m}$, pump repetition rate $f_\mathrm{R} = 100\,\mathrm{kHz}$, second mirror reflectivity $R_2 = 50\,\%$. (b) Zoom of a single output signal pulse.

and energy E_s achievable by varying the operating condition in terms of repetition rate f_R and duty cycle D.

Fig. 7.11(a) reports the generated pulses for the optimized laser, showing the stable output signal pulses and the input pump pulses as a function of the time, input pump duty cycle $D = 35\,\%$, laser cavity length $L = 0.8\,\mathrm{m}$ and second mirror reflectivity $R_2 = 50\,\%$. After a build-up time of about $t = 65\,\mu\mathrm{s}$, the first pulse is generated. Stable gain-switched pulsed regime with an output peak power of $P_s^{peak} = 59\,\mathrm{W}$ and a pulse duration of $\tau_s = 184\,\mathrm{ns}$, corresponding to an output energy of $E_s = 11\,\mu\mathrm{J}$, is obtained after $t = 110\,\mu\mathrm{s}$. Fig. 7.11(b) depicts a zoom of a single output signal pulse.

The obtained results are promising, even with reference to the state of the art [69–71]. As examples, the following characteristics of gain switched lasers were reported in the recent literature: i) in [69], pulse trains at $\lambda = 2.8\,\mu\mathrm{m}$ with a maximum peak power of $P_s^{peak} = 68\,\mathrm{W}$, a duration of $\tau_s = 300\,\mathrm{ns}$ and a pulse energy of $E_s = 20.4\,\mu\mathrm{J}$ at the repetition rate of $f_R = 100\,\mathrm{kHz}$ in an Er^{3+}-doped ZBLAN fiber laser; ii) in [70], pulse trains at $\lambda = 2.8\,\mu\mathrm{m}$ with a maximum peak power of $P_s^{peak} = 3.85\,\mathrm{W}$, a duration of $\tau_s = 1.55\,\mu\mathrm{s}$ and a pulse energy of $E_s = 5.97\,\mu\mathrm{J}$ at the repetition rate of $f_R = 20\,\mathrm{kHz}$ in the same fiber; iii) in [71], pulse trains at $\lambda = 2.98\,\mu\mathrm{m}$ with a maximum peak power of $P_s^{peak} = 3.26\,\mathrm{W}$, a duration of $\tau_s = 1.49\,\mu\mathrm{s}$ and a pulse energy of $E_s = 4.87\,\mu\mathrm{J}$ at the repetition rate of $f_R = 80\,\mathrm{kHz}$ in a Ho^{3+}-doped ZBLAN fiber. In view of these results, the proposed ZBLAN fiber laser doped with Dy^{3+} ions constitutes an attractive solution since it allows the generation of pulse trains at $\lambda = 3\,\mu\mathrm{m}$ with a maximum peak power of $P_s^{peak} = 59\,\mathrm{W}$, a duration of $\tau_s = 184\,\mathrm{ns}$, a pulse energy of $E_s = 11\,\mu\mathrm{J}$ and an optical-to-optical efficiency of $\eta = 60\,\%$ at the repetition rate of $f_R = 100\,\mathrm{kHz}$. Moreover, the proposed solution promises stable gain-switching operation even at higher repetition rates, e.g. at $f_R = 140\,\mathrm{kHz}$.

7.3 Conclusion

A Dy^{3+}:ZBLAN fiber laser operating in gain switching regime is accurately modeled and numerically investigated. By employing an input pump of 5 W with 100 kHz repetition rate and 35 % duty cycle, pulses with a peak power of 59 W and a full width at half maximum (FWHM) width of 184 ns can be obtained. The related energy is 11 µJ, which corresponds to an optical-to-optical efficiency larger than 60 %. The parameters of a commercially available fluoride fiber are used. Therefore, the proposed investigation can be considered a feasibility investigation of a pulsed laser which can be constructed by employing fluoride fibers available on the market.

Conclusion

The feasibility investigation of different fiber lasers for mid-IR applications has been accurately performed via home-made computer codes. The light generation/amplification in the mid-IR wavelength range has been obtained by considering chalcogenide and ZBLAN host glasses and different pumping schemes. The simulation results refer to five different devices.

Firstly, an optical source exploiting a master oscillator power amplifier (MOPA) configuration is designed and optimized. The pump and signal wavelengths are 1709 nm and 4384 nm, respectively. The MOPA configuration overcomes the limits of a simple laser configuration and allows a better exploitation of the pump power, increasing the overall system efficiency. An output signal power as high as 637 mW at 4384 nm wavelength can be achieved with a pump power of 3 W. The related efficiency exceeds 21 %.

An innovative double pumping scheme for the same Dy^{3+}:$Ga_5Ge_{20}Sb_{10}S_{65}$ is proposed in order to design a fiber laser which provides an optical beam emission close to 4400 nm wavelength by employing two pump beams at 2850 nm and 4092 nm wavelengths. An output signal power close to 350 mW is simulated for the input pump #1 power of 50 mW and the input pump #2 power of 1 W, therefore with an overall efficiency greater than 33 %.

The particle swarm optimization (PSO) technique is exploited in order to maximize the optical gain of an in-band pumped Dy^{3+}-doped ZBLAN fiber amplifier. A maximum optical gain as high as 15.56 dB at 2.95 µm can be achieved with an input pump power of 1 W at 2.72 µm, for a fiber with dopant concentration of 2000 ppm and

length of 2.34 m. The simulated noise figure is 5.86 dB.

The same Dy^{3+}-doped ZBLAN glass is employed to design and optimize a highly efficient continuous-wave (CW) fiber laser emitting around 3 µm wavelength. The model allows the optimization of both the slope efficiency and the power threshold of the laser. By applying the PSO algorithm, a maximum slope efficiency of 54 % has been calculated, which is higher than half of the Stokes efficiency limit of 93 %. The related power threshold is 147 mW.

Finally, a time-dependent numerical model of a Dy^{3+}-doped ZBLAN glass fiber is developed to investigate the feasibility of a pulsed mid-IR laser emitting at about 3 µm wavelength. Gain switching technique is exploited to obtain a stable single-pulse emission. Simulations are performed by means of a modified finite-difference time-domain (FDTD) algorithm. The laser can emit pulses with a peak power of 59 W and a full width at half maximum (FWHM) width of 184 ns, by employing an input pump of 5 W with 100 kHz repetition rate and 35 % duty cycle. The related pulse energy is 11 µJ, which corresponds to an optical-to-optical efficiency larger than 60 %.

In all the cases, spectroscopic parameters measured on preliminary samples of chalcogenide and ZBLAN glasses are taken into account to fulfill realistic simulations. The proposed feasibility investigation show that it is possible to obtain high beam quality mid-IR sources by employing both chalcogenide and ZBLAN glasses. Chalcogenide glasses are a subject of strong interest for the research. They require further technological efforts, from the point of view of glass purification, fiber drawing and doping with rare earths, but are extremely attractive for their potential at very long wavelength till 20 µm. Conversely, ZBLAN optical fibers are available on the market and allow more feasible solutions. A first experiment pertaining to the CW dysprosium-doped ZBLAN fiber laser has been performed by employing non-optimized components. The aim of the future activity is the fabrication of the pulsed dysprosium-doped ZBLAN fiber laser and the implementation of the double pumping scheme and the MOPA configuration, suitably adapted, to the ZBLAN glass.

List of publications

International Journals:

1. M. C. Falconi, G. Palma, F. Starecki, V. Nazabal, J. Troles, S. Taccheo, M. Ferrari, and F. Prudenzano, "Design of an efficient pumping scheme for mid-IR Dy^{3+}:$Ga_5Ge_{20}Sb_{10}S_{65}$ PCF fiber laser," *Photonics Technology Letters, IEEE*, vol. 28, no. 18, pp. 1984–1987, Sep. 2016.

2. G. Palma, M. C. Falconi, F. Starecki, V. Nazabal, T. Yano, T. Kishi, T. Kumagai, and F. Prudenzano, "Novel double step approach for optical sensing via microsphere WGM resonance," *Optics Express*, vol. 24, no. 23, pp. 26956-26971, Nov. 2016.

3. M. C. Falconi, G. Palma, F. Starecki, V. Nazabal, J. Trolès, J.-L. Adam, S. Taccheo, M. Ferrari, and F. Prudenzano, "Dysprosium-doped chalcogenide master oscillator power amplifier (MOPA) for mid-IR emission," *Journal of Lightwave Technology*, vol. 35, no. 2, pp. 265-273, Jan. 2017.

4. G. Palma, M. C. Falconi, F. Starecki, V. Nazabal, J. Ari, L. Bodiou, J. Charrier, Y. Dumeige, E. Baudet, and F. Prudenzano, "Design of praseodymium-doped chalcogenide micro-disk emitting at 4.7 µm," *Optics Express*, vol. 25, no. 6, pp. 7014-7030, Mar. 2017.

5. M. C. Falconi, D. Laneve, and F. Prudenzano, "Advances in mid-IR fiber lasers: tellurite, fluoride and chalcogenide," *Fibers*, vol. 5, no. 2, Jun. 2017.

6. F. Chiavaioli, D. Laneve, D. Farnesi, M. C. Falconi, G. Nunzi Conti, F. Baldini, and F. Prudenzano, "Long period grating-based fiber coupling to WGM microresonators," *Micromachines*, vol. 9, no. 7, Jul. 2018.

7. D. Laneve, M. C. Falconi, M. Bozzetti, G. Rutigliani, R. A. Prisco, V. Dimiccoli, and F. Prudenzano, "An efficient hybrid approach to the electromagnetic design of resonant cavities for side-coupled linacs," *IET The Journal of Engineering*, Jul. 2018. Accepted for publication.

8. D. Laneve, M. C. Falconi, M. Bozzetti, G. Rutigliani, R. A. Prisco, V. Dimiccoli, and F. Prudenzano, "Electromagnetic design of microwave cavities for side-coupled linear accelerators: a hybrid numerical/analytical approach," in *IEEE Transactions on Nuclear Science*, vol. 65, no. 8, pp. 2233-2239, Aug. 2018.

9. S. Sujecki, L. Sojka, A. B. Seddon, T. M. Benson, E. Barney, M. C. Falconi, F. Prudenzano, M. Marciniak, H. Baghdasaryan, P. Peterka, and S. Taccheo, "Comparative modeling of infrared fiber lasers," *Photonics*, vol. 5, no. 4, Nov. 2018.

10. M. C. Falconi, D. Laneve, M. Bozzetti, T. T. Fernandez, G. Galzerano, and F. Prudenzano, "Design of an efficient pulsed Dy^{3+}:ZBLAN fiber laser operating in gain switching regime," *Journal of Lightwave Technology*, vol. 36, no. 23, pp. 5327-5333, Dec. 2018.

Papers in proceedings of international conferences:

1. M. C. Falconi, G. Palma, R. Chahal, F. Starecki, V. Nazabal, J. Troles, J.-L. Adam, and F. Prudenzano, "Design of mid-IR microstructured fiber light source based on dysprosium doped chalcogenide glass," *Microwave Symposium (MMS), 2015 15th Mediterranean*, Lecce (Italy), 30 Nov-2 Dec 2015.

2. G. Palma, M. C. Falconi, F. Starecki, V. Nazabal, L. Bodiou, Y. Dumeige, J. Lemaitre, J. Charrier, and F. Prudenzano, "Design of rare-earth doped chalco-

genide microresonators for biosensing in mid-IR," *Transparent Optical Networks (ICTON), 2016 18th International Conference on*, Trento, 10-14 July 2016.

3. M. C. Falconi, G. Palma, F. Starecki, V. Nazabal, J.-L. Adam, S. Taccheo, M. Ferrari, and F. Prudenzano, "Novel pumping schemes of mid-IR photonic crystal fiber lasers for aerospace applications," *Transparent Optical Networks (ICTON), 2016 18th International Conference on*, Trento, 10-14 July 2016 (Invited paper).

4. M. C. Falconi, G. Palma, F. Starecki, V. Nazabal, J. Troles, J.-L. Adam, S. Taccheo, M. Ferrari, and F. Prudenzano, "Recent advances on pumping schemes for mid-IR PCF lasers," in *Proceedings of SPIE Optical Components and Materials XIV*, San Francisco (United States), 30 Jan-1 Feb 2017 (Invited paper).

5. M. C. Falconi, G. Palma, A. Ameruoso, C. Laterza, S. Popolizio, L. Rinaldi, A. Rizzi, G. Testa, F. Tragni, F. Chiavaioli, F. Baldini, D. Farnesi, G. Nunzi Conti, S. Pelli, G. C. Righini, S. Soria, C. Trono, and F. Prudenzano, "Design of microspheres and microbubbles for environmental chemical/biological optical sensing," *2017 IEEE International Instrumentation and Measurement Technology Conference (I2MTC)*, Torino, Italy, 2017, pp. 1-6.

6. D. Laneve, M. C. Falconi, G. Palma, A. Crudele, and F. Prudenzano, "Optical microresonators for biomedicine applications," *Transparent Optical Networks (ICTON), 2017 19th International Conference on*, Girona, 2-6 July 2017, pp. 1-5 (Invited paper).

7. M. C. Falconi, D. Laneve, C. Clemente, D. Gurban, T. T. Fernandez, G. Galzerano, and F. Prudenzano, "Global optimization via evolutionary approach of a Dy^{3+}:ZBLAN fiber amplifier for mid-IR applications," in *Proceedings of SPIE Fiber Lasers and Glass Photonics: Materials through Applications*, Strasbourg (France), 22-26 Apr 2018.

8. S. Sujecki, L. Sojka, A. Seddon, T. Benson, M. C. Falconi, F. Prudenzano, M. Marciniak, H. Baghdasary, P. Peterka, and S. Taccheo, "Comparative study of

infrared fiber laser models," in *Proceedings of SPIE Fiber Lasers and Glass Photonics: Materials through Applications*, Strasbourg (France), 22-26 Apr 2018.

9. M. C. Falconi, D. Laneve, M. Bozzetti, T. T. Fernandez, G. Galzerano, and F. Prudenzano, "Continuous-wave and pulsed optical fiber lasers for medium infrared applications," *Transparent Optical Networks (ICTON), 2018 20th International Conference on*, Bucharest, 1-5 July 2018, pp. 1-6 (Invited paper).

10. D. Laneve, D. Farnesi, F. Baldini, M. C. Falconi, G. Nunzi Conti, F. Prudenzano, F. Chiavaioli, and S. Soria, "Optical coupling of spherical microresonators with tapered fibers for chemical/biomedical applications," *2018 IEEE International Workshop on Metrology for the Sea (MetroSea2018)*, Bari, Italy, 8-10 October 2018, pp. 1-5.

Abstracts of international conferences:

1. D. Laneve, M. C. Falconi, G. Palma, F. Chiavaioli, G. Nunzi Conti, G. C. Righini, C. Trono, and F. Prudenzano, "Optical microresonators for chemical and biological sensing applications," in *EOS Topical Meeting on Optical MicroSystems (OμS'17)*, Capri, Italy, 10-14 settembre 2017.

2. M. C. Falconi, D. Laneve, and F. Prudenzano, "Numerical modeling of a Dy^{3+}:ZBLAN fiber laser operating in gain switching regime," in *7th International Workshop on Photoluminescence in Rare Earths: Photonic Materials and Devices (PRE'17)*, Rome, Italy, 30 novembre-2 dicembre 2017.

3. M. C. Falconi, D. Laneve, C. Clemente, A. Crudele, T. T. Fernandez, G. Galzerano, and F. Prudenzano, "Mid-IR fiber amplifier based on dysprosium-doped ZBLAN glass," in *1st International Conference on Dielectric Photonic Devices and Systems Beyond Visible (D-Photon 2018)*, Bari, Italy, 1-2 ottobre 2018.

4. D. Laneve, M. C. Falconi, F. Chiavaioli, D. Farnesi, G. Nunzi Conti, S. Soria, F. Baldini, and F. Prudenzano, "Optical resonators for chemical/biological sens-

ing," in *1st International Conference on Dielectric Photonic Devices and Systems Beyond Visible (D-Photon 2018)*, Bari, Italy, 1-2 ottobre 2018.

Papers in proceedings of national conferences:

1. M. C. Falconi, G. Palma, F. Starecki, V. Nazabal, J. Troles, S. Taccheo, M. Ferrari, and F. Prudenzano, "Dysprosium-doped chalcogenide fiber laser for medical applications", in *XXI RiNEm, Riunione Nazionale di Elettromagnetismo*, Parma, 12-14 settembre 2016.

2. G. Palma, M. C. Falconi, F. Starecki, V. Nazabal, L. Bodiou, Y. Dumeige, J. Lemaitre, J. Charrier, and F. Prudenzano, "Design of erbium doped chalcogenide microdisk emitting at 4.5 µm wavelength", in *XXI RiNEm, Riunione Nazionale di Elettromagnetismo*, Parma, 12-14 settembre 2016.

3. M. C. Falconi, D. Laneve, Y. Wang, T. T. Fernandez, G. Galzerano, and F. Prudenzano, "Modelling of dysprosium-doped ZBLAN fiber laser", in *Fotonica AEIT 2017, Convegno Italiano delle Tecnologie Fotoniche*, Padova, 3-5 maggio 2017.

4. D. Laneve, M. C. Falconi, G. Palma, F. Chiavaioli, G. Nunzi Conti, G. C. Righini, C. Trono, and F. Prudenzano, "Microspheres and microbubbles for chemical and biomedicine optical sensing", in *Fotonica AEIT 2017, Convegno Italiano delle Tecnologie Fotoniche*, Padova, 3-5 maggio 2017.

5. M. C. Falconi, D. Laneve, M. Bozzetti, T. T. Fernandez, G. Galzerano, and F. Prudenzano, "Design of an in-band pumped dysprosium-doped ZBLAN fiber amplifier operating at 2.9-3.2 micron," in *XXII RiNEm, Riunione Nazionale di Elettromagnetismo*, Cagliari, 3-6 settembre 2018.

Abstracts of national conferences:

1. M. C. Falconi, G. Palma, F. Starecki, V. Nazabal, J. Troles, S. Taccheo, M. Ferrari, and F. Prudenzano, "Design of a high efficiency mid-IR laser at 4400 nm",

in *Fotonica AEIT 2016, Convegno Italiano delle Tecnologie Fotoniche*, Roma, 6-8 giugno 2016.

2. G. Palma, M. C. Falconi, F. Starecki, V. Nazabal, J. Charrier, L. Bodiou, and F. Prudenzano, "Rare-earth doped microdisks for mid-infrared applications", in *Fotonica AEIT 2016, Convegno Italiano delle Tecnologie Fotoniche*, Roma, 6-8 giugno 2016.

3. M. C. Falconi, D. Laneve, M. Bozzetti, T. T. Fernandez, G. Galzerano, and F. Prudenzano, "Design of a gain-switched Dy^{3+}:ZBLAN fibre laser", in *Fotonica AEIT 2018, Convegno Italiano delle Tecnologie Fotoniche*, Lecce, 23-25 maggio 2018.

4. D. Laneve, M. C. Falconi, G. Palma, V. Gallo, A. Rizzuti, F. Chiavaioli, G. Nunzi Conti, G. C. Righini, S. Soria, C. Trono, and F. Prudenzano, "Feasibility investigation of microspherical resonators for fluid sensing in medicine", in *Fotonica AEIT 2018, Convegno Italiano delle Tecnologie Fotoniche*, Lecce, 23-25 maggio 2018.

Bibliography

[1] M. C. Falconi, G. Palma, F. Starecki, V. Nazabal, J. Troles, J.-L. Adam, S. Taccheo, M. Ferrari, and F. Prudenzano, "Dysprosium-doped chalcogenide master oscillator power amplifier (MOPA) for mid-IR emission," *J. Lightw. Technol.*, vol. 35, no. 2, pp. 265–273, Jan. 2017.

[2] M. C. Falconi, G. Palma, F. Starecki, V. Nazabal, J. Troles, S. Taccheo, M. Ferrari, and F. Prudenzano, "Design of an efficient pumping scheme for mid-IR Dy^{3+}:$Ga_5Ge_{20}Sb_{10}S_{65}$ PCF fiber laser," *IEEE Photon. Technol. Lett.*, vol. 28, no. 18, pp. 1984–1987, Sep. 2016.

[3] M. C. Falconi, D. Laneve, M. Bozzetti, T. T. Fernandez, G. Galzerano, and F. Prudenzano, "Design of an efficient pulsed Dy^{3+}:ZBLAN fiber laser operating in gain switching regime," *J. Lightw. Technol.*, vol. PP, no. 99, pp. 1–1, 2018.

[4] A. D'Orazio, M. De Sario, C. Giasi, L. Mescia, V. Petruzzelli, and F. Prudenzano, "Design of planar optic sensors for hydrocarbon detection," *Opt. Quantum Electron.*, vol. 36, no. 6, pp. 507–526, 2004.

[5] F. Starecki, F. Charpentier, J.-L. Doualan, L. Quetel, K. Michel, R. Chahal, J. Troles, B. Bureau, A. Braud, P. Camy, V. Moizan, and V. Nazabal, "Mid-IR optical sensor for CO_2 detection based on fluorescence absorbance of Dy^{3+}:$Ga_5Ge_{20}Sb_{10}S_{65}$ fibers," *Sens. Actuator B-Chem.*, vol. 207, Part A, no. 5, pp. 518–525, Sep. 2015.

[6] F. Attivissimo, C. G. C. Carducci, A. M. L. Lanzolla, A. Massaro, and M. R. Vadrucci, "A portable optical sensor for sea quality monitoring," *IEEE Sensors J.*, vol. 15, no. 1, pp. 146–153, Jan. 2015.

[7] V. W. S. Chan, "Free-space optical communications," *J. Lightw. Technol.*, vol. 24, no. 12, pp. 4750–4762, Dec. 2006.

[8] H. Kaushal and G. Kaddoum, "Optical communication in space: Challenges and mitigation techniques," *IEEE Commun. Surveys Tuts.*, vol. 19, no. 1, pp. 57–96, Firstquarter 2017.

[9] A. P. Tang, J. M. Kahn, and K.-P. Ho, "Wireless infrared communication links using multi-beam transmitters and imaging receivers," in *Proc. IEEE Int. Conf. Commun.*, vol. 1, Jun. 1996, pp. 180–186.

[10] A. M. Street, P. N. Stavrinou, D. C. O'Brien, and D. J. Edward, "Indoor optical wireless systems - a review," *Opt. Quantum Electron.*, vol. 29, no. 3, pp. 349–378, Mar. 1997.

[11] J. B. Carruthers and J. M. Kahn, "Angle diversity for nondirected wireless infrared communication," *IEEE Trans. Commun.*, vol. 48, no. 6, pp. 960–969, Jun. 2000.

[12] R. S. Quimby, L. B. Shaw, J. S. Sanghera, and I. D. Aggarwal, "Modeling of cascade lasing in Dy : chalcogenide glass fiber laser with efficient output at 4.5 µm," *IEEE Photon. Technol. Lett.*, vol. 20, no. 2, pp. 123–125, Jan. 2008.

[13] D. D. Hudson, "Short pulse generation in mid-IR fiber lasers," *Opt. Fiber Technol.*, vol. 20, no. 6, pp. 631–641, Dec. 2014.

[14] G. Palma, M. C. Falconi, F. Starecki, V. Nazabal, J. Ari, L. Bodiou, J. Charrier, Y. Dumeige, E. Baudet, and F. Prudenzano, "Design of praseodymium-doped chalcogenide micro-disk emitting at 4.7 µm," *Opt. Express*, vol. 25, no. 6, pp. 7014–7030, Mar. 2017.

[15] L. Sojka, Z. Tang, D. Furniss, H. Sakr, Y. Fang, E. Beres-Pawlik, T. M. Benson, A. B. Seddon, and S. Sujecki, "Mid-infrared emission in Tb^{3+}-doped selenide glass fiber," *J. Opt. Soc. Am. B*, vol. 34, no. 3, pp. A70–A79, Mar. 2017.

[16] L. Sojka, Z. Tang, D. Furniss, H. Sakr, E. Beres-Pawlik, A. B. Seddon, T. M. Benson, and S. Sujecki, "Numerical and experimental investigation of mid-infrared laser action in resonantly pumped Pr^{3+} doped chalcogenide fibre," *Opt. Quantum Electron.*, vol. 49, no. 21, pp. 1–15, Jan. 2017.

[17] M. De Sario, L. Mescia, F. Prudenzano, F. Smektala, F. Deseveday, V. Nazabal, J. Troles, and L. Brilland, "Feasibility of Er^{3+}-doped, $Ga_5Ge_{20}Sb_{10}S_{65}$ chalcogenide microstructured optical fiber amplifiers," *Opt. Laser Technol.*, vol. 41, no. 1, pp. 99–106, 2009.

[18] J.-L. Adam and X. Zhang, *Chalcogenide Glasses: Preparation, Properties and Applications*, ser. Electron. Opt. Mater. Sawston, Cambridge, U.K.: Woodhead Publishing, 2014.

[19] J.-L. Adam, L. Brilland, P. Toupin, V. Nazabal, and J. Troles, "Chalcogenide glass fibers for photonic devices," in *2013 15th Int. Conf. Transp. Opt. Netw. (ICTON)*, Jun. 2013, pp. 1–4.

[20] J. Troles and L. Brilland, "Chalcogenide microstructured optical fibres for mid-IR applications," *C. R. Phys.*, vol. 18, no. 1, pp. 19–23, Jan. 2017.

[21] M. Saad, "Fluoride glasses and fiber for Mid-IR applications," in *2014 IEEE Photon. Soc. Summer Top. Meet. Series*, Jul. 2014, pp. 55–56.

[22] D. Starodubov, S. Mechery, D. Miller, C. Ulmer, P. Willems, J. Ganley, and D. Tucker, "ZBLAN fibers: from zero gravity tests to orbital manufacturing," in *Imag. Appl. Opt. 2014*, 2014, p. AM4A.2.

[23] R. Allen, L. Esterowitz, and R. J. Ginther, "Diode-pumped single-mode fluorozirconate fiber laser from the $^4I_{11/2} \rightarrow {}^4I_{13/2}$ transition in erbium," *Appl. Phys. Lett.*, vol. 56, no. 17, pp. 1635–1637, 1990.

[24] H. Yanagita, I. Masuda, T. Yamashita, and H. Toratani, "Diode laser pumped Er^{3+} fibre laser operation between 2.7-2.8 µm," *Electron. Lett.*, vol. 26, no. 22, pp. 1836–1838, Oct. 1990.

[25] R. M. Percival, S. F. Carter, D. Szebesta, S. T. Davey, and W. A. Stallard, "Thulium-doped monomode fluoride fibre laser broadly tunable from 2.25 to 2.5 µm," *Electron. Lett.*, vol. 27, no. 21, pp. 1912–1913, Oct. 1991.

[26] E. Poppe, B. Srinivasan, and R. K. Jain, "980 nm diode-pumped continuous wave mid-IR (2.7 µm) fibre laser," *Electron. Lett.*, vol. 34, no. 24, pp. 2331–2333, Nov. 1998.

[27] S. D. Jackson, "Single-transverse-mode 2.5-W holmium-doped fluoride fiber laser operating at 2.86 µm," *Opt. Lett.*, vol. 29, no. 4, pp. 334–336, Feb. 2004.

[28] K. J. Linden, "Fiber laser with 1.2-W CW-output power at 2712 nm," *IEEE Photon. Technol. Lett.*, vol. 16, no. 2, pp. 401–403, Feb. 2004.

[29] X. Zhu and R. Jain, "Compact 2 W wavelength-tunable Er:ZBLAN mid-infrared fiber laser," *Opt. Lett.*, vol. 32, no. 16, pp. 2381–2383, Aug. 2007.

[30] S. Tokita, M. Hirokane, M. Murakami, S. Shimizu, M. Hashida, and S. Sakabe, "Stable 10 W Er:ZBLAN fiber laser operating at 2.71-2.88 µm," *Opt. Lett.*, vol. 35, no. 23, pp. 3943–3945, Dec. 2010.

[31] D. Faucher, M. Bernier, G. Androz, N. Caron, and R. Vallee, "20 W passively cooled single-mode all-fiber laser at 2.8 µm," *Opt. Lett.*, vol. 36, no. 7, pp. 1104–1106, Apr. 2011.

[32] S. D. Jackson, M. Pollnau, and J. Li, "Diode pumped erbium cascade fiber lasers," *IEEE J. Quantum Electron.*, vol. 47, no. 4, pp. 471–478, Apr. 2011.

[33] R. Li, J. Li, L. Shterengas, and S. D. Jackson, "Highly efficient holmium fibre laser diode pumped at 1.94 µm," *Electron. Lett.*, vol. 47, no. 19, pp. 1089–1090, Sep. 2011.

[34] J. Li, L. Wang, H. Luo, J. Xie, and Y. Liu, "High power cascaded erbium doped fluoride fiber laser at room temperature," *IEEE Photon. Technol. Lett.*, vol. 28, no. 6, pp. 673–676, Mar. 2016.

[35] J. Zmojda, M. Kochanowicz, P. Miluski, G. C. Righini, M. Ferrari, and D. Dorosz, "Investigation of upconversion luminescence in $Yb^{3+}/Tm^{3+}/Ho^{3+}$ triply doped antimony-germanate glass and double-clad optical fiber," *Opt. Mater.*, vol. 58, pp. 279–284, Aug. 2016.

[36] J. Zmojda, M. Kochanowicz, P. Miluski, J. Dorosz, J. Pisarska, W. A. Pisarski, and D. Dorosz, "Investigation of upconversion luminescence in antimony-germanate double-clad two cores optical fiber co-doped with Yb^{3+}/Tm^{3+} and Yb^{3+}/Ho^{3+} ions," *J. Lumin.*, vol. 170, pp. 795–800, Feb. 2016.

[37] M. Kochanowicz, J. Zmojda, P. Miluski, T. Ragin, W. A. Pisarski, J. Pisarska, R. Jadach, M. Sitarz, and D. Dorosz, "Structural and luminescent properties of germanate glasses and double-clad optical fiber co-doped with Yb^{3+}/Ho^{3+}," *J. Alloys Compd.*, vol. 727, pp. 1221–1226, Dec. 2017.

[38] T. Ragin, J. Zmojda, M. Kochanowicz, P. Miluski, P. Jelen, M. Sitarz, and D. Dorosz, "Enhanced mid-infrared 2.7 µm luminescence in low hydroxide bismuth-germanate glass and optical fiber co-doped with Er^{3+}/Yb^{3+} ions," *J. Non-Cryst. Solids*, vol. 457, pp. 169–174, Feb. 2017.

[39] F. Enrichi, C. Armellini, S. Belmokhtar, A. Bouajaj, A. Chiappini, M. Ferrari, A. Quandt, G. C. Righini, A. Vomiero, and L. Zur, "Visible to NIR downconversion process in Tb^{3+}-Yb^{3+} codoped silica-hafnia glass and glass-ceramic sol-gel waveguides for solar cells," *J. Lumin.*, vol. 193, pp. 44–50, Jan. 2018.

[40] G. H. Dieke and H. M. Crosswhite, "The spectra of the doubly and triply ionized rare earths," *Appl. Opt.*, vol. 2, no. 7, pp. 675–686, Jul. 1963.

[41] J. Yang, Y. Tang, R. Zhang, and J. Xu, "Modeling and characteristics of gain-switched diode-pumped Er-Yb codoped fiber lasers," *IEEE J. Quantum Electron.*, vol. 48, no. 12, pp. 1560–1567, Dec. 2012.

[42] J. Yang, H. Li, Y. Tang, and J. Xu, "Temporal characteristics of in-band-pumped gain-switched thulium-doped fiber lasers," *J. Opt. Soc. Am. B*, vol. 31, no. 1, pp. 80–86, Jan. 2014.

[43] S. Yan, Y. Wang, Y. Zhou, N. Yang, Y. Li, Y. Tang, and J. Xu, "Developing high-power hybrid resonant gain-switched thulium fiber lasers," *Opt. Express*, vol. 23, no. 20, pp. 25 675–25 687, Oct. 2015.

[44] C. A. Coello Coello, G. T. Pulido, and M. S. Lechuga, "Handling multiple objectives with particle swarm optimization," *IEEE Trans. Evol. Comput.*, vol. 8, no. 3, pp. 256–279, Jun. 2004.

[45] F. Prudenzano, L. Mescia, A. D'Orazio, M. De Sario, V. Petruzzelli, A. Chiasera, and M. Ferrari, "Optimization and characterization of rare-earth-doped photonic-crystal-fiber amplifier using genetic algorithm," *J. Lightw. Technol.*, vol. 25, no. 8, pp. 2135–2142, Aug. 2007.

[46] A. Giaquinto, L. Mescia, G. Fornarelli, and F. Prudenzano, "Particle swarm optimization-based approach for accurate evaluation of upconversion parameters in Er^{3+}-doped fibers," *Opt. Lett.*, vol. 36, no. 2, pp. 142–144, Jan. 2011.

[47] L. Mescia, A. Giaquinto, G. Fornarelli, G. Acciani, M. De Sario, and F. Prudenzano, "Particle swarm optimization for the design and characterization of silica-based photonic crystal fiber amplifiers," *J. Non-Cryst. Solids*, vol. 357, no. 8, pp. 1851–1855, Apr. 2011.

[48] F. Prudenzano, L. Mescia, L. Allegretti, V. Moizan, V. Nazabal, and F. Smektala, "Theoretical study of cascade laser in erbium-doped chalcogenide glass fibers," *Opt. Mater.*, vol. 33, no. 2, pp. 241–245, 2010.

[49] S. Sujecki, L. Sojka, E. Beres-Pawlik, Z. Tang, D. Furniss, A. B. Seddon, and T. M. Benson, "Modelling of a simple Dy^{3+} doped chalcogenide glass fibre laser for mid-infrared light generation," *Opt. Quantum Electron.*, vol. 42, no. 2, pp. 69–79, 2010.

[50] G. P. Agrawal, *Nonlinear Fiber Optics*, 4th ed. San Diego, CA: Academic, 2007.

[51] N. Y. Voo, J. K. Sahu, and M. Ibsen, "345-mW 1836-nm single-frequency DFB fiber laser MOPA," *IEEE Photon. Technol. Lett.*, vol. 17, no. 12, pp. 2550–2552, Dec. 2005.

[52] L. Brilland, F. Smektala, G. Renversez, T. Chartier, J. Troles, T. N. Nguyen, N. Traynor, and A. Monteville, "Fabrication of complex structures of holey fibers in chalcogenide glass," *Opt. Express*, vol. 14, no. 3, pp. 1280–1285, Feb. 2006.

[53] G. Palma, P. Bia, L. Mescia, T. Yano, V. Nazabal, J. Taguchi, A. Moreac, and F. Prudenzano, "Design of fiber coupled Er^{3+}:chalcogenide microsphere amplifier via particle swarm optimization algorithm," *Opt. Eng.*, vol. 53, no. 7, p. 071805, Dec. 2013.

[54] L. Mescia, S. Girard, P. Bia, T. Robin, A. Laurent, F. Prudenzano, A. Boukenter, and Y. Ouerdane, "Optimization of the design of high power Er^{3+}/Yb^{3+}-codoped fiber amplifiers for space missions by means of particle swarm approach," *IEEE J. Sel. Topics Quantum Electron.*, vol. 20, no. 5, pp. 484–491, Sep. 2014.

[55] R. R. Gattass, L. B. Shaw, F. H. Kung, D. J. Gibson, V. Q. Nguyen, G. D. Chin, L. E. Busse, I. D. Aggarwal, and J. S. Sanghera, "Infrared fiber N x 1 multimode combiner," *IEEE Photon. J.*, vol. 5, no. 5, pp. 7 100 905–7 100 905, Oct. 2013.

[56] R. Thapa, R. R. Gattass, V. Nguyen, G. Chin, D. Gibson, W. Kim, L. B. Shaw, and J. S. Sanghera, "Low-loss, robust fusion splicing of silica to chalcogenide fiber for integrated mid-infrared laser technology development," *Opt. Lett.*, vol. 40, no. 21, pp. 5074–5077, Nov. 2015.

[57] N. P. Barnes and R. E. Allen, "Room temperature Dy:YLF laser operation at 4.34 µm," *IEEE J. Quantum Electron.*, vol. 27, no. 2, pp. 277–282, Feb. 1991.

[58] H. Jelinkova, M. E. Doroshenko, M. Jelinek, J. Sulc, V. V. Osiko, V. V. Badikov, and D. V. Badikov, "Dysprosium-doped $PbGa_2S_4$ laser generating at 4.3 µm directly pumped by 1.7 µm laser diode," *Opt. Lett.*, vol. 38, no. 16, pp. 3040–3043, Aug. 2013.

[59] G. Carlone, A. D'Orazio, M. De Sario, L. Mescia, V. Petruzzelli, and F. Prudenzano, "Design of double-clad erbium-doped holey fiber amplifier," *J. Non-Cryst. Solids*, vol. 351, no. 21-23, pp. 1840–1845, 2005.

[60] F. Prudenzano, L. Mescia, L. A. Allegretti, M. De Sario, T. Palmisano, F. Smektala, V. Moizan, V. Nazabal, and J. Troles, "Design of Er^{3+}-doped chalcogenide glass laser for MID-IR application," *J. Non-Cryst. Solids*, vol. 355, no. 18-21, pp. 1145–1148, 2009.

[61] L. Sojka, Z. Tang, H. Zhu, E. Beres-Pawlik, D. Furniss, A. B. Seddon, T. M. Benson, and S. Sujecki, "Study of mid-infrared laser action in chalcogenide rare earth doped glass with Dy^{3+}, Pr^{3+} and Tb^{3+}," *Opt. Mater. Express*, vol. 2, no. 11, pp. 1632–1640, Nov. 2012.

[62] G. E. Snopatin, V. S. Shiryaev, V. G. Plotnichenko, E. M. Dianov, and M. F.Churbanov, "High-purity chalcogenide glasses for fiber optics," *Inorg. Mater.*, vol. 45, no. 13, p. 1439, 2009.

[63] M. Bozzetti, A. D'Orazio, M. De Sario, V. Petruzzelli, F. Prudenzano, and F. Renna, "Tapered photonic bandgap microstrip lowpass filters: design and reali-

sation," *Microwaves, Antennas and Propagation, IEE Proceedings*, vol. 150, no. 6, pp. 459–462, Dec. 2003.

[64] G. Calò, A. D'Orazio, M. De Sario, L. Mescia, V. Petruzzelli, and F. Prudenzano, "Tunability of photonic band gap notch filters," *IEEE Trans. Nanotechnol.*, vol. 7, no. 3, pp. 273–284, May 2008.

[65] M. R. Majewski and S. D. Jackson, "Highly efficient mid-infrared dysprosium fiber laser," *Opt. Lett.*, vol. 41, no. 10, pp. 2173–2176, May 2016.

[66] M. R. Majewski and S. D. Jackson, "Tunable dysprosium laser," *Opt. Lett.*, vol. 41, no. 19, pp. 4496–4498, Oct. 2016.

[67] M. R. Majewski, R. I. Woodward, and S. D. Jackson, "Dysprosium-doped ZBLAN fiber laser tunable from 2.8 µm to 3.4 µm, pumped at 1.7 µm," *Opt. Lett.*, vol. 43, no. 5, pp. 971–974, Mar. 2018.

[68] R. I. Woodward, M. R. Majewski, G. Bharathan, D. D. Hudson, A. Fuerbach, and S. D. Jackson, "Watt-level dysprosium fiber laser at 3.15 µm with 73% slope efficiency," *Opt. Lett.*, vol. 43, no. 7, pp. 1471–1474, Apr. 2018.

[69] M. Gorjan, R. Petkovsek, M. Marincek, and M. Copic, "High-power pulsed diode-pumped Er:ZBLAN fiber laser," *Opt. Lett.*, vol. 36, no. 10, pp. 1923–1925, May 2011.

[70] C. Wei, H. Luo, H. Shi, Y. Lyu, H. Zhang, and Y. Liu, "Widely wavelength tunable gain-switched Er^{3+}-doped ZBLAN fiber laser around 2.8 µm," *Opt. Express*, vol. 25, no. 8, pp. 8816–8827, Apr. 2017.

[71] H. Luo, J. Li, Y. Hai, X. Lai, and Y. Liu, "State-switchable and wavelength-tunable gain-switched mid-infrared fiber laser in the wavelength region around 2.94 µm," *Opt. Express*, vol. 26, no. 1, pp. 63–79, Jan. 2018.